

**On Finite Difference Solutions for the Ocean Wave Spectrum in  
Regions of Non-Uniform Water Depth**

by

Pablo Marco Amenta

Thesis submitted to the Faculty of the  
Virginia Polytechnic Institute and State University  
in partial fulfillment of the requirements for the degree of  
Master of Science  
in  
Aerospace and Ocean Engineering

APPROVED:

---

Wayne L. Neu, Chairman

---

Joseph A. Schetz

---

Owen F. Hughes

March, 1989.

Blacksburg, Virginia

**On Finite Difference Solutions for the Ocean Wave Spectrum in  
Regions of Non-Uniform Water Depth**

by

Pablo Marco Amenta

Wayne L. Neu, Chairman

Aerospace and Ocean Engineering

(ABSTRACT)

This investigation is concerned with the determination of the sea state in terms of wave spectra. The phenomenon was calculated for two different bathymetries.

The purpose is to develop a finite difference method with an upwind differencing scheme to solve several formulations of the wave action conservation equation. The computations were done in the wave number space and the frequency direction space. For the case of a beach with constant slope the results were compared with the analytical solution. For the case of an elliptical submerged shoal, they were compared with experimental data.

The results of the computer code showed a fairly good qualitative agreement with the actual values for a smooth distribution of input energy.

## Acknowledgements

My deepest gratitude is for my parents, \_\_\_\_\_ y \_\_\_\_\_ for their limitless support during my education. Special thanks go to my sister, \_\_\_\_\_ and her husband . \_\_\_\_\_ Also, a special acknowledgement is for my grandfather \_\_\_\_\_ who had a strong influence during my childhood.

The author wishes to express his gratitude to his advisor, Wayne L. Neu, for the many opportunities, guidance and support he has provided me in the course of my graduate studies at Virginia Poly.

I am grateful to Joseph A. Schetz for his guidance and teaching during my Masters Degree, as well as for serving on my examining comitee and reviewing my thesis.

I also want to thank Owen F. Hughes for serving on my examining comitee and his review of this thesis.

Special thanks are for

\_\_\_\_\_ and \_\_\_\_\_ for their guidance and teaching during my studies in Buenos Aires.

Finally, I thank all my good friends and \_\_\_\_\_ for the pleasant and very funny times we shared.

# Table of Contents

NOTATION .....	1
CHAPTER I .....	3
INTRODUCTION .....	4
CHAPTER II .....	7
PROBLEM FORMULATION .....	8
II.1 MATHEMATICAL REPRESENTATION OF RANDOM SEAS .....	8
II.1.1 Small Amplitude Water Wave Theory .....	8
a) Governing Partial Differential Equation (PDE) .....	8
b) Boundary Value Problem .....	9
c) Solution of the PDE .....	11
d) Extension to 2-D .....	12
II.1.2 Stochastic Representation of the Sea .....	13
a) General Description .....	13

b) General Principles of Time Series Analysis of Waves .....	14
c) The Energy Density Spectrum .....	17
d) The Significant Wave Height .....	21
e) Spectral Formulation of Wind-Generated Seas .....	22
f) Directional Spectrum .....	23
II.1.3 A Variational Approach to the Evolution of the Wave Spectrum .....	25
a) General Derivation .....	25
b) General Considerations .....	30
II.2 THE GOVERNING EQUATION .....	31
II.2.1. Derivation of the Governing Equation .....	31
II.2.2. Exact Solution in 1-D .....	36
<b>CHAPTER III .....</b>	<b>37</b>
<b>EVOLUTION OF THE SPECTRUM ON A 1-D TOPOGRAPHY .....</b>	<b>38</b>
III.1 GENERAL CONSIDERATIONS .....	38
III.2 GENERAL COMPUTATIONS .....	39
III.3 EVOLUTION IN THE $(\sigma, \theta)$ DOMAIN .....	40
III.3.1. Unidirectional Spectrum .....	41
III.3.2. Multidirectional Spectrum .....	42
III.3.3. Grid Development .....	43
III.3.4. Stability Analysis .....	43
III.3.5. Treatment of the Boundary Conditions .....	45
III.3.6. Results .....	45
III.4 EVOLUTION IN THE $(k, \theta)$ DOMAIN .....	49
III.4.1. General Description .....	49
III.4.2. Grid Development .....	49
III.4.3. Stability Analysis .....	50

III.4.4. Treatment of the Boundary Conditions .....	51
III.4.5. Results .....	51
III.5 EVOLUTION IN THE ( $k_1$ , $k_2$ ) DOMAIN .....	53
III.5.1. General Description .....	53
III.5.2. Grid Development .....	54
III.5.3. Stability Analysis .....	54
III.5.4. Treatment of the Boundary Conditions .....	54
III.5.5. Results .....	55
<b>CHAPTER IV .....</b>	<b>57</b>
<b>EVOLUTION OF THE SPECTRUM ON A 2-D TOPOGRAPHY .....</b>	<b>58</b>
IV.1 GENERAL CONSIDERATIONS .....	58
IV.2 EXPERIMENTAL INPUT INFORMATION .....	59
Experimental Conditions .....	59
IV.3 NUMERICAL COMPUTATIONS .....	60
Finite Difference Method Scheme .....	60
IV.4 RESULTS .....	62
<b>CHAPTER V .....</b>	<b>68</b>
<b>CONCLUSIONS .....</b>	<b>69</b>
<b>REFERENCES .....</b>	<b>71</b>
<b>FIGURES .....</b>	<b>74</b>
<b>Vita .....</b>	<b>151</b>

## List of Illustrations

Figure 1.	Spatial reference system	75
Figure 2.	Sketch indicating the structure of a random sea (Pierson et al.)	76
Figure 3.	Principles of predicting random seas (Ochi M.)	77
Figure 4.	Frequency spectrum according to the TMA formulation for $\gamma = 2$ and $\gamma = 20$	78
Figure 5.	Wrapped normal spreading function for $\lambda = 10$ and $\lambda = 30$ , and cosine squared formulation vs $\theta$	79
Figure 6.	Comparison of the analytical solution to the numerical prediction of the action A for the unidirectional case with and without expansion of the x-derivative vs $kh$	80
Figure 7.	Comparison of the analytical solution to the numerical prediction of the integration of $A(\theta)$ for different grid resolution in $\theta$ vs $kh$	81
Figure 8.	Contour levels of the numerical error of the numerical prediction of the action A at each angular band at each location for the formulation with no expanded derivatives in $\theta$ and $x$	82
Figure 9.	Contour levels of the numerical error of the numerical prediction of the action A at each angular band at each location for the formulation with expanded derivatives in $\theta$	83
Figure 10.	Contour levels of the numerical error of the numerical prediction of the action A at each angular band at each location for the formulation with expanded derivatives in $\theta$ and $x$	84
Figure 11.	Comparison of the analytical solution to the prediction of the action A using different grid resolution in $\theta$ , with no expanded derivatives in $\theta$ and $x$ vs $kh$	85
Figure 12.	Comparison of the analytical solution to the numerical prediction of the action A using different grid resolution in $x$ , with no expanded derivatives in $\theta$ and $x$ vs $kh$	86
Figure 13.	Comparison of the analytical solution to the numerical prediction of the action A using different grid resolution in $\theta$ , with expanded derivatives in $\theta$ vs $kh$	87
Figure 14.	Comparison of the analytical solution to the numerical prediction of the action A using different grid resolution in $x$ , with expanded derivatives in $\theta$ vs $kh$	88

Figure 15.	Comparison of the analytical solution to the numerical prediction of the action A using 1st and 3rd order differencing in $\theta$ , with expanded derivatives in $\theta$ vs $kh$ . . .	89
Figure 16.	Comparison of the analytic solution to the prediction of the action A using 1st and 3rd order differencing in $\theta$ with the directional spectrum centered midway between bands . . . . .	90
Figure 17.	Comparison of the analytic solution to the prediction of the action A using different grid resolution in $x$ , for the formulation with expanded derivatives in $\theta$ and $x$ vs $kh$	91
Figure 18.	Comparison of the analytical solution to the numerical prediction of the action A using 1st and 3rd order differencing in $\theta$ vs $kh$ . . . . .	92
Figure 19.	Comparison of the analytical solution to the numerical prediction of the action A using 1st and 3rd order differencing in $\theta$ doubling the resolution in $\theta$ vs $kh$ . . . .	93
Figure 20.	Comparison of the analytic solution to the prediction of the action A using 1st and 3rd order differencing in $\theta$ with the directional spectrum centered midway between bands . . . . .	94
Figure 21.	Analytical solution for the action N in the $(k, \theta)$ space at $x/L_0 = 0.035$ . . . . .	95
Figure 22.	Analytical solution for the action N in the $(k, \theta)$ space at $x/L_0 = 0.520$ . . . . .	96
Figure 23.	Analytical solution for the action N in the $(k, \theta)$ space at $x/L_0 = 0.760$ . . . . .	97
Figure 24.	Analytical solution for the action N in the $(k, \theta)$ space at $x/L_0 = 1.000$ . . . . .	98
Figure 25.	Numerical Prediction for the action N in the $(k, \theta)$ space at $x/L_0 = 0.035$ . . . . .	99
Figure 26.	Numerical Prediction for the action N in the $(k, \theta)$ space at $x/L_0 = 0.520$ . . . .	100
Figure 27.	Numerical Prediction for the action N in the $(k, \theta)$ space at $x/L_0 = 0.760$ . . . .	101
Figure 28.	Numerical Prediction for the action N in the $(k, \theta)$ space at $x/L_0 = 1.000$ . . . .	102
Figure 29.	Numerical Prediction for the action N in the $(k, \theta)$ space using 2nd order differencing in $k$ at $x/L_0 = 0.035$ . . . . .	103
Figure 30.	Numerical Prediction for the action N in the $(k, \theta)$ space using 2nd order differencing in $k$ at $x/L_0 = 0.520$ . . . . .	104
Figure 31.	Numerical Prediction for the action N in the $(k, \theta)$ space using 2nd order differencing in $k$ at $x/L_0 = 0.760$ . . . . .	105
Figure 32.	Numerical Prediction for the action N in the $(k, \theta)$ space using 2nd order differencing in $k$ at $x/L_0 = 1.000$ . . . . .	106
Figure 33.	Numerical Prediction for the action N in the $(k, \theta)$ space using 3rd order differencing in $k$ at $x/L_0 = 0.760$ . . . . .	107
Figure 34.	Analytical solution for the action N in the $(k, \theta)$ space with sinusoidal initial conditions at $x/L_0 = 0.035$ . . . . .	108
Figure 35.	Analytical solution for the action N in the $(k, \theta)$ space with sinusoidal initial conditions at $x/L_0 = 0.520$ . . . . .	109

Figure 36.	Analytical solution for the action $N$ in the $(k, \theta)$ space with sinusoidal initial conditions at $x/L_0 = 0.760$ .....	110
Figure 37.	Analytical solution for the action $N$ in the $(k, \theta)$ space with sinusoidal initial conditions at $x/L_0 = 1.000$ .....	111
Figure 38.	Numerical prediction for the action $N$ in the $(k, \theta)$ space with sinusoidal initial conditions at $x/L_0 = 0.035$ .....	112
Figure 39.	Numerical prediction for the action $N$ in the $(k, \theta)$ space with sinusoidal initial conditions at $x/L_0 = 0.520$ .....	113
Figure 40.	Numerical prediction for the action $N$ in the $(k, \theta)$ space with sinusoidal initial conditions at $x/L_0 = 0.760$ .....	114
Figure 41.	Numerical prediction for the action $N$ in the $(k, \theta)$ space with sinusoidal initial conditions at $x/L_0 = 1.000$ .....	115
Figure 42.	Analytic solution for the action $N$ in the $(k_1, k_2)$ space at $x/L_0 = 0.035$ .....	116
Figure 43.	Analytic solution for the action $N$ in the $(k_1, k_2)$ space at $x/L_0 = 0.520$ .....	117
Figure 44.	Analytic solution for the action $N$ in the $(k_1, k_2)$ space at $x/L_0 = 0.760$ .....	118
Figure 45.	Analytic solution for the action $N$ in the $(k_1, k_2)$ space at $x/L_0 = 1.000$ .....	119
Figure 46.	Numerical prediction for the action $N$ in the $(k_1, k_2)$ space at $x/L_0 = 0.035$ ...	120
Figure 47.	Numerical prediction for the action $N$ in the $(k_1, k_2)$ space at $x/L_0 = 0.520$ ...	121
Figure 48.	Numerical prediction for the action $N$ in the $(k_1, k_2)$ space at $x/L_0 = 0.760$ ...	122
Figure 49.	Numerical prediction for the action $N$ in the $(k_1, k_2)$ space at $x/L_0 = 1.000$ ...	123
Figure 50.	General array of the wave tank .....	124
Figure 51.	Description of the boundary conditions and the computational domain .....	125
Figure 52.	Wave height levels as given by paper for the monochrome case with $\sigma = 4.83$ Hz and $\lambda = 0$ .....	126
Figure 53.	Wave height levels as given by paper for the spectral case with $\gamma = 2$ and $\lambda = 10$	127
Figure 54.	Wave height levels as given by paper for the spectral case with $\gamma = 2$ and $\lambda = 30$	128
Figure 55.	Wave height levels as given by SAS/Graph plotting the basin data for the monochrome case with $\sigma = 4.83$ Hz and $\lambda = 0$ .....	129
Figure 56.	Wave height levels as given by SAS/Graph plotting the basin data for the spectral case with $\gamma = 2$ and $\lambda = 10$ .....	130
Figure 57.	Wave height levels as given by SAS/Graph plotting the basin data for the spectral case with $\gamma = 2$ and $\lambda = 30$ .....	131
Figure 58.	Numerical prediction for the wave height for the monochrome case with $\sigma = 4.83$ Hz and $\lambda = 0$ .....	132

Figure 59.	Numerical prediction for the wave height for the spectral case with $\gamma = 2$ and $\lambda = 10$ .....	133
Figure 60.	Numerical prediction for the wave height for the spectral case with $\gamma = 2$ and $\lambda = 30$ .....	134
Figure 61.	Numerical prediction for the wave height for the monochrome case with $\sigma = 3.30$ Hz and $\lambda = 0$ .....	135
Figure 62.	Numerical prediction for the wave height for the monochrome case with $\sigma = 8.00$ Hz and $\lambda = 0$ .....	136
Figure 63.	Numerical prediction for the wave height for the monochrome case with $\sigma = 4.83$ Hz and $\lambda = 0$ and a depth at the center of the shoal of 0.05 m (33% less deep)	137
Figure 64.	Comparison of the experimental data to the numerical prediction of the wave height H for the monochrome case with $\sigma = 4.83$ Hz and $\lambda = 0$ at $x/R_o = 2$ vs $y/R_o$ .....	138
Figure 65.	Comparison of experimental data to the numerical prediction of the wave height H using higher resolution in $\theta$ with $\sigma = 4.83$ Hz and $\lambda = 0$ at $x/R_o = 2$ .....	139
Figure 66.	Comparison of the experimental data to the numerical prediction of the wave height H for the monochrome case with $\sigma = 4.83$ Hz and $\lambda = 0$ at $x/R_o = 0$ vs $y/R_o$ .....	140
Figure 67.	Comparison of the experimental data to the numerical prediction of the wave height H for the monochrome case with $\sigma = 4.83$ Hz and $\lambda = 0$ at $x/R_o = 1$ vs $y/R_o$ .....	141
Figure 68.	Comparison of the experimental data to the numerical prediction of the wave height H for the monochrome case with $\sigma = 4.83$ Hz and $\lambda = 0$ at the center line vs $x/R_o$ .....	142
Figure 69.	Comparison of the experimental data to the numerical prediction of the wave height H for the spectral case with $\gamma = 2$ and $\lambda = 10$ at $x/R_o = 0$ vs $y/R_o$ ....	143
Figure 70.	Comparison of the experimental data to the numerical prediction of the wave height H for the spectral case with $\gamma = 2$ and $\lambda = 10$ at $x/R_o = 1$ vs $y/R_o$ ....	144
Figure 71.	Comparison of the experimental data to the numerical prediction of the wave height H for the spectral case with $\gamma = 2$ and $\lambda = 10$ at $x/R_o = 2$ vs $y/R_o$ ....	145
Figure 72.	Comparison of the experimental data to the numerical prediction of the wave height H for the spectral case with $\gamma = 2$ and $\lambda = 10$ at the center line vs $x/R_o$	146
Figure 73.	Comparison of the experimental data to the numerical prediction of the wave height H for the spectral case with $\gamma = 2$ and $\lambda = 30$ at $x/R_o = 0$ vs $y/R_o$ ....	147
Figure 74.	Comparison of the experimental data to the numerical prediction of the wave height H for the spectral case with $\gamma = 2$ and $\lambda = 30$ at $x/R_o = 1$ vs $y/R_o$ ....	148
Figure 75.	Comparison of the experimental data to the numerical prediction of the wave height H for the spectral case with $\gamma = 2$ and $\lambda = 30$ at $x/R_o = 2$ vs $y/R_o$ ....	149

Figure 76. Comparison of the experimental data to the numerical prediction of the wave height  $H$  for the spectral case with  $\gamma = 2$  and  $\lambda = 30$  at the center line vs  $x/R_0$  150

# NOTATION

$a$	wave amplitude
$A$	wave action
$c$	phase velocity
$c_g$	group velocity
$D$	spreading function
$E$	energy function
$f$	circular frequency
$f_m$	modal circular frequency
$g$	gravity acceleration
$h$	water depth
$H$	wave height
$k$	wave number
$L$	wave length
$L_o$	length of $x$ -domain
$N$	wave action
$p$	pressure
$R$	variance of wave height

$R_0$	minimum radius of the shoal
$s$	phase function
$S$	wave spectrum
$t$	time
$T$	wave period
$x,y,z$	spatial coordinates
$u,v,w$	particle velocities
$z$	variance

*Greek symbols*

$\beta$	wave number
$\nabla$	del operator
$\Delta$	delta operator
$\varepsilon$	phase constant
$\eta$	surface elevation
$\gamma$	shape parameter
$\lambda$	directional spreading parameter
$\phi$	velocity potential
$\Phi$	transformation factor for shallow water
$\rho$	density
$\sigma$	frequency
$\sigma_m$	modal frequency
$\theta$	angular direction

# CHAPTER I

# INTRODUCTION

Marine structures are designed to withstand the dashing of wind-generated waves. According to the type of the design, different elements and parameters of the sea state are needed. For instance, for the deck elevation, an appropriate measure of the wave height should be known. In other cases the requisites are more directly related to the wave energy density, where the distribution along the frequency domain is of significant importance, as well as the distribution in the angular direction, since sometimes it is necessary to evaluate the response of ships and marine structures in a seaway for which six degrees of motion have to be considered. Finally in coastal waters it is of importance to estimate the wave energy along the shoreline, as this energy is related to many shore and harbor phenomena such as sediment transport and beach erosion. These reasons lead to the comprehension of the importance of an operational wave forecasting model.

The purpose of this work is to develop and test the performance of a numerical prediction scheme to solve the problem of the evolution of wave spectra as the waves propagate from deep water over complex bathymetry into shallow water.

In the literature, a number of different theories deal with this problem. It is important to know which method can be best used with respect to accuracy, computer costs

and practical flexibility. The complexity of natural waves systems is a recognized fact. Nevertheless, most engineering analysis of wave propagation over irregular bathymetry have been based on representation of seastate by a monochromatic wave of height, period and direction chosen to approximate the significant wave.

One method is the mild slope equation derived by Berkhoff [1], in terms of the velocity potential function. It is an elliptic refraction-diffraction equation. It is useful in harbors (reflecting boundaries) and tsunami propagation. But in large open sea areas it becomes computationally unfeasible [2]. One restriction in this formulation is that the bottom slopes have to be mild.

A second method is the parabolic approximation equation [1], that has been developed simplifying the mild slope equation, since diffraction only along the wave front is taken into account. Its disadvantage is that it requires that one grid coordinate essentially follow the dominant wave direction. It is more feasible to solve than the mild slope equation.

A third method is the refraction approximation of the mild slope equation [1]. It neglects diffraction effects in both directions  $x$  and  $y$ . It leads to the so called eikonal equation, and can be solved by the method of characteristics (classic wave ray method). No reflection is taken into account. As each ray is computed independently from the others, the computational effort is reduced. But due to refraction, the refraction diagrams can show intersection points of wave rays (caustics), and the computation of wave amplitude is not possible with this equation at these points, which are very common in practical applications. Besides, the solution is found along wave rays, so it is not possible to determine this solution at pre-designated locations.

Although useful, the description of the sea surface in terms of monochromatic waves is at best an approximation. One reason for this is that the shallow water region may act as a filter against certain frequencies of the deep water spectrum, whereas it has fo-

cusing effects on other frequencies resulting in a shift of the mean frequency of the spectrum in shallow water. It is then possible that given the right conditions, two shallow water points separated only by a few kilometers, will exhibit completely different shallow water wave spectra. Most realistic sea states have a more complex, randomly irregular structure. This structure is characterized by a spectral distribution over a wave number space or a polar frequency direction space.

The equation of wave action conservation is another expression of the wave energy conservation. It is simpler if current interactions are taken into account. The boundary conditions are relatively easily handled, specially for the incoming and outgoing energy at any propagation direction in the region of analysis.

The study of the features and performance of a Fortran code of a Finite Difference Method scheme for the governing equation is the problem of interest in this research. The first part describes a mathematical representation of the ocean waves problem. The main aspects and variables are presented together with some elements of the ray theory and the variational approach. The second part is a description of how the problem was solved for a 1-D case. A beach with a constant sloped bottom was chosen, and the numerical results were compared to the analytical solution in terms of wave action. Different formulations of the governing equation were tried for different conditions, in order to investigate the different behaviours of the code. The third part deals with the 2-D case. A submerged elliptical shoal was chosen, and the results were compared to experimental data, in terms of wave amplitude.

It can be deduced through the last two parts that the main obstacle to get accurate results lies on the fact of the finite differencing of the  $\theta$ -space. Further improvements may be obtained with refined  $\theta$  resolution and/or more sophisticated finite difference schemes.

## CHAPTER II

# PROBLEM FORMULATION

## II.1 MATHEMATICAL REPRESENTATION OF RANDOM SEAS

### *II.1.1 Small Amplitude Water Wave Theory*

#### *a) Governing Partial Differential Equation (PDE)*

To develop the governing PDE of the linear water wave problem, it is assumed that the flow is irrotational and incompressible. Also, for this deduction, no currents are taken into account and no surface tension is considered [3].

The continuity equation for incompressible fluids states

$$\nabla \cdot \mathbf{u} = 0 \tag{2.1}$$

where  $\mathbf{u} = u \hat{i} + v \hat{j} + w \hat{k}$  is the water particle velocity, and  $\nabla = \frac{\partial}{\partial x} + \frac{\partial}{\partial y} + \frac{\partial}{\partial z}$  is the del operator,  $(x,y,z)$  being a coordinate system fixed in space (Figure 1).

Assuming the motion is irrotational gives the possibility to introduce a velocity potential function

$$\mathbf{u} = -\nabla\phi \quad (2.2)$$

where  $\phi$  is the velocity potential.

They together lead to the Laplace equation

$$\nabla^2\phi = 0 \quad (2.3)$$

### *b) Boundary Value Problem*

For a 1-D water wave the geometric boundary conditions are

#### *1. The kinematic free surface boundary condition*

The surface is free to deform under the influence of forces, and there is no mass flow through it. If the surface is expressed by

$$F(x,y,z,t) = z - \eta(x,y,t) = 0 \quad (2.4)$$

where  $\eta$  is the surface displacement and  $t$  is time, then

$$\frac{D}{Dt} F(x,y,z,t) = \frac{\partial F}{\partial t} + u \frac{\partial F}{\partial x} + v \frac{\partial F}{\partial y} + w \frac{\partial F}{\partial z} = 0 \quad \text{on } F = 0 \quad (2.5)$$

This boundary condition, will be used in its linearized form, since small wave amplitudes are considered. Because of this, the velocities  $u$  and  $v$ , and the derivatives  $\frac{\partial \eta}{\partial x}$  and  $\frac{\partial \eta}{\partial y}$  are also considered small, consequently the second order terms can be neglected, and then the equation can be evaluated at  $z = 0$

$$w = - \left. \frac{\partial \phi}{\partial z} \right]_{z=0} = \frac{\partial \eta}{\partial t} \quad (2.6)$$

### 2. The dynamic free surface boundary condition

As a "free" surface, the air-water interface cannot support variation in pressure across the interface (no surface tension is considered), and must respond so as to maintain continuity of pressure. Then at the surface, the pressure in the water must equal atmospheric pressure. The unsteady Bernoulli equation is used to form a condition on the velocity potential:

$$- \frac{\partial \phi}{\partial t} + \frac{1}{2} (u^2 + w^2) + \frac{p}{\rho} + gz = C(t) \quad (2.7)$$

where  $p$  is the pressure taken to be constant,  $\rho$  is the density, and  $g$  is the gravity acceleration. The function  $\phi$  can be chosen such that  $C(t) = 0$ .

This boundary condition is linearized for small amplitude waves, with the same considerations of the previous one. This yields to

$$\eta = \frac{1}{g} \left[ \left. \frac{\partial \phi}{\partial t} \right]_{z=0} \right] \quad (2.8)$$

### 3. The kinematic horizontal bottom boundary condition

No mass flow can happen through a solid bottom. Consequently for an horizontal impermeable bottom the boundary condition is

$$w = - \left. \frac{\partial \phi}{\partial z} \right]_{z=-h} = 0 \quad (2.9)$$

where  $h$  is the water depth.

The solution of the PDE is also required to be periodic in  $x$  and in  $t$ . This can be expressed as

$$\phi(x,t) = \phi(x + L,t) \quad (2.10)$$

where  $L$  is the wave length.

$$\phi(x,t) = \phi(x,t + T) \quad (2.11)$$

where  $T$  is the wave period.

### *c) Solution of the PDE*

A time harmonic function  $\phi(x,z,t)$  with frequency  $\sigma$  will be obtained. This frequency can be calculated as

$$\sigma = \frac{2\pi}{T} \quad (2.12)$$

A separation of variables solution and the application of the boundary conditions lead to the final solution for the velocity potential function for a progressive wave

$$\phi(x,z,t) = - \frac{a g \cosh k(h+z)}{\sigma \cosh kh} \sin(kx - \sigma t) \quad (2.13)$$

where  $a$  is the wave amplitude, that is half the wave height  $H$ , and  $k = \frac{2\pi}{L}$  is the wavenumber.

To satisfy the kinematic free surface boundary condition the dispersion relationship is obtained

$$\sigma^2 = gk \tanh kh \quad (2.14)$$

Then by (2.8) the profile of a progressive wave moving in the  $x$  -direction is given by

$$\eta(x,t) = a \cos(kx - \sigma t) \quad (2.15)$$

*d) Extension to 2-D*

To write (2.15) in a more general way, using the coordinate system  $(x,y,z)$  fixed in the space, Figure (1), the equation (2.15) becomes

$$\eta(x,y,t) = a \cos\{k(x \cos \theta + y \sin \theta) - \sigma t + \varepsilon\} \quad (2.16)$$

where  $\varepsilon$  is a phase constant and  $\theta$  is the direction of travel of the wave.

The wind generated waves at a certain location may be considered as a linear superposition of simple harmonic waves of different length, amplitude and coming from different directions, Figure (2).

$$\eta(x,y,t) = \sum_{i=1}^N a_i \cos\{k_i(x \cos \theta_i + y \sin \theta_i) - \sigma_i t + \varepsilon_i\} \quad (2.17)$$

## *II.1.2 Stochastic Representation of the Sea*

### *a) General Description*

If one observes a restless sea, it will be clear that it is rarely feasible to describe it simply in terms of a plane wave. At one instant one can see an irregular surface composed of crests and troughs of non-uniform sizes. Some time later a quite different pattern can be seen.

To be able to describe the sea state, probabilistic and statistical methods have to be used. One method of predicting the statistical properties of a random process is making random (not sucesive) observations (in this case of the wave amplitude) in the time domain. Then assuming that this variable obeys a certain probability density function (in this case the Raleigh distribution), one can predict the expected value to occur with a specified confidence coefficient (confidence interval) if the sample size is small (less than about 150 observations); or with the maximum likelihood estimation method if the sample size is large.

A second method is the usage of the frequency domain. It is a much more rigorous way of computing the necessary variables and wave characteristics (Figure 3). In the time domain height point measurements along time are taken from the random sea to build the auto-correlation function. Then in the frequency domain the wave spectrum as a function of frequency is obtained, following the Wiener-Khintchine theorem and the Fourier Transformation. Fast Fourier Transformation can be also used, but in this case the auto-covariance funcion is not obtained.

Finally in the probability domain, after some simplifying assumptions , the probability density function of wave height is obtained. Knowing this function any statistic (moment) can be completely determined. For example the significant wave height.

The above procedure will be briefly described below.

*b) General Principles of Time Series Analysis of Waves*

As it was stated before, the sea surface displacement  $\eta$  may be thought of as a superposition of different waves. According to equation (2.17)

$$\eta(x,y,t) = \sum_{i=1}^N a_i \cos\{\mathbf{k}_i \cdot \mathbf{x} + \sigma_i t - \varepsilon_i\} \quad (2.18)$$

where the amplitude  $a_i$  is a random variable for each  $\mathbf{k}_i$  and  $\sigma_i$ .

One statistical measure of this surface  $\eta$  is the joint probability density function [5]

$$p(\eta_1, \eta_2) \quad (2.19)$$

defined in such a way that the probability that  $\eta_1$  and  $\eta_2$  at the points  $(x_1, t_1)$  and  $(x_2, t_2)$  lies within the limits  $a, b$  and  $c, d$  respectively is

$$P = \int_a^b \int_c^d p(\eta_1, \eta_2) d\eta_1 d\eta_2 \quad (2.20)$$

It follows that

$$P = \int_{-\infty}^{\infty} \int_{-\infty}^{\infty} p(\eta_1, \eta_2) d\eta_1 d\eta_2 = 1 \quad (2.21)$$

In a similar way  $p(\eta_1)$  is defined in such a way that the probability that  $\eta_1$  lies within the limits  $a$  and  $b$  is

$$P = \int_a^b p(\eta_1) d\eta_1 \quad (2.22)$$

and satisfies

$$P = \int_{-\infty}^{\infty} p(\eta_1) d\eta_1 = 1 \quad (2.23)$$

The expected value, or the probability average of the value is

$$\bar{\eta} = \int_{-\infty}^{\infty} \eta p(\eta) d\eta \quad (2.24)$$

The cross-correlation is [19]

$$\begin{aligned} \overline{\eta(\mathbf{x}, t) \eta(\mathbf{x} + \mathbf{r}, t + \tau)} &= \int_{-\infty}^{\infty} \int_{-\infty}^{\infty} \eta_1 \eta_2 p(\eta_1, \eta_2) d\eta_1 d\eta_2 \\ &= z(\mathbf{x}, \mathbf{r}, t, \tau) \end{aligned} \quad (2.25)$$

where  $\eta_1 \equiv \eta(\mathbf{x}, t)$  and  $\eta_2 \equiv \eta(\mathbf{x} + \mathbf{r}, t + \tau)$ .

At this time two assumptions are made

- the wave field is homogeneous, i.e. the probability density functions do not depend on the position  $\mathbf{x}$ .
- the wave field is stationary, i.e. the probability density functions do not depend on the time  $t$ .

These assumptions can be made if not dealing with large scale and long term variations in the wave field.

Consequently it can be written that

$$z = z(\mathbf{r}, \tau).$$

For the particular case  $\mathbf{r} = 0$ , and  $\tau = 0$ , this function is the mean square surface displacement

$$\bar{\eta}^2 = z(0,0) = \int_{-\infty}^{\infty} \eta_1^2 p(\eta_1) d\eta_1 \quad (2.26)$$

If the above equation is multiplied by  $(\frac{1}{2} \rho g)$  it becomes the expression for the mean energy per unit surface area in the wave field.

The problem is that one does not know  $p(\eta)$ , nor can it be measured. All that is known about it a priori is that the mean of  $\eta$  is zero. That is  $E[\eta] = \bar{\eta} = 0$ .

In addition, a way to find expected values from the realization  $\eta_1(t)$  of the random process  $\eta$  is taking time averages. This is the ergodic assumption [4]: "If  $\eta$  is an ergodic stationary random function, then the first moment and the covariance function obtained by ensemble (ensemble is a set of simultaneous observations at different points) are identical to the corresponding time averages computed for any given realization,  $\eta_1$ ." That is

$$E[\eta] = \lim_{T \rightarrow \infty} \frac{1}{2T} \int_{-T}^T \eta_1(t) dt \quad (2.27)$$

$$z(\mathbf{r}, \tau) = \lim_{T \rightarrow \infty} \frac{1}{2T} \int_{-T}^T [\eta_1(t) - \bar{\eta}(t)] [\eta_2(t + \tau) - \bar{\eta}(t)] dt \quad (2.28)$$

If  $\mathbf{r} = 0$  the cross-covariance becomes the auto-covariance.

$$z(0, \tau) = \lim_{T \rightarrow \infty} \frac{1}{2T} \int_{-T}^T [\eta_1(t) - \bar{\eta}(t)] [\eta_1(t + \tau) - \bar{\eta}(t)] dt \quad (2.29)$$

Since  $\bar{\eta}(t) = 0$ , this is also the auto-correlation function.

In addition, if the time shift  $\tau = 0$ ,

$$z(0,0) = \bar{\eta}^2 = \lim_{T \rightarrow \infty} \frac{1}{2T} \int_{-T}^T \eta_1^2(t) dt \quad (2.30)$$

Thus, the variance of  $\eta$ ,  $E[\eta^2(t)] = z(0,0)$ , can be calculated.

In this way, with the ergodicity assumption the analysis of a single record  $\eta_1(t)$  provides all the necessary statistical information.

### c) *The Energy Density Spectrum*

Once more, the surface elevation at one point is given by (2.18)

$$\eta(x,y,t) = \sum_{i=1}^N a_i \cos\{\mathbf{k}_i \cdot \mathbf{x} + \sigma_i t - \varepsilon_i\}$$

If this point is chosen as the origin the equation becomes

$$\eta(t) = \sum_{i=1}^N a_i \cos(\sigma_i t - \varepsilon_i) \quad (2.31)$$

with

$$-\infty < \sigma_i < \infty, \quad 0 < a_i < \infty \quad \text{and} \quad -\pi < \varepsilon_i < \pi$$

With a trigonometric identity this equation can be rewritten as

$$\eta(t) = \sum_{i=1}^N [b_i \cos \sigma_i t + c_i \sin \sigma_i t] \quad (2.32)$$

with

$$b_i = a_i \cos \varepsilon_i$$

$$c_i = a_i \sin \varepsilon_i$$

so

$$a_i^2 = b_i^2 + c_i^2$$

If in equation (2.32) the  $\sigma_i$  were all integer multiples of  $\sigma_1$ , it should represent the development of the function  $\eta(t)$  in a Fourier Series and the Fourier coefficients would yield the amplitudes of each frequency. However, in the case of the wave field there is not a discrete set of frequencies, but a continuous distribution of frequencies. In the limit, the sum becomes an integral, so

$$\eta(t) = \int_{-\infty}^{\infty} a(\sigma) \cos[\sigma t - \varepsilon(\sigma)] d\sigma = \int_{-\infty}^{\infty} b(\sigma) \cos \sigma t d\sigma + \int_{-\infty}^{\infty} c(\sigma) \sin \sigma t d\sigma \quad (2.33)$$

with

$$b(\sigma) = \frac{1}{2\pi} \int_{-\infty}^{\infty} \eta(t) \cos \sigma t dt \quad (2.34)$$

$$c(\sigma) = \frac{1}{2\pi} \int_{-\infty}^{\infty} \eta(t) \sin \sigma t dt \quad (2.35)$$

From these two equations  $a(\sigma)$  can be calculated as

$$a^2(\sigma) = b^2(\sigma) + c^2(\sigma) \quad (2.36)$$

The amplitude spectrum  $a(\sigma)$  resulting from the realization  $\eta_1(t)$  will accurately represent the realization for times within the measurement interval, but cannot say anything about times outside of the sample interval. If a large number of realizations of the same process could be made, each would yield a different  $a(\sigma)$ . Then the variance of  $a(\sigma)$  can be calculated as a function of  $\sigma$ , and this can be used to obtain expectations of the process.

Nevertheless, making all these realizations is not practical.

The variance calculation is obtained by (2.30).

For the distribution of variance by  $\sigma$ ,  $z(0, \tau)$  is developed in Fourier Transform with equations (2.34) and (2.35) replacing  $\eta$  with  $z(0, \tau)$ . Since  $z(0, \tau)$  is even

$$c(\sigma) = 0 \quad (2.37)$$

$$b(\sigma) = \frac{1}{2\pi} \int_{-\infty}^{\infty} z(0, \tau) \cos \sigma \tau d\tau \quad (2.38)$$

From equation (2.33)

$$z(0, \tau) = \int_{-\infty}^{\infty} b(\sigma) \cos \sigma \tau d\sigma \quad (2.39)$$

$b(\sigma)$  is the variance density frequency spectrum or simply the frequency spectrum of the wave field, so

$$S(\sigma) = b(\sigma)$$

This is also known as the Wiener-Khinchine Theorem that states [4] [5]: "For any ergodic stationary real random function  $\eta$  with zero mean, the spectrum  $S(\sigma)$  is given by the Fourier transformation of the auto-covariance function of  $\eta$ ":

$$S(\sigma) = \frac{1}{2\pi} \int_{-\infty}^{\infty} z(0, \tau) e^{i\sigma\tau} d\tau \quad (2.40)$$

Since  $S(\sigma)$  is an even function, it is usually defined as

$$S(\sigma) = S(\sigma) \quad \sigma \geq 0 \quad (2.41)$$

for  $\tau = 0$  equation (2.39) implies

$$z(0,0) = E[\eta^2] = \int_0^{\infty} S(\sigma) d\sigma \quad (2.42)$$

or the area under  $S(\sigma)$  is one half of the variance of  $\eta$ .

Since the average wave energy is proportional to the variance,  $S(\sigma)$  may be interpreted as an energy density spectrum, missing only a factor  $\rho g$ .

#### *d) The Significant Wave Height*

Finally, to determine the probability function of wave height (in the probability domain), 3 assumptions are made

- i) the surface elevation  $\eta$  is a stationary normal process with
- ii) narrow band spectrum (i.e. energy sufficiently concentrated near one frequency)
- iii) statistically independent wave heights

With this, it can be derived theoretically that the wave heights are governed by the Rayleigh probability density function [6]

$$f(H) = 2 \frac{H}{R} e^{-H^2/R} \quad 0 \leq H < \infty \quad (2.43)$$

where  $R$  is the variance of wave height  $H$ , i.e.  $R = 8 \int_0^\infty S(\sigma) d\sigma$

The statistics are

$$E[H] = \frac{\sqrt{\pi}}{2} R \quad (2.44)$$

$$E[H^2] = \left(1 - \frac{\pi}{4}\right) R \quad (2.45)$$

The significant wave height,  $H_{1/3}$  is defined as the average of the highest one-third of wave heights. Commonly it is used to represent the severity of the sea.

Writing the lower limit of the highest one-third of a sample as  $H^*$  the following probability equation can be written

$$P[H > H^*] = \int_{H^*}^{\infty} f(H) dH = \frac{1}{3} \quad (2.46)$$

Taking the moment about the origin

$$H_{1/3} \frac{1}{3} = \int_{H^*}^{\infty} H f(H) dH \quad (2.47)$$

From these two equations,  $H^*$  and  $H_{1/3}$  can be obtained in terms of the parameter  $R$  of the Rayleigh distribution. Since the parameter  $R$  is the variance of the wave height and is equal to 8 times the area under the wave spectral density function,  $H_{1/3}$  becomes [6]

$$H_{1/3} = 4.01 \sqrt{m_0} \quad (2.48)$$

$$\text{where } m_0 = \int_0^{\infty} S(\sigma) d\sigma$$

### e) Spectral Formulation of Wind-Generated Seas

The shape of wave spectra varies according to the geographical location, duration and fetch of the wind, stage of growth and decay of a storm, and existence of swell.

The JONSWAP spectrum is used in Chapter III as the incident one, and its expression is

$$S(f) = \alpha g^2 (2\pi)^{-4} f^{-5} e^{-\frac{5}{4}(f/f_m)^{-4}} \gamma e^{-\frac{1}{2}(f-f_m)^2/(2\sigma^2 f_m^2)} \quad (2.49)$$

where

$\alpha = 0.01$  is the scale parameter

$f = \frac{1}{T}$  is the circular frequency

$f_m$  is the modal frequency, i.e. the frequency at which  $S$  is a maximum

$\sigma = \sigma_a = 0.07$   $f_m \geq f$

$\sigma = \sigma_b = 0.09$   $f_m < f$

$\gamma = 3.3$  is the shape parameter

The TMA shallow-water spectrum presented by Bouws et. al [7] is used in Chapter IV as the incident spectrum. It is the JONSWAP spectrum multiplied by the transformation factor for shallow water [8]  $\Phi$ , which is a function of the frequency  $f$  and the depth  $h$ , i.e.  $\Phi = \Phi(f, h)$ . The complete expression results in

$$S(f) = \alpha g^2 (2\pi)^{-4} f^{-5} e^{-\frac{5}{4}(f/f_m)^{-4}} \gamma e^{-(f-f_m)^2/(2\sigma^2)} \Phi \quad (2.50)$$

Different curves  $S(f)$  are obtained, according to the value of  $\gamma$ , for the conditions of the shoal trials. This is shown in Figure (4).

### *f) Directional Spectrum*

The wave spectrum  $S$  as developed above is a point spectrum, i.e. it is the spectrum of surface fluctuations at a point, regardless of which direction the wave is propagating. In reality, wind-generated waves do not necessarily propagate toward one specific direction. The wave energy associated with the frequencies close to the modal frequency is primarily propagated in the wind direction, while energy associated with lower and higher frequencies is distributed over a range of angular directions [6].

The directional wave spectrum  $S(f, \theta)$  can be represented by

$$S(f, \theta) = S(f) D(f, \theta) \quad (2.51)$$

where  $\theta$  is the direction of wave propagation and  $D(f, \theta)$  is an angular spreading function.

The following two relations are satisfied

$$S(f) = \int_0^{2\pi} S(f, \theta) d\theta \quad (2.52)$$

and

$$\int_0^{2\pi} D(f, \theta) d\theta = 1 \quad (2.53)$$

The spreading function  $D(f, \theta)$  used to describe the incident directional spectrum in Chapter IV is [9]

$$D(f, \theta) = \frac{1}{2\pi} + \frac{1}{\pi} \sum_{l=1}^L \cos l(\theta - \theta_m) e^{-\frac{1}{2}(l\lambda)^2} \quad (2.54)$$

with

$L = 15$  is an arbitrary number of harmonics

$\theta_m$  is the mean wave direction at the frequency  $f$

$\lambda$  is the directional spreading parameter at the frequency  $f$

Different curves are obtained according to the value of  $\lambda$ . This is shown in Figure (5).

The spreading function used in Chapter III is [6]

$$D(\theta) = \frac{2}{\pi} \cos^2 \theta \quad -\frac{\pi}{2} \leq \theta \leq \frac{\pi}{2} \quad (2.55)$$

This curve is also shown in Figure (5).

### II.1.3 A Variational Approach to the Evolution of the Wave Spectrum

#### a) General Derivation

A propagating wave is a travelling disturbance about an equilibrium state; it may be thought of as a moving front and analyzed using the ray theory. Some fundamental aspects of the ray theory will be shown below. A deeper treatment of the subject may be found in [4].

The simple wave may be written as

$$\eta(\mathbf{x}, t) = a(\mathbf{x}, t) \Re_e \{ e^{iS(\mathbf{x}, t)} \} \quad (2.56)$$

$$\text{where } S(\mathbf{x}, t) = \mathbf{k} \cdot \mathbf{x} - \sigma t \quad (2.57)$$

is the phase function, and may represent the wave front or crest.

It can be seen that

$$\mathbf{k} = \nabla S \quad (2.58)$$

and

$$\sigma = - \frac{\partial S}{\partial t} \quad (2.59)$$

The conservation of crest equation is thus derived from (2.58) and (2.59)

$$\frac{\partial \mathbf{k}}{\partial t} + \nabla \sigma = 0 \quad (2.60)$$

The conservation of crest equation may be interpreted as if  $\mathbf{k}$  were a directional density of crests in space and  $\sigma$  a flux of crests past a fixed point.

The phase velocity, i.e. the velocity of a crest  $c$ , may be obtained if one considers the function  $S = \text{const.}$ , thus if

$$S(\mathbf{x}, t) = \text{const} \quad (2.61)$$

it is obvious that

$$dS(\mathbf{x}, t) = 0, \quad (2.62)$$

which in its expanded form becomes

$$\frac{\partial S}{\partial t} dt + \nabla S \cdot d\mathbf{x} = 0 \quad (2.63)$$

Consequently the points that belong to the surface defined by the function  $S$  move with a velocity  $c$ , given by

$$\mathbf{c} = \frac{d\mathbf{x}}{dt} = \sigma \frac{\mathbf{k}}{k^2} \quad (2.64)$$

The group velocity, the velocity at which the wave energy propagates, can be shown to be [3]

$$c_{g_i} = \frac{\partial \sigma}{\partial k_i} \quad (2.65)$$

therefore its magnitude is given by

$$|c_g| = c_g = \frac{\sigma}{k} \frac{1}{2} \left[ 1 + \frac{2kh}{\sinh 2kh} \right] \quad (2.66)$$

With all these elements a variational approach for the evolution of the spectrum can be developed [4][10] [15]. The first step is to introduce a generic energy function, then this energy function has to be minimum, according to the Hamilton Variational Principle. In order to get this minimum, the first variation of this function is set equal to zero, from where the Euler-Lagrange equations are obtained. These Euler-Lagrange equations lead to two equations: the dispersion relation and the energy conservation equation. These main aspects of this development are briefly described below. A complete and rigorous mathematical explanation is available in the mentioned references.

In what follows, subscripts are used to denote differentiation with respect to the explicit dependence of  $L$  on the dependant variables  $(a, \sigma, \mathbf{k})$  and the independant variables  $(\mathbf{x}, t)$ , whereas the conventional derivatives include complete differentiation with respect to one independant variable, keeping the others fixed.

The functional  $J$  (total energy) for this case may be expressed as

$$J = \int \int L \, d\mathbf{x} \, dt \quad (2.67)$$

where  $L = L(\mathbf{q}, \mathbf{q}_x, \mathbf{q}_t, \mathbf{x}, t)$  is an energy density function averaged over a period of time, that is

$$L = \frac{1}{T} \int_0^T U \, dt \quad (2.68)$$

and

$\mathbf{q}$  is a general vector which components are generic functions

$U$  is the energy density function

The necessary condition for a relative extreme of  $J$  is that its first variation,  $\delta J$ , vanish, i.e.

$$\delta J = 0 \quad (2.69)$$

From this equation, (2.69), the Euler-Lagrange equation can be obtained

$$\frac{\partial L}{\partial \mathbf{q}} - \frac{\partial}{\partial t} \left( \frac{\partial L}{\partial \dot{\mathbf{q}}_t} \right) - \frac{\partial}{\partial \mathbf{x}} \left( \frac{\partial L}{\partial \dot{\mathbf{q}}_x} \right) = 0 \quad (2.70)$$

Choosing as the dependant variables  $a$  and  $S$  (the components of the vector  $\mathbf{q}$ ) and choosing as the independant variables  $\mathbf{x}$  and  $t$  it can be written that

$$L = L(a, S_t, \nabla S, \mathbf{x}, t) \quad (2.71)$$

with (2.58) and (2.59) this becomes

$$L = L(a, \sigma, \mathbf{k}, \mathbf{x}, t) \quad (2.72)$$

Now the dependant variables are  $a$ ,  $\sigma$ , and  $\mathbf{k}$ .

Expanding the Euler-Lagrange equation in the scalar form, two equations can be obtained

$$1) L_a = 0 \quad (2.73)$$

$$2) \frac{\partial}{\partial t} L_\sigma - \frac{\partial}{\partial \mathbf{x}} L_{\mathbf{k}} = 0 \quad (2.74)$$

The equation (2.73) leads to a certain function  $G$  that relates  $a$ ,  $\sigma$ , and  $\mathbf{k}$

$$G(a, \sigma, \mathbf{k}) = 0 \quad (2.75)$$

that for small amplitude waves becomes the dispersion relation, equation (2.14), that is independent of the amplitude  $a$ , so

$$G(\sigma, \mathbf{k}) = 0 \quad (2.76)$$

As the energy density  $L$  is proportional to  $a^2$ ,  $L(a, \sigma, \mathbf{k})$  can be expressed as

$$L = G(\sigma, \mathbf{k})a^2 \quad (2.77)$$

This last equation with (2.76) for linear waves lead to conclude that

$$L = 0 \quad (2.78)$$

At this step the derivative of  $L$  with respect to time is necessary, its expression is

$$\frac{\partial L}{\partial t} = L_\sigma \frac{\partial \sigma}{\partial t} + L_{k_i} \frac{\partial k_i}{\partial t} + L_a \frac{\partial a}{\partial t} + L_t \quad (2.79)$$

besides from (2.76) and (2.77) it may be written that

$$c_{g_i} = \frac{\partial \sigma}{\partial k_i} = - \frac{L_{k_i}}{L_\sigma} \quad (2.80)$$

This equation (2.79) together with the equation (2.74) are equivalent to

$$\frac{\partial}{\partial t} [\sigma L_\sigma - L] - \frac{\partial}{\partial x_i} [\sigma L_{k_i}] = - L_t \quad (2.81)$$

If the product  $\sigma L_\sigma$  is considered as an energy function called  $E$ , that is

$$\sigma L_\sigma = E \quad (2.82)$$

the simple energy conservation equation is obtained from (2.78), (2.80) and (2.81) for a medium at rest, and if  $L$  does not depend explicitly on  $t$ , i.e.  $L_t = 0$ . Therefore

$$\frac{\partial}{\partial t} E + \frac{\partial}{\partial x_i} (c_{g_i} E) = 0 \quad (2.83)$$

If the *Wave Action* is defined as

$$A \equiv \frac{E}{\sigma} \quad (2.84)$$

equation (2.74) becomes

$$\frac{\partial}{\partial t} A + \frac{\partial}{\partial x_i} (c_{g_i} A) = 0 \quad (2.85)$$

or, in other words, the wave action conservation equation.

### ***b) General Considerations***

The conservation of wave action is more fundamental than that of energy, since it applies to moving systems as well as to stationary ones.

It is only in a time invariant system, where

$$\frac{d\sigma}{dt} = 0 \quad (2.86)$$

that (2.85) reduces to (2.83).

For example, if the fluid is moving with a slowly varying velocity (i.e. currents)  $U(\mathbf{x}, t)$  with respect to an inertial coordinate system, equation (2.85) becomes

$$\frac{\partial}{\partial t} A_o + \frac{\partial}{\partial x_i} (c_{g_{io}} A_o) = 0 \quad (2.87)$$

but equation (2.83) becomes

$$\frac{\partial}{\partial t} E_o + \frac{\partial}{\partial x_i} (c_{g_{io}} E_o) - \frac{E_o}{\sigma_o} \frac{d\sigma_o}{dt} = 0 \quad (2.88)$$

having to compute an extra term. The subscript "o" indicates quantities observed within the moving system.

The approach is linear. Only effects of shoaling and refraction are taken into account. The transfer of energy from one frequency band to the other by non-linear wave-wave interaction, energy dissipations due to bottom friction, whitecapping and turbulence, and atmospheric energy input are neglected. Thus, its application in shallow water or near the surfline is doubtful.

It is quite simple to treat the incident and outgoing waves at the boundary conditions.

## II.2 THE GOVERNING EQUATION

### *II.2.1. Derivation of the Governing Equation*

While (2.85) can be directly extended to action density spectra, e.g. [11], it is better for our present purposes to proceed along slightly different lines now that the principle of conservation of action has been established.

Different forms of (2.85) may be obtained, according to the domain where one is working, and the degree of expansion of the derivatives. Although they are analytically identical, numerically they have different behaviour and complexity. The aim of this work is to study them.

The action density spectrum  $A(\sigma, \theta)$  gives a description of the sea surface fluctuation at a point. If the bottom is uneven, each component of the action spectrum is refracted as it propagates, with the result that the action becomes a function of the surface coordinates  $(x, y)$ , in addition to  $\sigma$  and  $\theta$ . If a transitory state is to be computed a fifth variable,  $t$ , has to be considered.

In the general case, therefore

$$A = A(x, y, \sigma, \theta, t)$$

As a wave propagates through space, its frequency,  $\sigma$ , and its direction of travel,  $\theta$ , may change. For the spectrum, this represents propagation of action in the  $\sigma$  and  $\theta$  directions as well as in the  $x$  and  $y$  directions.

By analogy to the fluid mass conservation, equation (2.85) may be interpreted as: the net rate of action inflow per unit volume at a point is the negative divergence of the action. Under the concept of a four dimensional space, this results in [12]

$$\frac{\partial A}{\partial t} + \nabla \cdot (\mathbf{v}A) = 0 \quad (2.89)$$

in which  $\mathbf{v}$  is a four-dimensional velocity vector whose components are equal to the propagation velocity of the wave action in each direction and the vector operator  $\nabla$  has the components

$$\nabla = \left[ \frac{\partial}{\partial x}, \frac{\partial}{\partial y}, \frac{\partial}{\partial \sigma}, \frac{\partial}{\partial \theta} \right]. \quad (2.90)$$

Equation (2.89) is a general equation that describes the propagation of the wave action in the four-dimensional  $(x, y, \sigma, \theta)$ -space.

The components of the velocity vector  $\mathbf{v}$ , are found by using the results from monochromatic wave refraction methods based on small amplitude wave theory. The velocity vector is given by

$$\begin{bmatrix} v_x \\ v_y \\ v_\sigma \\ v_\theta \end{bmatrix} = \begin{bmatrix} c_g \cos \theta \\ c_g \sin \theta \\ d\sigma/dt \\ d\theta/dt \end{bmatrix} \quad (2.91)$$

in which  $\frac{d\theta}{dt} = \frac{1}{k} \frac{\partial \sigma}{\partial h} \left( \frac{\partial h}{\partial x} \sin \theta - \frac{\partial h}{\partial y} \cos \theta \right)$ , and  $\frac{\partial \sigma}{\partial h} = \frac{gk^2}{2\sigma \cosh^2 kh}$ .

In the absence of currents or time varying mean water depth, neither of which are considered here,  $\frac{d\sigma}{dt} = 0$ .

Consequently a first formulation that can be obtained is (in what follows, the notation [F*i*] stands for "formulation number *i*")

[F1]

$$\frac{\partial A}{\partial t} + \frac{\partial}{\partial x} (c_g \cos \theta A) + \frac{\partial}{\partial y} (c_g \sin \theta A) + \frac{\partial}{\partial \theta} \left( \frac{\partial \theta}{\partial t} A \right) = 0 \quad (2.92)$$

[F2] is obtained by expanding the  $\theta$ -derivative in (2.92), as

$$\frac{\partial}{\partial \theta} \frac{\partial \theta}{\partial t} = \frac{1}{k} \frac{\partial \sigma}{\partial h} \left[ \frac{\partial h}{\partial x} \cos \theta + \frac{\partial h}{\partial y} \sin \theta \right] \quad (2.93)$$

the expansion results in

$$\begin{aligned} \frac{\partial A}{\partial t} + \frac{\partial}{\partial x} (c_g \cos \theta A) + \frac{\partial}{\partial y} (c_g \sin \theta A) + \frac{\partial \theta}{\partial t} \frac{\partial A}{\partial \theta} + \\ + \left( \frac{\partial \sigma}{\partial x} \cos \theta + \frac{\partial \sigma}{\partial y} \sin \theta \right) \frac{1}{k} A = 0 \end{aligned} \quad (2.94)$$

[F3] is obtained expanding the  $\theta$  and  $x$ -derivatives in (2.92) :

$$\begin{aligned} \frac{\partial A}{\partial t} + c_g \cos \theta \frac{\partial A}{\partial x} + \frac{\partial c_g}{\partial x} \cos \theta A + c_g \sin \theta \frac{\partial A}{\partial y} + \frac{\partial c_g}{\partial y} \sin \theta A + \frac{\partial \theta}{\partial t} \frac{\partial A}{\partial \theta} + \\ + \left( \frac{\partial \sigma}{\partial x} \cos \theta + \frac{\partial \sigma}{\partial y} \sin \theta \right) \frac{1}{k} A = 0 \end{aligned} \quad (2.95)$$

Alternate equations can be derived from this. Noting that the wave phase velocity is given by (2.64)

$$c = \frac{\sigma}{k} = \left[ \frac{g}{k} \tanh kh \right]^{1/2}, \quad (2.96)$$

and multiplying (2.92) by  $cc_g$ , after some algebra this results in [F4]

$$\frac{D}{Dt} (cc_g A) = \frac{\partial}{\partial t} (cc_g A) + \mathbf{v} \cdot \nabla (cc_g A) = 0 \quad (2.97)$$

which with further manipulations becomes

$$\frac{\partial A}{\partial t} + \left[ \frac{\cos \theta}{c} \frac{\partial}{\partial x} + \frac{\sin \theta}{c} \frac{\partial}{\partial y} \right] (cc_g A) + \frac{\partial \theta}{\partial t} \frac{\partial A}{\partial \theta} = 0 \quad (2.98)$$

The same action conservation equation can be expressed in terms of the wave number  $k$ , either in a rectangular  $(k_x, k_y)$  or polar  $(k, \theta)$  representation, instead of the polar  $(\sigma, \theta)$ -space, since  $\sigma$  and  $k$  are related by the dispersion relation (2.14).

It can be derived theoretically that the relation between  $A$  and  $N$  is given by

$$N(x, k, \theta) = \frac{c_g(x, k)}{k} \left[ A(x, \sigma, \theta) \right]_{\sigma=\sigma(x, k)} \quad (2.99)$$

Denoting  $N$  as the action density spectrum in the wave number space,  $N = N(x, y, k_1, k_2, t)$ , the resulting equation can be derived in the same way as the  $A$  equation, this is

$$\frac{\partial N}{\partial t} + \frac{\partial}{\partial x_i} (\dot{x}_i N) + \frac{\partial}{\partial k_i} (\dot{k}_i N) = 0 \quad (2.100)$$

with  $\dot{x}_i = \frac{dx_i}{dt}$  and  $\dot{k}_i = \frac{dk_i}{dt}$ , then knowing that

$$\frac{\partial \dot{x}_i}{\partial x_i} = - \frac{\partial \dot{k}_i}{\partial k_i} \quad (2.101)$$

the final equation is obtained as

$$\frac{DN}{Dt} = \frac{\partial N}{\partial t} + \dot{x}_i \frac{\partial N}{\partial x_i} + \dot{k}_i \frac{\partial N}{\partial k_i} = 0 \quad (2.102)$$

Writing this in a complete manner

$$\frac{\partial N}{\partial t} + c_g \cos \theta \frac{\partial N}{\partial x} + c_g \sin \theta \frac{\partial N}{\partial y} - \frac{\partial \sigma}{\partial h} \frac{\partial h}{\partial x} \frac{\partial N}{\partial k_1} - \frac{\partial \sigma}{\partial h} \frac{\partial h}{\partial y} \frac{\partial N}{\partial k_2} = 0 \quad (2.103)$$

Now turning into the polar  $(k, \theta)$ -space in a similar way the general equation is

$$\frac{\partial N}{\partial t} + \frac{\partial}{\partial x} (\dot{x} N) + \frac{\partial}{\partial \theta} (\dot{\theta} N) + \frac{\partial}{\partial k} (\dot{k} N) = 0 \quad (2.104)$$

that if it is written in a complete manner results in

$$\begin{aligned} \frac{\partial N}{\partial t} + c_g \cos \theta \frac{\partial N}{\partial x} + c_g \sin \theta \frac{\partial N}{\partial y} - \frac{\partial \sigma}{\partial h} \frac{\partial h}{\partial x} \left( \frac{\partial N}{\partial k} \cos \theta - \frac{1}{k} \frac{\partial N}{\partial \theta} \sin \theta \right) - \\ - \frac{\partial \sigma}{\partial h} \frac{\partial h}{\partial y} \left( \frac{\partial N}{\partial k} \sin \theta + \frac{1}{k} \frac{\partial N}{\partial \theta} \cos \theta \right) = 0 \end{aligned} \quad (2.105)$$

### II.2.2. Exact Solution in 1-D

A unidirectional spectrum travelling in the  $x$ -direction, with a plane bathymetry composed of parallel contours in the  $y$ -direction is determined simply by applying the shoaling coefficient squared [3] [13].

$$A(\sigma) = k_s^2(h, \sigma) A_o(\sigma) = \frac{c_{go}}{c_g} A_o(\sigma) \quad (2.106)$$

where the subscript "o" means reference condition.

A multidirectional spectrum travelling in the same bottom conditions is determined by [13]

$$A(\sigma, \theta) = \frac{k}{k_o} \frac{c_{go}}{c_g} A_o(\sigma, \theta_o) \quad (2.107)$$

where  $\theta_o = \sin^{-1}\left(\frac{k}{k_o} \sin \theta\right)$

## CHAPTER III

# EVOLUTION OF THE SPECTRUM ON A 1-D TOPOGRAPHY

## III.1 GENERAL CONSIDERATIONS

In this chapter both unidirectional and multidirectional spectra travelling over a plane bathymetry will be considered. This bathymetry has parallel contours in the  $y$ -direction, with a constant slope  $dh/dx$  that leads to shallower water. With this particular case, there is no " $y$ " dependence, and the action conservation equation becomes simpler, as some terms vanish. The action conservation equation will be solved numerically, and the results compared to the analytic exact solution shown in Chapter II, Section II.2.2.

Three different domains will be studied. In the  $(\sigma, \theta)$  space 6 formulations, according to the degree of expansion of the derivatives, are tried: 2 for the unidirectional case, and 4 for the multidirectional case. Then the action conservation equation is solved in the  $(k, \theta)$ -space, and finally in the  $(k_1, k_2)$ -space. Also, different grid resolution and different order of differencing schemes are tried to see the different behaviours.

### III.2 GENERAL COMPUTATIONS

The derivatives involving the action  $A$  and the group velocity  $c_g$  will be computed with an upwind finite difference scheme. The rest of them will be computed by analytical expressions.

For first order accurate cases, the upwind finite difference operator is

$$\left[ \frac{\partial Q}{\partial \beta} \right]_i = \frac{\Delta Q}{\Delta \beta} \Big|_i = (Q_i - Q_{i-1}) \frac{1}{\beta_i - \beta_{i-1}} \quad \text{if } \dot{\beta} > 0 \quad (3.1)$$

or

$$\left[ \frac{\partial Q}{\partial \beta} \right]_i = \frac{\Delta Q}{\Delta \beta} \Big|_i = (Q_i - Q_{i+1}) \frac{1}{\beta_i - \beta_{i+1}} \quad \text{if } \dot{\beta} \leq 0 \quad (3.2)$$

where  $\dot{\beta} = \partial \beta / \partial t$ .

In these expressions  $Q$  represents the dependant variable and  $\beta$  the independent variable. The dependent variables may be  $A$ ,  $N$  or  $c_g$ , and the independent variables may be  $x$ ,  $\theta$ ,  $k$ ,  $k_1$  or  $k_2$ .

In order to know which equation to use, (3.1) or (3.2), the direction the dependent variable is moving has to be checked. For example, if  $\dot{x} > 0$ , then the action is going in the positive direction of the  $x$ -axis, and equation (3.1) is used. If  $\dot{x} < 0$ , that means that the action is moving toward the negative  $x$ -direction, so equation (3.2) is used. Another case is in the  $\theta$ -space. If  $\dot{\theta} > 0$  the action is travelling counterclockwise, so equation (3.1) should be used. If  $\dot{\theta} < 0$ , the action moves clockwise, and then equation (3.2) is used.

For a second order accurate scheme the operator is

$$\left[ \frac{\partial Q}{\partial \beta} \right]_i = \frac{\Delta Q}{\Delta \beta} \Big|_i = \frac{1}{\Delta \beta} \left[ \frac{3}{2} Q_i - 2Q_{i-1} + \frac{1}{2} Q_{i-2} \right] \quad \text{if } \dot{\beta} > 0 \quad (3.3)$$

or

$$\left. \frac{\partial Q}{\partial \beta} \right]_i = \left. \frac{\Delta Q}{\Delta \beta} \right]_i = \frac{1}{\Delta \beta} \left[ -\frac{3}{2} Q_i + 2Q_{i+1} - \frac{1}{2} Q_{i+2} \right] \quad \text{if } \dot{\beta} \leq 0 \quad (3.4)$$

For a third order accurate scheme the operator is

$$\left. \frac{\partial Q}{\partial \beta} \right]_i = \left. \frac{\Delta Q}{\Delta \beta} \right]_i = \frac{1}{\Delta \beta} \left[ \frac{11}{6} Q_i - 3Q_{i-1} + \frac{3}{2} Q_{i-2} - \frac{1}{3} Q_{i-3} \right] \quad \text{if } \dot{\beta} > 0 \quad (3.5)$$

or

$$\left. \frac{\partial Q}{\partial \beta} \right]_i = \left. \frac{\Delta Q}{\Delta \beta} \right]_i = \frac{1}{\Delta \beta} \left[ -\frac{11}{6} Q_i + 3Q_{i+1} - \frac{3}{2} Q_{i+2} + \frac{1}{3} Q_{i+3} \right] \quad \text{if } \dot{\beta} \leq 0 \quad (3.6)$$

These second and third order schemes will be employed in the  $\theta$ -space.

Time derivatives are taken forward in time to yield an explicit time marching finite difference scheme. All comparisons of the solutions were made using the steady state. The steady state was considered achieved when the values of the action  $A$  (or  $N$ ) of two consecutive time steps gave a difference lower than a prefixed tolerance.

### III.3 EVOLUTION IN THE $(\sigma, \theta)$ DOMAIN

In this section,  $A$  is considered a function of  $x, \sigma$  and  $\theta$ . Only one frequency  $\sigma$  is taken into account, since each frequency can be treated independently from the others. The frequency acts as a parameter in the governing equation.

### III.3.1. Unidirectional Spectrum

The notation [FiU] stands for "formulation  $i$  of a unidirectional wave".

a) [F1U]

The equation (2.92) [F1] from Chapter II can be simplified since for this particular case

- there is no "y" dependence, so  $\frac{\partial}{\partial y} = 0$
- the wave travels normal to the slope, so  $v_\theta = \theta = 0$  and no refraction occurs. consequently it can be rewritten as

$$\frac{\partial A}{\partial t} + \frac{\partial}{\partial x} (c_g A) = 0 \quad (3.7)$$

b) [F3U]

For the same reasons the equation (2.95) from Chapter II becomes [F3U]

$$\frac{\partial A}{\partial t} + c_g \frac{\partial A}{\partial x} + \frac{\partial c_g}{\partial x} A = 0 \quad (3.8)$$

Although they are analitically identical, the expansion of the derivative in (3.7) leads to a different finite difference representation of the governing equation. In general, for two functions  $f$  and  $g$  one has

$$\frac{\partial}{\partial x} (fg) \cong \frac{(f + \Delta f)(g + \Delta g) - fg}{\Delta x} = \frac{1}{\Delta x} [g\Delta f + f\Delta g + \Delta f\Delta g] \quad (3.9)$$

but

$$\frac{\partial f}{\partial x} g + f \frac{\partial g}{\partial x} \cong \frac{(f + \Delta f) - f}{\Delta x} g + f \frac{(g + \Delta g) - g}{\Delta x} = \frac{1}{\Delta x} [g\Delta f + f\Delta g] \quad (3.10)$$

### III.3.2. Multidirectional Spectrum

The notation [F*i*] stands for "formulation *i*". In this section we have at each surface point waves propagating in different directions.

All the equations shown below come from the ones developed in Chapter II (i.e. [F1], [F2], [F3], [F4] ), where the *y*-dependence terms have been deleted. In this section we do have refraction, as some energy is propagating in directions not perpendicular to the bathymetry.

a) [F1]

After making the above mentioned simplifications the governing equation (2.92) [F1] becomes

$$\frac{\partial A}{\partial t} + \frac{\partial}{\partial x} (c_g \cos \theta A) + \frac{\partial}{\partial \theta} \left( \frac{\partial \theta}{\partial t} A \right) = 0 \quad (3.11)$$

b) [F2]

By simplifying (2.94) [F2], the second formulation is obtained

$$\frac{\partial A}{\partial t} + \frac{\partial}{\partial x} (c_g \cos \theta A) + \frac{\partial \theta}{\partial t} \frac{\partial A}{\partial \theta} + \frac{1}{k} \frac{\partial \sigma}{\partial x} \cos \theta A = 0 \quad (3.12)$$

c) [F3]

The completely expanded derivatives version comes from (2.95) [F3]

$$\frac{\partial A}{\partial t} + c_g \cos \theta \frac{\partial A}{\partial x} + \frac{\partial c_g}{\partial x} \cos \theta A + \frac{\partial \theta}{\partial t} \frac{\partial A}{\partial \theta} + \frac{1}{k} \frac{\partial \sigma}{\partial x} \cos \theta A = 0 \quad (3.13)$$

d) [F4]

Simplifying equation (2.98) [F4] in Chapter II

$$\frac{\partial A}{\partial t} + \frac{\cos \theta}{c} \frac{\partial}{\partial x} (cc_g A) + \frac{\partial \theta}{\partial t} \frac{\partial A}{\partial \theta} = 0 \quad (3.14)$$

### III.3.3. Grid Development

In order to choose  $\Delta\theta$ , a quantity of 12 directions was chosen. Thus  $\Delta\theta = 30^\circ$ , which was considered a reasonable first approach.

Variation in depth that goes from  $kh = 3.53$  to  $kh = 0.27$  was chosen, so as to have deep, intermediate and shallow water. To achieve this the other variables were set for typical conditions of sea waves:  $\sigma = 0.6$  Hz, which sets the initial and final depths at 96 m and 2 m respectively.

After choosing a slope, the first approximation of the  $x$ -distance is obtained, and then the initial approach of the number of  $x$ -grid points is taken as 31.

### III.3.4. Stability Analysis

If the equation (3.11) [F1] (multidirectional spectrum) is differenced, the result is

$$A_{x,\theta}^{n+1} = \left[ 1 - c_g \cos \theta \frac{\Delta t}{\Delta x} - \frac{\partial \sigma}{\partial x} \sin \theta \frac{1}{k} \frac{\Delta t}{\Delta \theta} - \frac{\partial \sigma}{\partial x} \cos \theta \frac{1}{k} \Delta t \right] A_{x,\theta}^n + \left[ c_g \cos \theta \frac{\Delta t}{\Delta x} \right] A_{x-1,\theta}^n + \left[ \frac{\partial \sigma}{\partial x} \sin \theta \frac{1}{k} \frac{\Delta t}{\Delta \theta} \right] A_{x,\theta-1}^n \quad (3.15)$$

where the coefficients of the  $A_{i,j}$  terms are computed at the  $i,j$  points.

The stability affair was analyzed mathematically following the von Neumann procedure [18][14]. In this procedure, a first step is to express the action  $A$  as

$$A_{x,\theta}^n = \zeta_n e^{i(\beta_1 x \Delta x + \beta_2 \theta \Delta \theta)} \quad (3.16)$$

where the superscript  $n$  stands for the time step.

Then this is replaced in (3.15) in order to get the amplification function  $f$  as

$$\frac{\zeta_{n+1}}{\zeta_n} = f \quad (3.17)$$

After some algebra the expression becomes

$$\begin{aligned} |f|^2 = & \left[ 1 - \frac{\partial \sigma}{\partial x} \cos \theta \frac{1}{k} \Delta t - c_g \cos \theta \frac{\Delta t}{\Delta x} (1 - \cos \beta_1 \Delta x) - \right. \\ & \left. - \frac{\partial \sigma}{\partial x} \sin \theta \frac{1}{k} \frac{\Delta t}{\Delta \theta} (1 - \cos \beta_2 \Delta \theta) \right]^2 + \left[ c_g \cos \theta \frac{\Delta t}{\Delta x} \sin \beta_1 \Delta x + \right. \\ & \left. + \frac{\partial \sigma}{\partial x} \sin \theta \frac{1}{k} \frac{\Delta t}{\Delta \theta} \sin \beta_2 \Delta \theta \right]^2 \end{aligned} \quad (3.18)$$

Since it is required that the amplification factor  $f$  be less than 1 for the iterations to be stable, it can be written that

$$|f| < 1 \quad (3.19)$$

From this, the time step  $\Delta t$  can be fixed with [16]

$$\frac{1}{\Delta t} > \frac{\partial \sigma}{\partial x} \cos \theta \frac{1}{2k} + c_g \cos \theta \frac{1}{\Delta x} + \frac{\partial \sigma}{\partial x} \sin \theta \frac{1}{k} \frac{1}{\Delta \theta} \quad (3.20)$$

In this way, i.e. fixing  $\Delta x$ , and  $\Delta k$ , can get  $\Delta t$ .

For the unidirectional spectrum, where there is no  $\theta$ -dependance the amplification function  $f$  is

$$f = 1 - 2 c_g \frac{\Delta t}{\Delta x} \quad (3.21)$$

setting the restriction  $|f| < 1$ ,  $\Delta t$  can be determined with

$$\Delta t < \frac{\Delta x}{c_g}. \quad (3.22)$$

In this way, fixing  $\Delta x$ ,  $\Delta t$  can be obtained.

### *III.3.5. Treatment of the Boundary Conditions*

For the unidirectional case,  $[A]_{x=0} = 1$  as the input energy, since any constant can fit this boundary condition. For the multidirectional case, the input energy was distributed according to the cosine square spread form, equation (2.55), and scaled such that the component in the mean direction (i.e.  $\theta = 0^\circ$ ) was set equal to 1.

### *III.3.6. Results*

The different formulations were run in a computer code, trying different alternatives, one at a time, to look for the sources of error, and how to improve the output. These alternatives are: expansion of derivatives, higher resolution in the grids, and higher order accurate schemes for computing the numerical derivatives. The results of these runs were plotted in the set of Figures discussed below. The comparisons are versus the exact analytical solution (2.106) for the unidirectional case, and (2.107) for the multidirectional case.

Figure (6) compares the results obtained from F1U and F3U with the exact solution, to see the effect of expanding the  $x$ -derivative. It is observed that F1U gives exact solution, but F3U, expanding the  $x$ -derivative, gives error which increases with decreasing depth, overestimating the exact solution.

For the multidirectional case one can compare individual direction bands or the total action at each point, i.e. the integration over directions. If one uses the integration mode, two alternatives can be followed: the exact solution that can be integrated analytically, or the numerical solution that must be integrated numerically. As it is desired to have an estimation of how important the error due to the numerical integration in the  $\theta$ -space is, the exact solution for each direction (i.e.  $A(\theta)$ ) available in Section II.2.2, is integrated numerically over  $2\pi$  and then compared to the analytically integrated exact solution that corresponds to that point. This is done for  $\Delta\theta = 30^\circ, 15^\circ$ , and  $10^\circ$ . In Figure (7) it can be observed that the numerical integration of the exact solution, i.e.  $A = \sum_{i=1}^N A(\theta_i) \Delta\theta_i$  causes an error that increases with decreasing depth, underestimating the exact solution. In the comparisons that follow, the numeric results are compared to the analytically integrated solution.

Figures (8), (9) and (10) show the numerical error at each angular band, for each position point. This error is computed as  $e = (A(\theta) - AE(\theta)) \times \Delta\theta / AE(kh)$ . Figure (8) belongs to the formulation [F1], Figure (9) to [F2] and Figure (10) to the formulation [F3]. For this group of plots the conditions were set for  $kh = 2$  to  $kh = 0.35$  because in this manner the plots are clearer. The negative values of the contour levels of this error show that there are low values of  $A$  around the  $0^\circ$  band. The positive values of the

contour levels of this error show that close to the  $60^\circ$  band there is some energy that should not be there. In other words, instead of having the main amount of energy concentrated near the  $0^\circ$  band, the energy is dispersed along other bands. Since the region of negative error has larger values, it can be concluded that this is one of the reasons of why this formulation underestimates the actual values. The results obtained from [F2], Figure (9), and [F3], Figure (10), show that although the steady state was achieved, some action is still dispersed near the  $0^\circ$  direction.

Figures (11) (higher  $\theta$ -resolution) and (12) (higher  $x$ -resolution), show the the effect of higher resolution in the different spaces for [F1], where the derivatives are not expanded. The grids were refined by a factor of 2 and 3. It is seen that

- higher resolution in  $\Delta\theta$  does not improve the results significantly.
- higher resolution in  $\Delta x$  does not improve the results significantly.

It can be concluded that with this formulation it is difficult to improve the results by a finer mesh, showing insensitiveness in this aspect.

Figures (13) and (14) correspond to the formulation [F2], where the  $\theta$ -derivative is expanded. They show the effects of increasing the resolution in  $\theta$  and  $x$  respectively. It can be seen that

- higher resolution in  $\theta$  does improve the results significantly. Increasing the angular resolution makes the numerical dispersion of action in the  $\theta$ -space become less important, obtaining more accurate results; but in this way the computational time required is sufficiently large to render the method unfeasible for an operational wave forecasting model.

- higher resolution in  $x$  improved the results little compared to increasing the resolution in  $\theta$ .

In an attempt to obtain similar improvement without extra direction bands, a higher order differencing scheme is tried. Also tried is the alternative of not centering the directional spectrum on a band, it is centered at the midpoint between direction grid points. The results are shown in Figures (15) and (16) from which it can be concluded that for [F2]

- a 3<sup>rd</sup> order formulation for  $\frac{\partial A}{\partial \theta}$  improves the results, showing again that the governing equation is very sensitive in the  $\theta$ -space.
- setting the mean direction at  $15^\circ$  improves the results, smoothing out the action distribution.

Applying either higher resolution in  $\theta$  or a 3<sup>rd</sup> order form for  $\partial A/\partial \theta$  for [F2] leads to better results than the attempts made for [F1].

Turning now to [F3], where both the  $\theta$  and  $x$  derivatives are expanded, in Figure (17) it can be seen the behaviour as well as the effects of increasing the resolution in  $x$  as before, from what it can be concluded that higher resolution in  $x$  does not make an important improvement in the results.

No higher resolution in  $\theta$  is considered, since its derivative has the same expression as in [F2].

Finally, in order to find out how sensitive is [F4] in the  $\theta$ -space, Figures (18), (19) and (20) were drawn to see that

- a 3<sup>rd</sup> order formulation for  $\frac{\partial A}{\partial \theta}$  improves the results, also showing the importance of the angular resolution here.

- doubling the resolution in  $\theta$  improves the results

- setting the mean direction at 15° improves the results.

The degree of improvement is approximately similar to the one achieved with [F2]. No higher resolution in  $x$  is tried, since it is considered that the main problem lies in the  $\theta$ -space.

### III.4 EVOLUTION IN THE ( $k, \theta$ ) DOMAIN

#### III.4.1. General Description

In this section,  $N$  is treated as a function of  $x, k$ , and  $\theta$ . The governing equation (2.105) of Section II.2.1. can be simplified, since the  $y$ -derivatives vanish. Thus it can be written as

$$\frac{\partial N}{\partial t} + c_g \cos \theta \frac{\partial N}{\partial x} - \frac{\partial \sigma}{\partial x} \left( \frac{\partial N}{\partial k} \cos \theta - \frac{1}{k} \frac{\partial N}{\partial \theta} \sin \theta \right) = 0 \quad (3.23)$$

#### III.4.2. Grid Development

The  $\theta$ -grid is determined with an initial value of 24 directions, which implies that  $\Delta\theta = 15^\circ$ .

The initial x-grid is determined in such a way that the same  $dh/dx$  as in Section III.3.3. is obtained, with depths going from 50 m to 3.2 m, and the  $x$ -distance divided into 30 intervals.

In order to compute  $\Delta k$ , after choosing standard parameters for the JONSWAP spectrum,  $k_{\max}$  and  $k_{\min}$  were determined ( where the spectrum reaches almost a zero value and using (2.99)) and this interval was divided into 20 intervals, so as to have a reasonable initial resolution. The JONSWAP parameters are:  $\gamma = 3.3$  and  $\sigma_m = 0.6$  Hz, and the values  $k_{\max} = 0.135 \text{ m}^{-1}$  and  $k_{\min} = 0.007 \text{ m}^{-1}$  were chosen.

### III.4.3. Stability Analysis

The stability analysis is made by extension of the one made in III.3.4. Now the amplification function  $f$  is

$$|f|^2 = \left[ 1 - c_g \cos \theta \frac{\Delta t}{\Delta x} (1 - \cos \beta_1 \Delta x) + \frac{\partial \sigma}{\partial x} \cos \theta \frac{\Delta t}{\Delta k} (1 - \cos \beta_2 \Delta k) - \frac{\partial \sigma}{\partial x} \sin \theta \frac{1}{k} \frac{\Delta t}{\Delta \theta} (1 - \cos \beta_3 \Delta \theta) \right]^2 + \left[ c_g \cos \theta \frac{\Delta t}{\Delta x} \sin \beta_1 \Delta x - \frac{\partial \sigma}{\partial x} \cos \theta \frac{\Delta t}{\Delta k} \sin \beta_2 \Delta k + \frac{\partial \sigma}{\partial x} \sin \theta \frac{1}{k} \frac{\Delta t}{\Delta \theta} \sin \beta_3 \Delta \theta \right]^2 \quad (3.24)$$

Then  $\Delta t$  is again determined with  $|f| < 1$ , obtaining

$$\frac{1}{\Delta t} > c_g \cos \theta \frac{1}{\Delta x} - \frac{\partial \sigma}{\partial x} \cos \theta \frac{1}{\Delta k} + \frac{\partial \sigma}{\partial x} \sin \theta \frac{1}{k} \frac{1}{\Delta \theta} \quad (3.25)$$

#### *III.4.4. Treatment of the Boundary Conditions*

After fixing values for  $k_i$  that belong to the interval  $k_{\min}-k_{\max}$ , the corresponding values of  $\sigma$  can be computed, which together with the value of  $\theta$  lead to the calculation of the JONSWAP spectrum, which was then spread with the cosine square function described in Chapter II, equation (2.55). To compute  $N$  the equation (2.99) is employed.

#### *III.4.5. Results*

In a procedure similar to the one of Section III.3.6., different alternatives were tried for this formulation one at a time, to look for the different behaviours. Also, the exact solution obtained from (2.107) and (2.99) is shown.

In order to see the evolution of the action while travelling toward shore, Figures (21), (22), (23) and (24) were drawn for the exact solution. Each one shows the action plot in the  $k - \theta$  domain for 4 different  $x$ -grid points: one in deep water, one in shallow water, and two others between them (i.e. intermediate water). It can be seen that the action moves toward higher values of  $k$  (which implies a smaller wavelength), and gets less spread in the  $\theta$ -direction (which means that turns toward shore), while it is approaching shallower water.

Figures (25), (26), (27) and (28) are the plots of the evolution of the action under the same conditions and for the same cases as the previous set of plots, but now obtained from the numeric solution. Comparing these results with the exact ones shown before, it can be observed that the action is more spread along the  $k$ -domain, showing lower peak values. This behaviour is analyzed with the following sets of Figures.

To see the effect of being more accurate in the  $k$ -direction, a second order scheme for the  $k$ -derivative was tried. It can be appreciated from Figures (29), (30), (31) and (32) that the action distribution was not spread so much, and that the maximum value of the action  $N$  is not so low, which shows the importance of the  $k$ -direction, mainly in the region close to the peak of the curve of distribution of action, where the numeric derivatives are not accurate enough, due to the resolution.

Turning our attention to the  $\theta$ -space, a second order scheme for the  $\theta$ -derivative was tried, obtaining results similar to the ones of the second order scheme for  $k$ , which reinforces the concept of the importance of this domain, formerly seen in the  $\sigma - \theta$  formulation.

In an attempt to get even better results, in Figure (33) a third order scheme for the  $k$ -derivative is tried. It can be seen that a third order accurate scheme for the  $k$ -derivative produces oscillations, so no improvements can be obtained in this way, due to the shape of the action plot, which has strong changes in slope and curvature [17].

The fact of setting as an initial condition a curve smoother than the peaked JONSWAP one is to verify that the peak is a significant source of inaccuracies. For instance, if the curve  $N(k) = \sin \frac{k\pi}{k_{\max}}$  is tried instead of the action obtained from the JONSWAP formulation, comparisons to the exact solution show better agreement. This matches with the remarks made in the previous step. Figures (34), (35), (36) and (37) belong to the exact solution, while Figures (38), (39), (40) and (41) belong to the numeric prediction.

### III.5 EVOLUTION IN THE $(k_1, k_2)$ DOMAIN

#### III.5.1. General Description

In this section,  $N$  is treated as a function of  $x, k_1$  and  $k_2$ . The equation (2.103) of Chapter II results in a simpler one, since the derivatives with respect to  $y$  vanish. As a consequence, it is not necessary to calculate  $\frac{\partial N}{\partial k_2}$ , but it is still necessary the  $k_2$  direction due to the presence of  $\cos \theta$  (i.e.  $\cos \theta = \frac{k_1}{(k_1^2 + k_2^2)^{1/2}}$ ) in the governing equation.

Consequently, equation (2.103) from Section II.2.1. becomes

$$\frac{\partial N}{\partial t} + c_g \cos \theta \frac{\partial N}{\partial x} - \frac{\partial \sigma}{\partial h} \frac{\partial h}{\partial x} \frac{\partial N}{\partial k_1} = 0 \quad (3.26)$$

### III.5.2. Grid Development

The same initial  $x$ -grid as in section III.4.2. for the  $(k, \theta)$ -space was elected.

The  $k$ -grid is determined in the same way as in Section III.4.2., but now the total interval was divided into 10 intervals for  $\Delta k_1$ . After this,  $\Delta k_2$  was chosen equal to  $\Delta k_1$ .

### III.5.3. Stability Analysis

If the equation (3.26) is differenced, and then the same procedure as in III.3.4. is followed, the new amplification function is

$$|f|^2 = \left[ 1 - c_g \cos \theta \frac{\Delta t}{\Delta x} (1 - \cos \beta_1 \Delta x) + \frac{\partial \sigma}{\partial x} \frac{\Delta t}{\Delta k} (1 - \cos \beta_2 \Delta k) \right]^2 + \left[ \frac{\partial \sigma}{\partial x} \frac{\Delta t}{\Delta k} \sin \beta_2 \Delta k - c_g \cos \theta \frac{\Delta t}{\Delta x} \sin \beta_1 \Delta x \right]^2 \quad (3.27)$$

Again with the restriction that  $|f| < 1$ ,  $\Delta t$  can be fixed with

$$\frac{1}{\Delta t} > c_g \cos \theta \frac{1}{\Delta x} - \frac{\partial \sigma}{\partial h} \frac{\partial h}{\partial x} \frac{1}{\Delta k} \quad (3.28)$$

In this way, i.e. fixing  $\Delta x$ , and  $\Delta k$ , can obtain  $\Delta t$ .

### III.5.4. Treatment of the Boundary Conditions

As it was previously stated, a standard JONSWAP spectrum was chosen as the input energy, with the same parameters of Section III.4.2. Then it was distributed over the  $\theta$ -directions with the cosine square function (2.55).

Now the independent variables are  $k_1$  and  $k_2$  with which the correspondent values of  $\sigma$  and  $\theta$  are calculated and with the last ones, the value of the spectrum is computed.

With respect to the value of  $\frac{\partial N}{\partial k_1}$  for the first  $k_1$ , the approximation  $\frac{N_1}{\Delta k_1}$  was adopted for the first order accuracy scheme in the  $k$ -derivative.

### ***III.5.5. Results***

The results obtained in this space  $(k_1, k_2)$  are analogous to the ones of the previous space  $(k, \theta)$ . So the conclusions obtained before are valid here. The exact solution is computed by means of (2.107) and (2.99).

Figures (42), (43), (44) and (45) were drawn to see the behaviour of the exact solution. It can be seen that the action moves toward higher values of  $k_1$  (which implies a smaller wavelength), and gets less spread (which means that turns toward the shore) while it approaches shallower water. Some asymmetries of the contours can be found, it is supposed that they come from the graph process, since the the symmetry of the output files was checked.

Figures (46), (47), (48) and (49) were drawn to see the behaviour of the numeric solution. It can be seen that the action does not move enough, and besides its dispersion in the  $(k_1, k_2)$ -domain has a different configuration than the exact one. A constant  $k_1$ -grid requires a very big and not efficient increase of resolution to obtain improvements in the results, since only in the steep region of the action curve the resolution is needed, and

this steep region moves toward higher values of  $k_1$ , while reaching shallower water, as it has already been seen.

## CHAPTER IV

# EVOLUTION OF THE SPECTRUM ON A 2-D TOPOGRAPHY

## IV.1 GENERAL CONSIDERATIONS

After studying different alternatives of the governing equation for the one-dimensional bathymetry, a region in two-dimensions is now considered. The governing equation may be applied to any kind of bottom, as long as its shape does not vary with time.

In this chapter both a monochromatic initially unidirectional wave and a multidirectional spectrum passing over a submerged elliptical mound will be considered. No exact solution is available in this particular case, but experimental data from wave tank trials is available.

The action conservation equation will be solved numerically, and the results compared to the observations of the trials of [9]. In order to see what kind of improvements can be achieved with the formulation elected (according to the results of Chapter III), different grid resolution and different order of differentiation schemes are tried.

All the remarks in Section III.2. and Chapter II are valid in this Chapter.

## IV.2 EXPERIMENTAL INPUT INFORMATION

### *Experimental Conditions*

The shoal tests were conducted by Charles L. Vincent and Michael J. Briggs at the Coastal Engineering Research Center of the U.S. Army Corps of Engineers Waterways Experiment Station. The wave tank is 35 m wide by 29 m long. The bathymetry is uniform with no slope. The perimeter is lined with wave absorber frames to prevent adverse reflections. The tank is equipped with a directional spectral wave generator which is 27.43 m long, and consists of 60 paddles individually driven. The measurement area for this test is 6.10 m wide by 15.24 m long, and centrally located in front of the wave generator. An elliptical shoal was built in the tank. It has a major radius of 3.96 m and a minor radius of 3.05 m. The maximum height is 0.3048 m, and it was patterned after Berkhoff et al. [1]. Since the water depth is 0.457 m, the distance at the center of the shoal to still water level is 0.1524 m.

To get the experimental data, a straight transect was placed at 9 different locations. These 9 transects cover the mound and the region of main importance situated after it. The array is drawn in Figure (50). Each transect has 9 gages, spaced 0.76 m apart, in order to measure the wave amplitudes. An extra gage, (A), was located as a reference gage to measure incident wave conditions.

## IV.3 NUMERICAL COMPUTATIONS

### *Finite Difference Method Scheme*

For this 2-D case, the action  $A$  is considered as a function of  $x, y, \sigma$  and  $\theta$ . According to the explanation of Chapter II, the equation (2.94) is

$$\frac{\partial A}{\partial t} + \frac{\partial}{\partial x} (c_g \cos \theta A) + \frac{\partial}{\partial y} (c_g \sin \theta A) + \frac{\partial \theta}{\partial t} \frac{\partial A}{\partial \theta} + A \frac{\partial}{\partial \theta} \frac{\partial \theta}{\partial t} = 0 \quad (4.1)$$

For the Grid Development, the computational area chosen is 10 m wide by 15.8 m long. In this way both sides of the grid mesh and the incident front of the shoal have the flat bottom.

A reasonable first choice for  $\Delta\theta$  is  $30^\circ$ .

To choose  $\Delta x$  and  $\Delta y$  a mesh of 17 by 27 points (respectively) was employed, in order to get a spacing similar to the array of experimental gages as an initial attempt. In this way  $\Delta x = 0.625 \text{ m}$  and  $\Delta y = 0.608 \text{ m}$ .

For the Stability Analysis, the von Neumann procedure is followed, so in a way similar to Section III.3.4., the differentiation of the equation (4.1) yields

$$\begin{aligned}
A_{x,y,\theta}^{n+1} = & \left[ 1 - c_g \cos \theta \frac{\Delta t}{\Delta x} - c_g \sin \theta \frac{\Delta t}{\Delta y} - \left( \frac{\partial \sigma}{\partial x} \sin \theta - \frac{\partial \sigma}{\partial y} \cos \theta \right) \frac{1}{k} \frac{\Delta t}{\Delta \theta} - \right. \\
& - \left. \left( \frac{\partial \sigma}{\partial x} \cos \theta + \frac{\partial \sigma}{\partial y} \sin \theta \right) \frac{1}{k} \Delta t \right] A_{x,y,\theta}^n + \left[ c_g \cos \theta \frac{\Delta t}{\Delta x} \right] A_{x-1,y,\theta}^n + \\
& + \left[ c_g \sin \theta \frac{\Delta t}{\Delta y} \right] A_{x,y-1,\theta}^n + \left[ \left( \frac{\partial \sigma}{\partial x} \sin \theta - \frac{\partial \sigma}{\partial y} \cos \theta \right) \frac{1}{k} \frac{\Delta t}{\Delta \theta} \right] A_{x,y,\theta-1}^n
\end{aligned} \quad (4.2)$$

where the coefficients of the  $A_{i,j,k}$  terms are computed at the corresponding  $i,j,k$  grid point, and the superscript  $n$  stands for the time step.

After the necessary algebra, the amplification function obtained is

$$\begin{aligned}
|f|^2 = & \left[ 1 - \left( \frac{\partial \sigma}{\partial x} \cos \theta + \frac{\partial \sigma}{\partial y} \sin \theta \right) \frac{1}{k} \Delta t - c_g \cos \theta \frac{\Delta t}{\Delta x} (1 - \cos \beta_1 \Delta x) - \right. \\
& - c_g \sin \theta \frac{\Delta t}{\Delta y} (1 - \cos \beta_2 \Delta y) - \\
& - \left. \left( \frac{\partial \sigma}{\partial x} \sin \theta - \frac{\partial \sigma}{\partial y} \cos \theta \right) \frac{1}{k} \frac{\Delta t}{\Delta \theta} (1 - \cos \beta_3 \Delta \theta) \right]^2 + \\
& + \left[ c_g \cos \theta \frac{\Delta t}{\Delta x} \sin \beta_1 \Delta x + c_g \sin \theta \frac{\Delta t}{\Delta y} \sin \beta_2 \Delta y + \right. \\
& + \left. \left( \frac{\partial \sigma}{\partial x} \sin \theta - \frac{\partial \sigma}{\partial y} \cos \theta \right) \frac{1}{k} \frac{\Delta t}{\Delta \theta} \sin \beta_3 \Delta \theta \right]^2
\end{aligned} \quad (4.3)$$

$\Delta t$  can be determined from this last equation and  $|f| < 1$  after fixing  $\Delta x$ ,  $\Delta y$  and  $\Delta \theta$ . That is

$$\begin{aligned}
\frac{1}{\Delta t} > c_g \left( \cos \theta \frac{1}{\Delta x} + \sin \theta \frac{1}{\Delta y} \right) + \left( \frac{\partial \sigma}{\partial x} \sin \theta - \frac{\partial \sigma}{\partial y} \cos \theta \right) \frac{1}{k} \frac{1}{\Delta \theta} + \\
+ \left( \frac{\partial \sigma}{\partial x} \cos \theta + \frac{\partial \sigma}{\partial y} \sin \theta \right) \frac{1}{k}
\end{aligned} \quad (4.4)$$

In order to determine  $\Delta t$ , the maximum value of the right side of equation (4.4) has to be found. This happens at the edge of the shoal located at the extreme of its major axis, for the lowest frequency ( $\sigma$ ) and for  $\theta = 30^\circ$ .

With respect with the treatment of the Boundary Conditions, for this algorithm they were set according to the non-reflective sides of the basin. The wavemaker inputs energy at every direction that belongs to the half circumference that is in front of it. In this way the front side of the shoal takes all the spectral energy (which is distributed along this half circumference). The right and left sides only take part of this energy, due to the finite length of the wavemaker. For example, if one considers the farthest extreme of the wavemaker, the energy travelling in the direction perpendicular to it does not reach the shoal. The rear side of the shoal is considered open, since there is only leaving energy there (Figure 51).

#### IV.4 RESULTS

In this Section the output of some runs of the code under different conditions is shown. The purpose is not only to find a way to improve the results, but also to appreciate how the formulation behaves in other circumstances as for example shallower water, waves of very low and high frequencies, and steep and smooth distributed energy input.

With respect to the parameters chosen, in the case of the monochromatic wave, the frequency is  $\sigma = 4.83 \text{ Hz}$ , which corresponds to a period  $T = 1.3 \text{ s}$ , and no spreading

function is used, which means that  $\lambda = 0$  in equation (2.54). In the case of the spectral distribution,  $\sigma_m = 4.83 \text{ Hz}$  and  $\gamma = 2$  in equation (2.50).

The variables of the figures are dimensionless. The distances in the  $x$  and  $y$ -axis are normalized with  $R_o$ , which is the minimum radius of the shoal, and the wave heights,  $H$ , with the height measured at the reference gage (A).

Figures (52), (53) and (54) show the contour levels obtained from the trials, for a monochromatic initially unidirectional wave, and for two multidirectional spectrum cases respectively. The monochromatic case was chosen because the energy is totally concentrated in only one frequency and only one direction. The higher values of amplitudes are located in the region after the shoal (close to its edge) and at the center of the shoal (where the smallest depth is placed). Two pockets (depressions) are found after the shoal, one at each side of the region of high amplitude value. Figure (53) corresponds to the multidirectional spectrum case with parameters  $\gamma = 2$  in equation (2.50) and  $\lambda = 10$  in equation (2.54). In order to have smooth curves for the spectrum and spreading functions, Figure (54) was elected because it corresponds to parameter values  $\gamma = 2$  and  $\lambda = 30$ , in this way the energy is gently distributed in the  $\sigma - \theta$  directions. The higher amplitude values are located at two small regions (one at each side of the center of the shoal), and a third one at the center line, on top of the rear edge of the shoal. Small pockets are found on the left side of the measurement area. The amplitude values are not as pronounced as in the monochromatic case. These contours are as given in the paper [9].

Figures (55), (56) and (57) show the contour levels obtained with the same measurements of the trials, but in this case the data obtained from the gages was interpolated with the subroutine of SAS/Graph. Although these two sets of Figures (52) (53) (54), and (55) (56) (57) show similar qualitative pattern, from the discrepancies observed, such as the location of maximum and minimum amplitude values, and the numeric level values, it can be concluded that due to the sparsity of measurements points, no rigorous comparison by contour levels can be made. Consequently the comparison will also be made for specific individual transects.

Figures (58), (59) and (60) are contour levels obtained from the code, and give a quantitative idea of the output behaviour. Figure (58) is for the monochromatic wave. No small closed level curves are obtained at the center of the shoal, and at each side of the region after it. The region of higher amplitudes is closer to the center of the shoal and has lower values compared to the experimental curves. Figure (59) is the spectral case for  $\lambda = 10$ . The region of higher amplitudes is again closer to the center of the shoal, but it has the same values as in the experimental curves. The two small closed curves of levels  $H/H_0 = 1.2$  at the center of the shoal that appear in the empirical curves are not obtained. Figure (60) is the spectral case case for  $\lambda = 30$ . Instead of having three closed curves of levels  $H/H_0 = 1.2$  on the second half of the shoal, only one is obtained. Another difference with the experimental curves is that a big curve of level 1.0 takes the place of several smaller ones shown in the trial results.

Figures (61) and (62) show the comparison between the refraction of monochromatic waves of low and high frequency, respectively. For the low frequency a value

$\sigma = 3.3 \text{ Hz}$  is chosen, which gives the values  $kh = 0.78$  and  $L = 3.68 \text{ m}$  outside the shoal, and  $kh = 0.42$  and  $L = 2.27 \text{ m}$  at the center of the shoal. In this plot the high amplitude value region is located mainly at the second half of the shoal. For the high frequency, a value  $\sigma = 8 \text{ Hz}$  is chosen, which gives the values  $kh = 3.00$  and  $L = 0.96 \text{ m}$  outside the shoal, and  $kh = 1.20$  and  $L = 0.81 \text{ m}$  at the center of the shoal. In this plot the high value region is located after the rear edge of the shoal.

Figure (63) shows the effect of decreasing the water depth at the center of the shoal for the monochromatic wave case. The standard water depth at the center of the shoal is  $0.15 \text{ m}$ , and it was reduced to  $0.05 \text{ m}$ , which means a reduction of  $33 \%$ . With  $\sigma = 4.83 \text{ Hz}$ , this gives values  $kh = 1.07$  and  $L = 2.08 \text{ m}$  outside the shoal, and  $kh = 0.35$  and  $L = 0.90 \text{ m}$  at the center of the shoal. It can be seen that the shallower the water is, the greater the amplitude is, and the closer to the center of the shoal the peak is. It should be noticed that breaking may occur before these values are reached.

Figure (64) compares the basin data versus the numerical output along transect # 4 (i.e. a transverse section at  $x/R_0 = 2$ ) for the monochromatic unidirectional wave. It is observed that with the original resolution no good quantitative agreement is obtained. The numeric curve is smoother, not being able to reproduce the maximum and minimum peak values.

Figure (65) is again a comparison along transect # 4 of the monochromatic wave case, showing the effects of different alternatives tried to improve the previous results.

It is shown that higher resolution in the  $\theta$ -grid is a good way of getting closer results to the experimental data. This happens for the maximum peak, but not for the 2 minimum values.

Although more accurate results are obtained with a finer  $\theta$ -grid, the time involved in getting the necessary computations makes the calculation unfeasible for the purposes of an operational wave forecasting model.

Figures (66), (67) and (68) show the comparison between basin data and numerical predictions for the monochromatic wave case. Figure (66) corresponds to  $x/Ro = 0$ , i.e. a transverse section at the center of the shoal. One peak at the center longitudinal line is obtained instead of the two actual ones, one at each side. Figure (67) is taken at  $x/Ro = 1$ , i.e. a transverse section just on the rear edge of the shoal. One peak at the center line is obtained instead of a flat region of the tank data. Figure (68) belongs to the center line. The steep peak values are not reproduced by the numeric solution, and the high values found downstream, far from the shoal, are not followed even qualitatively. As it has been said before, this is the extreme case where all the energy is concentrated in only one frequency and only one direction initially. The coarse mesh employed is not fine enough to get reliable results.

Figures (69), (70), (71) and (72) show the comparison between basin data and numerical predictions for the spectral case of  $\lambda = 10$  at the same locations as before. In Figure (69),  $x/Ro = 0$ , a slight steep peak appears at the center line in the numeric prediction, but not in the experimental curve. In Figure (70),  $x/Ro = 1$ , one peak at the center line is seen instead of the two ones, one at each side, that correspond to the tank

data. In Figure (71),  $x/Ro = 2$ , a slight peak at the center line is observed in the code results, but a hump is obtained from the basin. In Figure (72), the center line, it is seen that the region of high heights is closer to the center of the shoal with the same height values. Although some discrepancies are still found in the comparison, they are not as large as in the monochromatic case.

Figures (73), (74), (75) and (76) are drawn for the spectral case of  $\lambda = 30$ . The same comparisons as above are done. Figure (73),  $x/Ro = 0$ , shows that the two slight peaks of the experimental results are not reproduced by the numerical prediction. For the others sections, i.e.  $x/Ro = 1$  shown in Figure (74),  $x/Ro = 2$  shown in Figure (75), and the center line shown in Figure (76), the agreement is quite good, showing only very small differences, due to the smoothness of the curves of the spectrum and spreading functions. It can be concluded that the method has a good performance for this kind of input energy.

**CHAPTER V**

## CONCLUSIONS

A method for computing the evolution of wave spectra, due to refraction and shoaling over 1-D and 2-D bathymetries, has been developed here. It has been tested under different conditions, and different devices were implemented to improve the numerical results.

The predictions are done in the  $(\sigma, \theta)$ -space, the  $(k, \theta)$  -space and the  $(k_1, k_2)$ -space, showing agreement in the results.

It is seen that the expansion of the  $x$  and  $y$  derivatives do not have significant importance, if trying to get more accurate output refining the respective mesh. On the other hand, the  $\theta$ -derivative is of fundamental importance, the results being sensitive to changes in its grid size. A relative coarse  $\theta$ -grid is the main obstacle for obtaining reliable forecasts for the case of monochromatic unidirectional waves. For this case lower peak values of energy are obtained at the correspondent bands, and some energy is obtained at other bands where no actual energy takes place. Other alternatives are tried to analyze the effect of the numeric dispersion of action due to the finite angular grid. For instance, higher order accuracy schemes and a smoother curve of the initial spec-

trum were run, leading to better results. In the case of smooth spectrum and spread functions, the results are very close to the actual 2-D values.

Either the polar or the rectangular  $k$ -domain has the extra complexity of the  $k$ -derivative. The shape of the initial spectrum curve brings numerical inaccuracies if it is peaked. In this case a third order accuracy scheme showed oscillations near the region of strong change in slope and curvature.

More sophisticated schemes may solve the kind of problems found in the  $\theta$  and  $k$ -spaces, as for example the Lax-Wendroff scheme or the method of interpolating the  $k$ -curve with a spline and then compute the derivatives analitically.

## REFERENCES

- <sup>1</sup> Berkhoff J.C.W., Booy N. and Radder A.C., "Verification of Numerical Wave Propagation Models for Simple Harmonic Linear Water Waves", *Coastal Engineering*, 6, (1982) 255-279.
- <sup>2</sup> Ebersole Bruce A., "Refraction-Diffraction Model for linear Water Waves", *Journal of Waterway, Port, Coastal and Ocean Engineering*, Vol. 111, No. 6, Nov. 1985.
- <sup>3</sup> Dean Robert G. and Dalrymple Robert A., "Water Wave Mechanics for Engineers And Scientists", Prentice Hall 1984.
- <sup>4</sup> Le Blond P.H. and Mysak L.A., "Waves in the Ocean", Elsevier Scientific Publishing Co. 1978.
- <sup>5</sup> Phillips O.M., "The Dynamics of the Upper Ocean", Cambridge University Press 1966.

- 6 Ochi Michel K., "Stochastic Analysis and Probabilistic Prediction of Random Seas", Coastal and Oceanographic Engineering Department University of Florida, UFL/COEL/TR-042.
- 7 Bouws E., Gunther H., Rosenthal W. and Vincent C.L., "Similarity of the Wind Wave Spectrum in Finite Depth Water", Journal of Geophysical Research", Vol.90, No.C1, Pages 975-986, January 20, 1985.
- 8 Kitaigorodskii S.A., Krasitskii V.P. and Zaslavskii M.M., "On Phillips Theory of equilibrium range in the spectra of wind-generated gravity waves", J. Phys. Oceanogr., 5, 412-413, 1975.
- 9 Vincent Charles L. and Briggs Michael J., "Refraction-Diffraction of Irregular Waves over a Mound", Unpublished work.
- 10 Bliss G.A., "Calculus of Variations".
- 11 Sakai Tetsuo, Koseki Masahiko and Iwagaki Yuichi, "Irregular Wave Refraction due to Current", Journal of Hydraulic Engineering, Vol. 109, No. 9, September 1983.
- 12 Karlson Thorbjorn, "Refraction of Continuous Ocean Wave Spectra", Journal of the Waterways and Harbors Division, No. WW4, Nov. 1969.

- 13 Le Mehaute Bernard and Wang John D., "Wave Spectrum Changes on Sloped Beach", Journal of the Waterway, Port, Coastal and Ocean Division, Vol. 108, No. WW1, Feb. 1982.
- 14 Schetz J.A., "Foundations of Boundary Layer Theory for Momentum, Heat and Mass Transfer", Prentice Hall, 1984.
- 15 Russell D., private communication.
- 16 Grossman B., private communication.
- 17 Walters R., private communication.
- 18 Marshall G., "Introduccion a la Solucion Numerica de Ecuaciones en Derivadas Parciales", Comision Nacional De Energia Atomica, Centro de Computos Cientifico, CNEA-AC 9/86, 1986.
- 19 Hughes O.F., "Ship Structural Design", The Society of Naval Architects and Marine Engineers, 1988.

# FIGURES

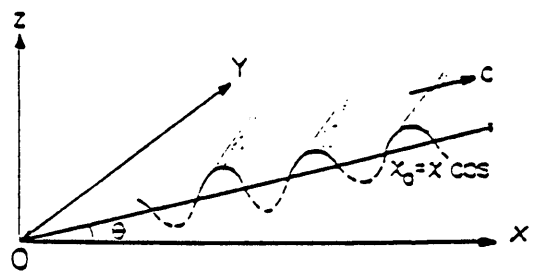


Figure 1. Spatial reference system

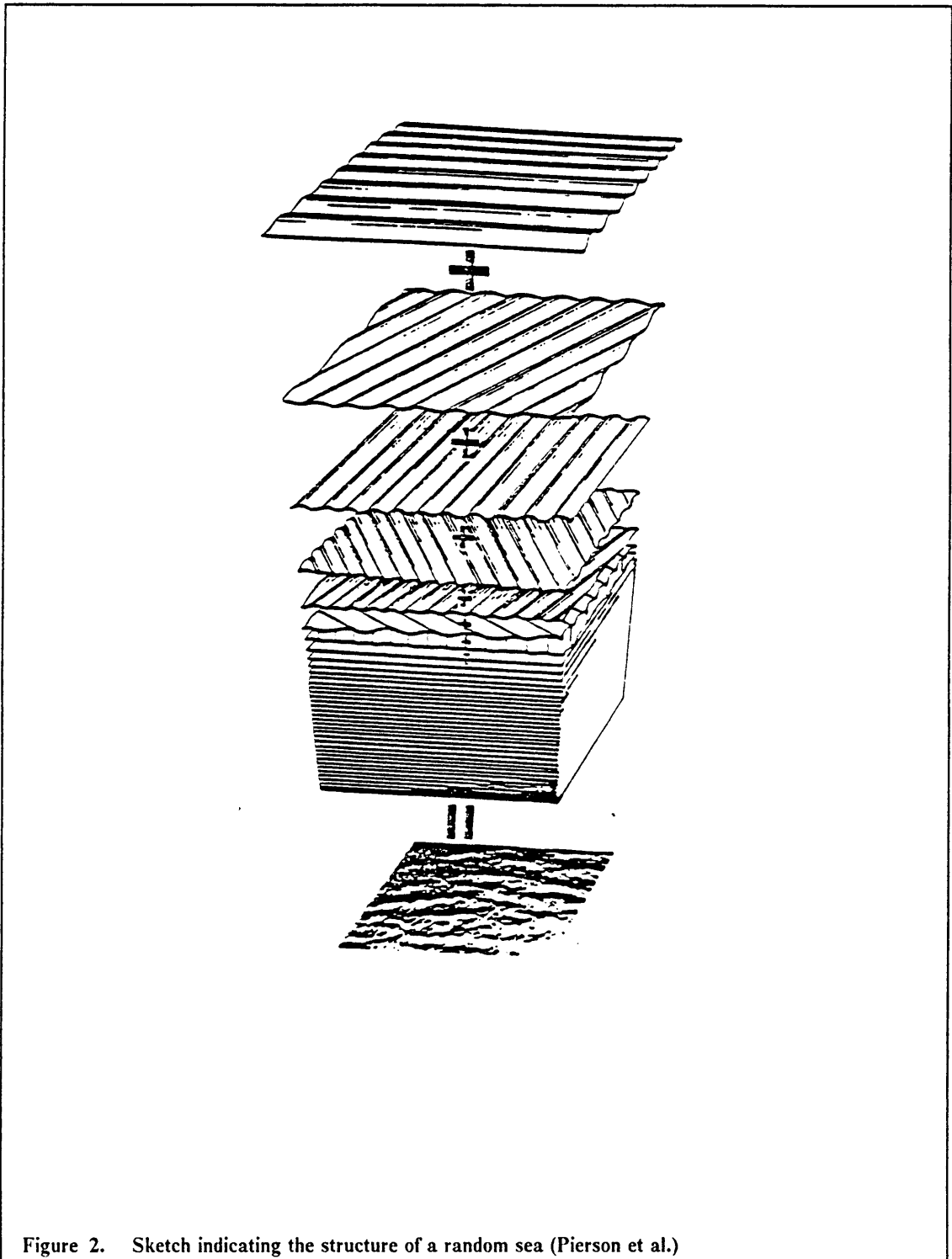


Figure 2. Sketch indicating the structure of a random sea (Pierson et al.)

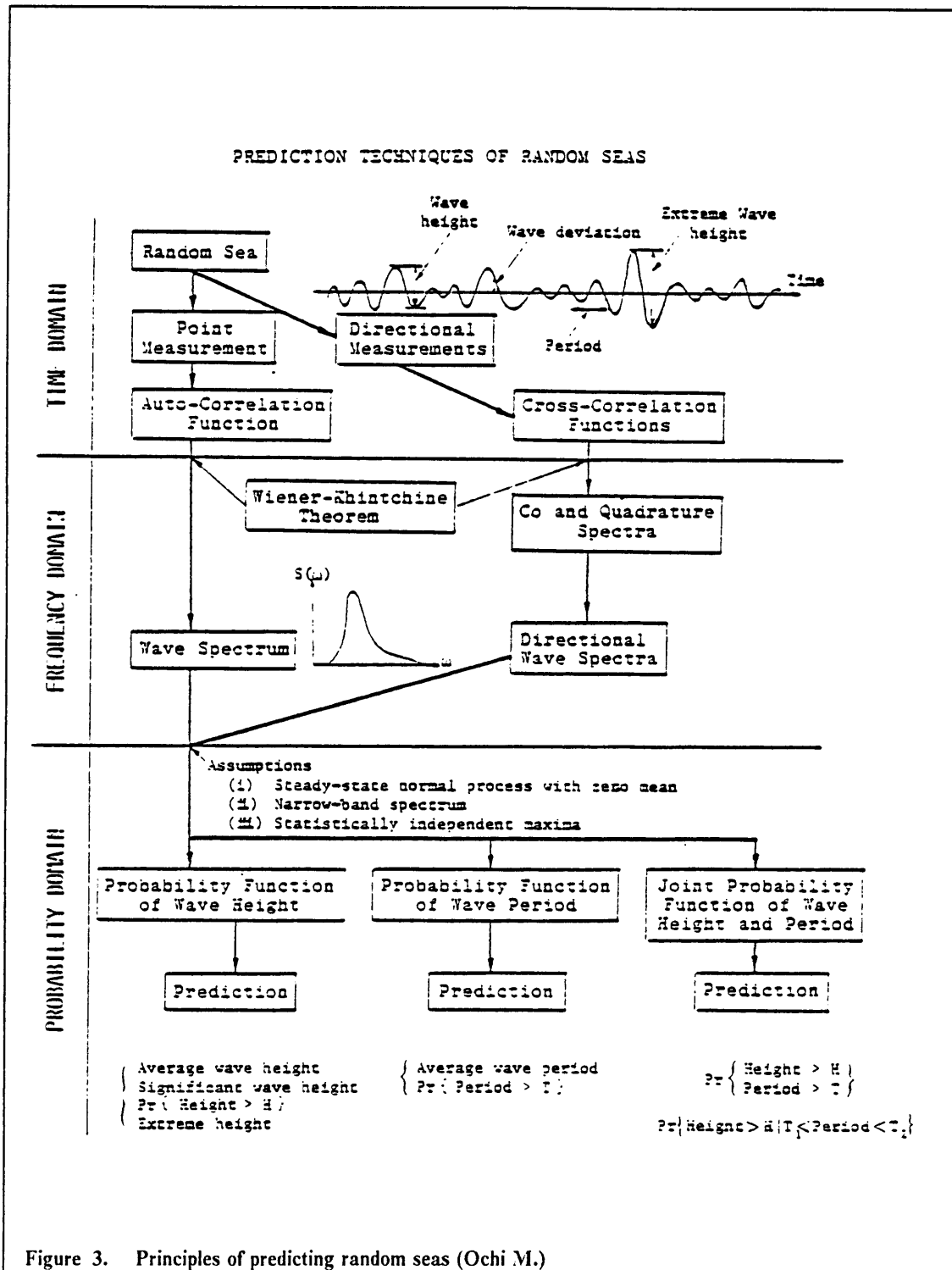


Figure 3. Principles of predicting random seas (Ochi M.)

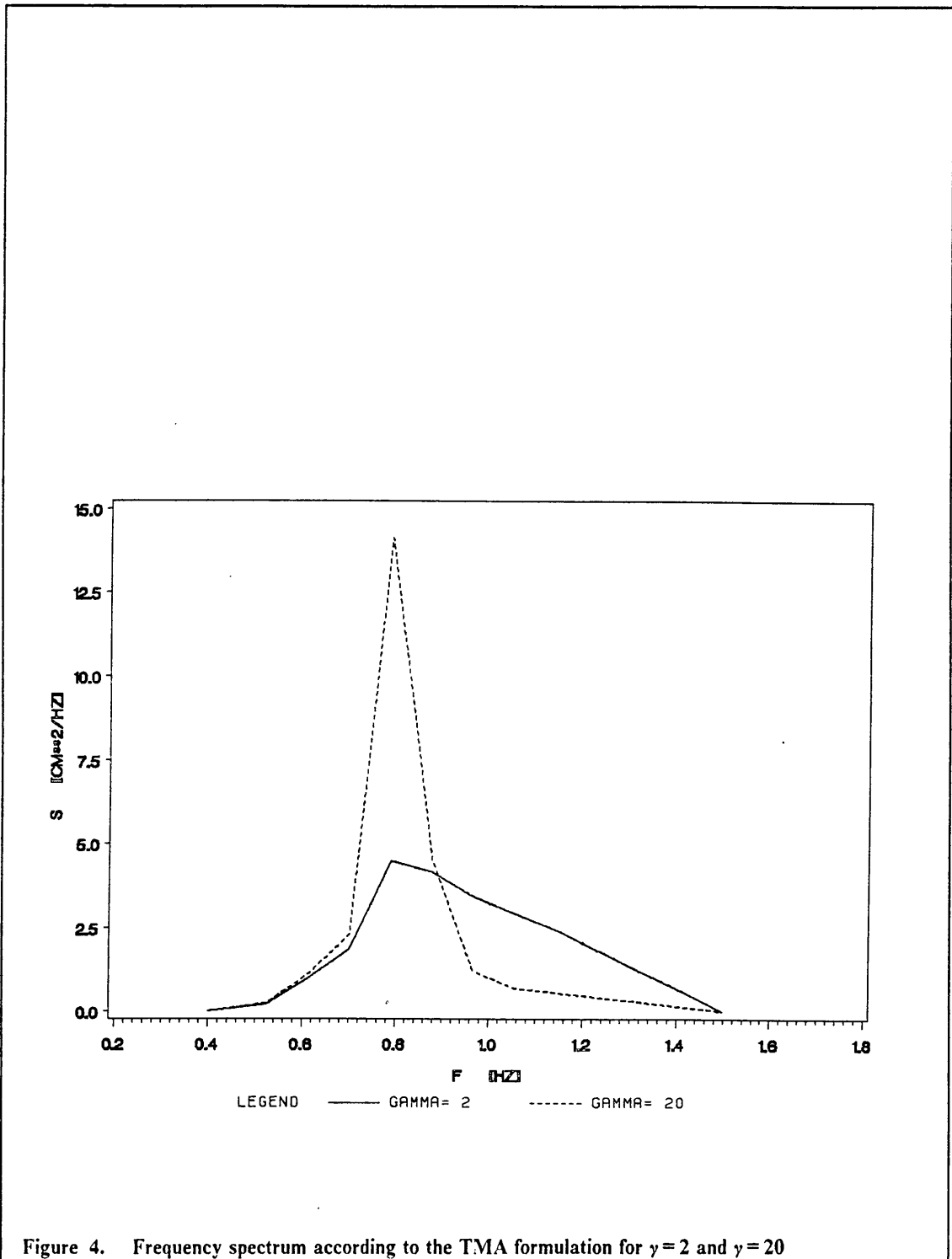


Figure 4. Frequency spectrum according to the TMA formulation for  $\gamma = 2$  and  $\gamma = 20$

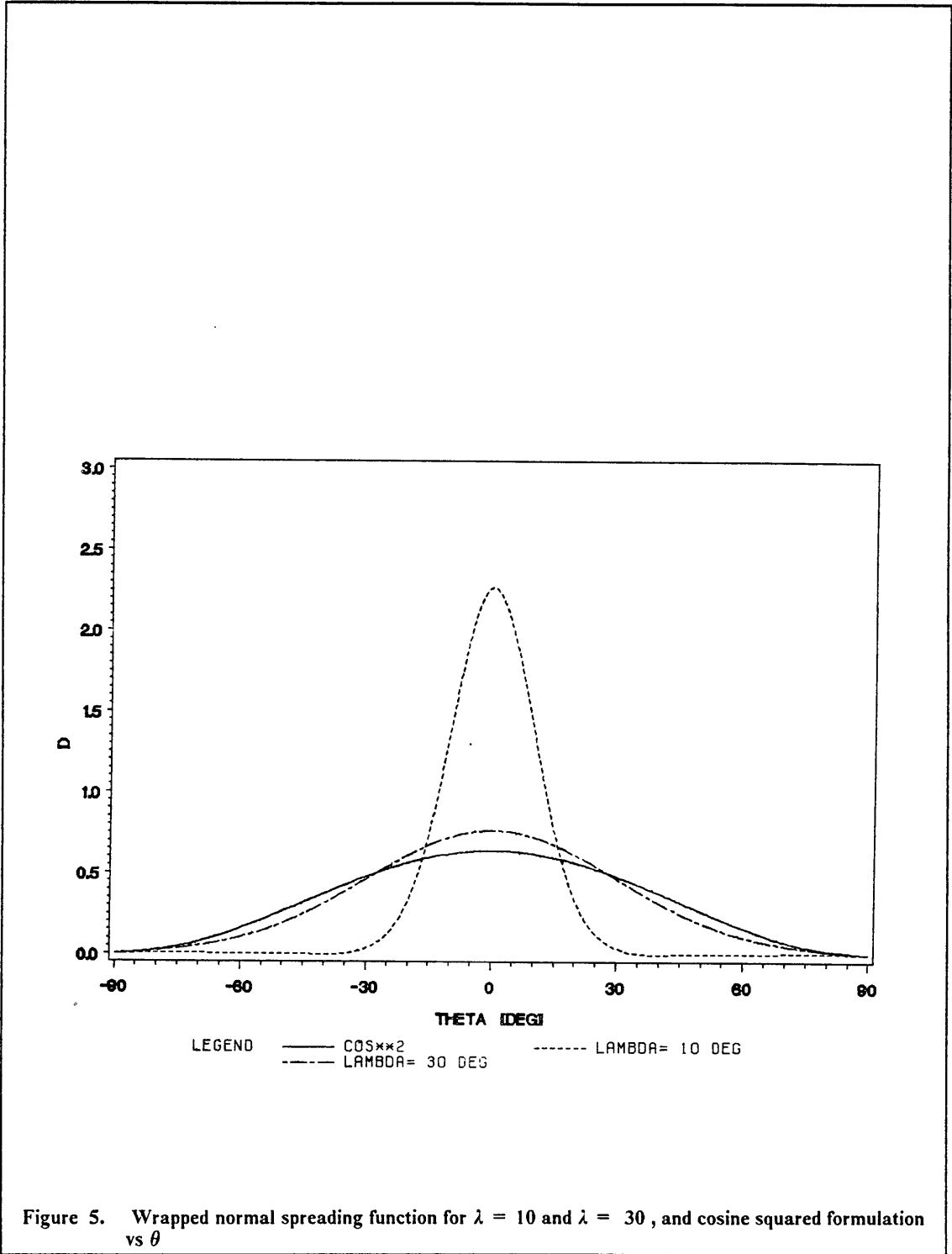


Figure 5. Wrapped normal spreading function for  $\lambda = 10$  and  $\lambda = 30$ , and cosine squared formulation vs  $\theta$

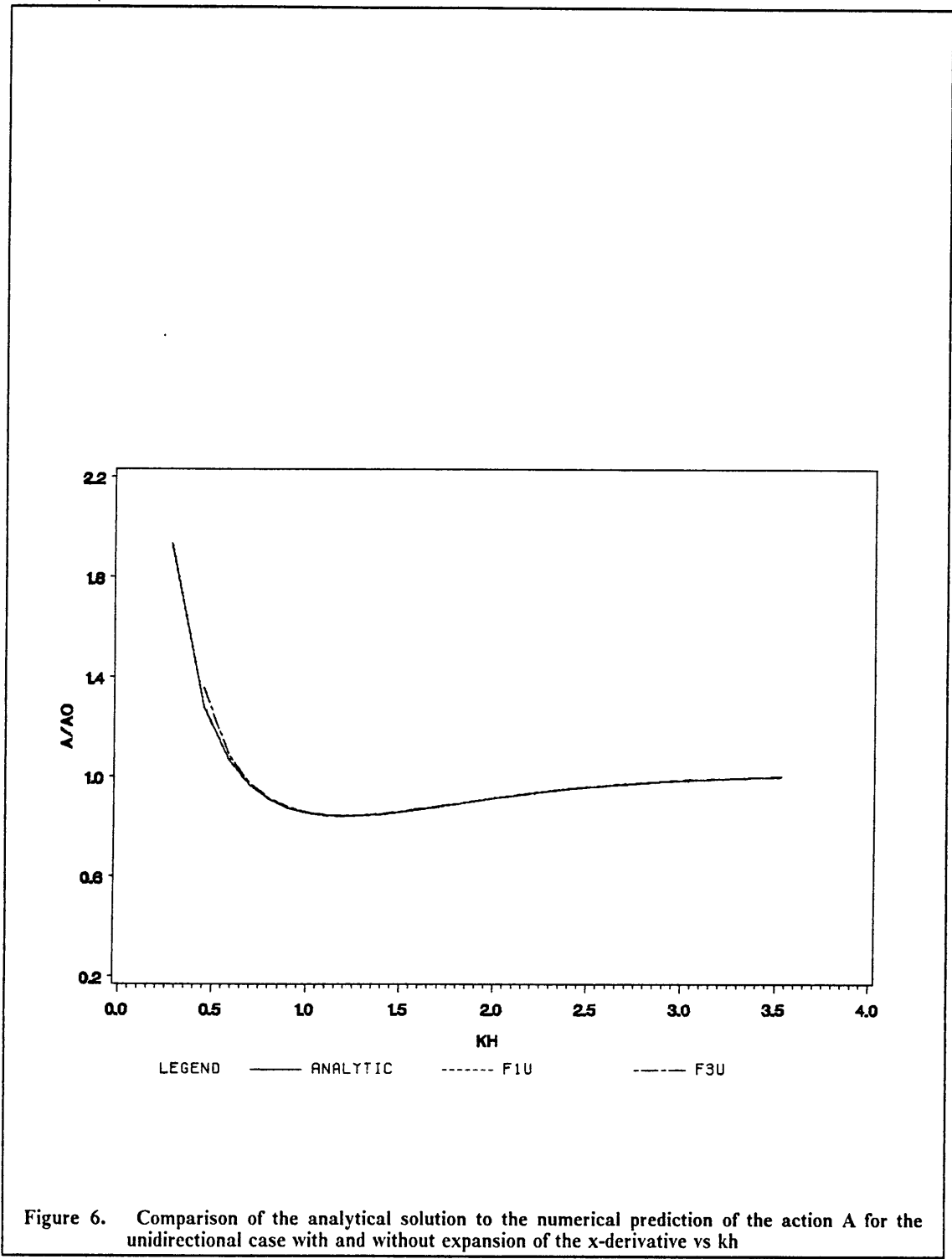


Figure 6. Comparison of the analytical solution to the numerical prediction of the action A for the unidirectional case with and without expansion of the x-derivative vs kh

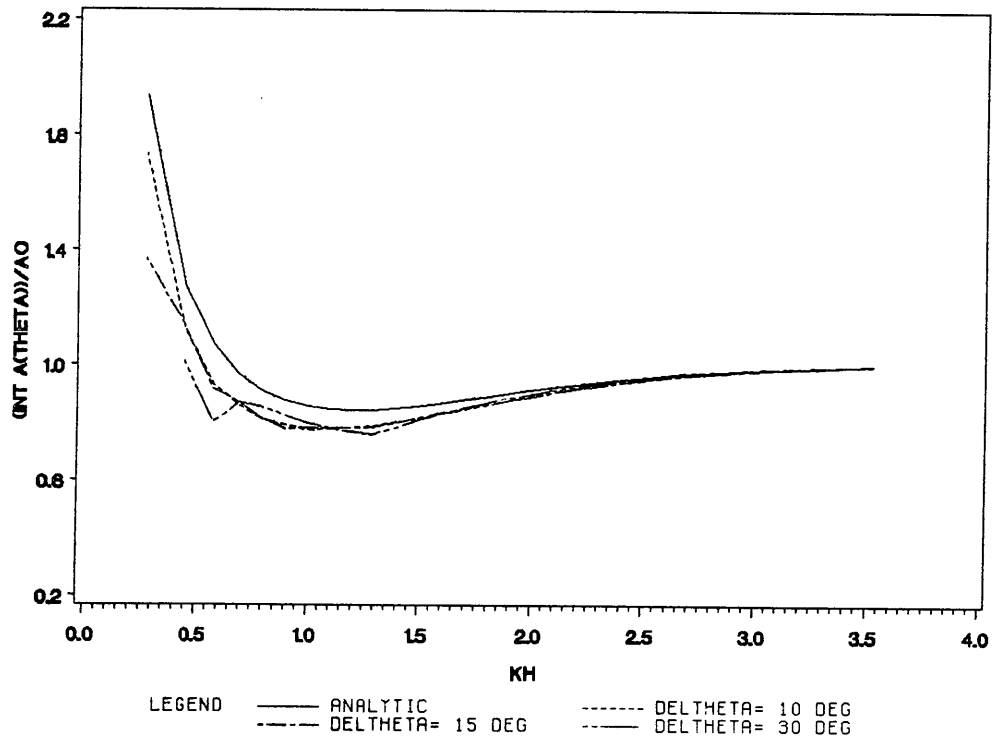
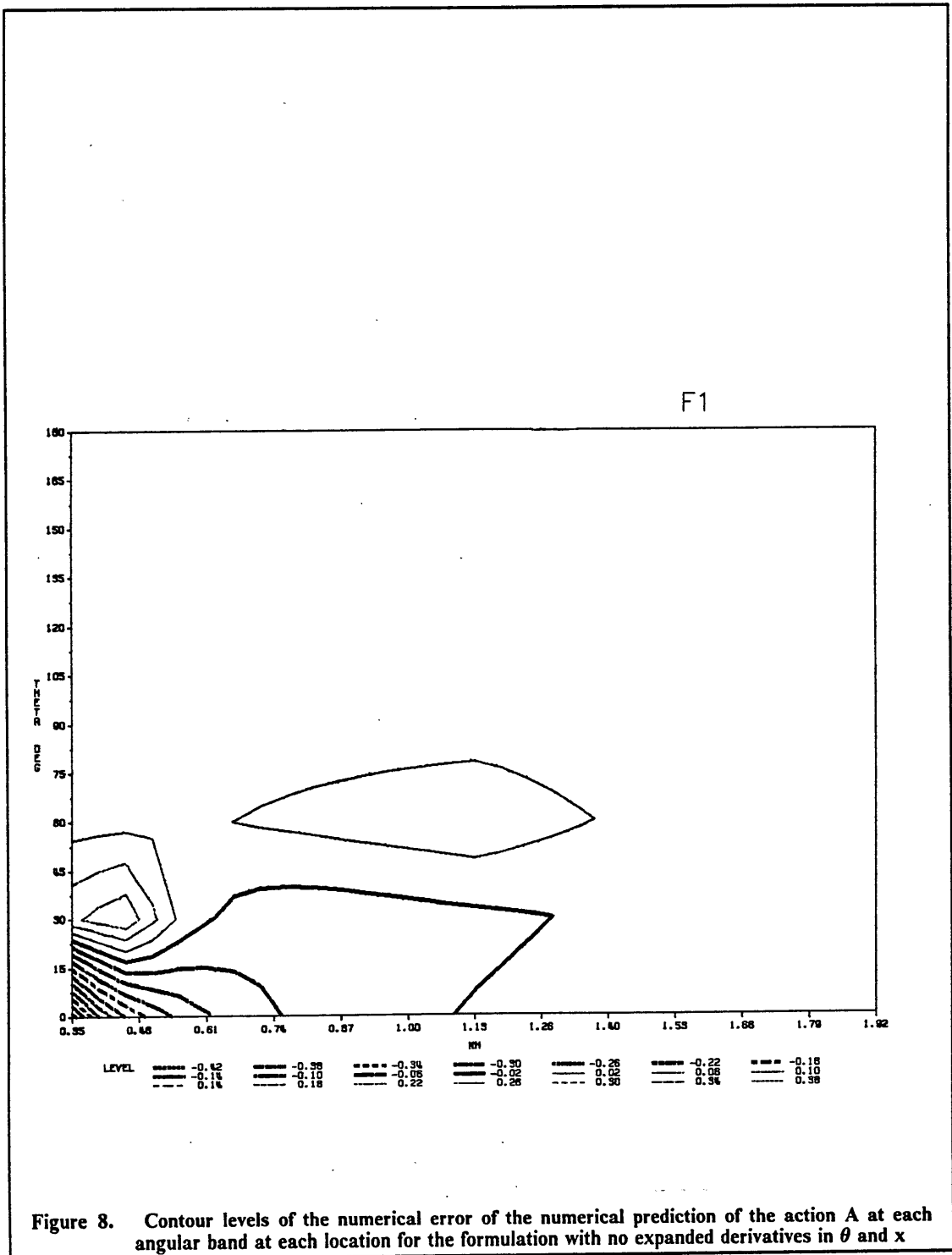


Figure 7. Comparison of the analytical solution to the numerical prediction of the integration of  $A(\theta)$  for different grid resolution in  $\theta$  vs  $kh$



F2

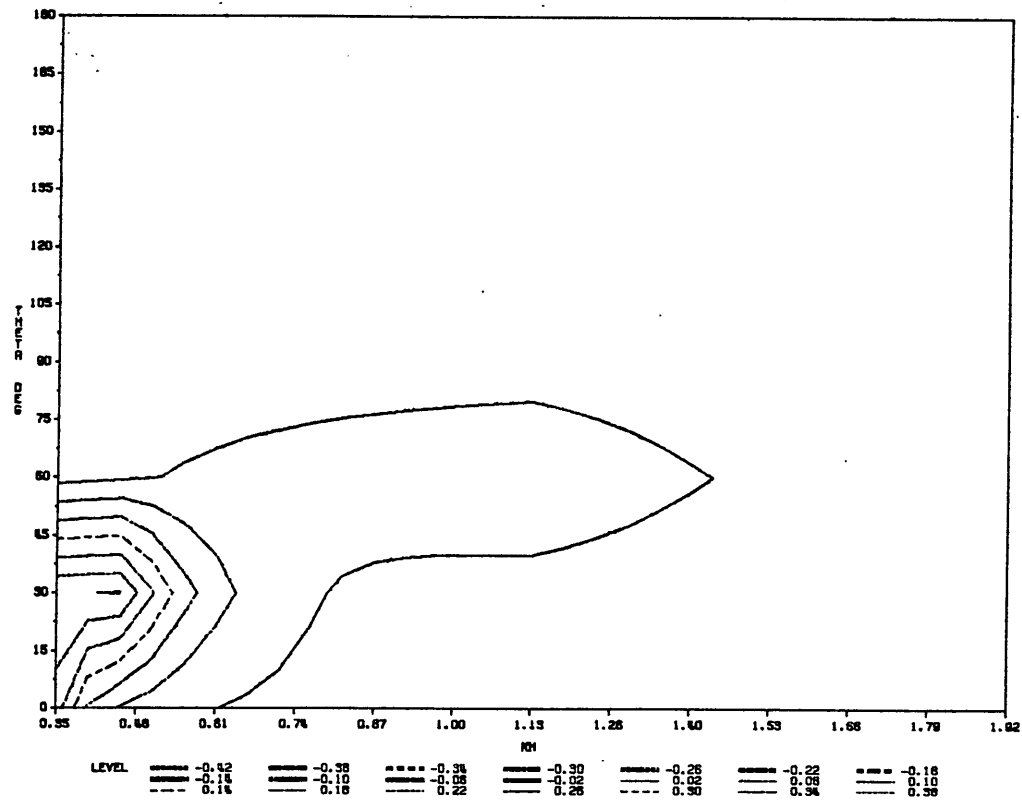
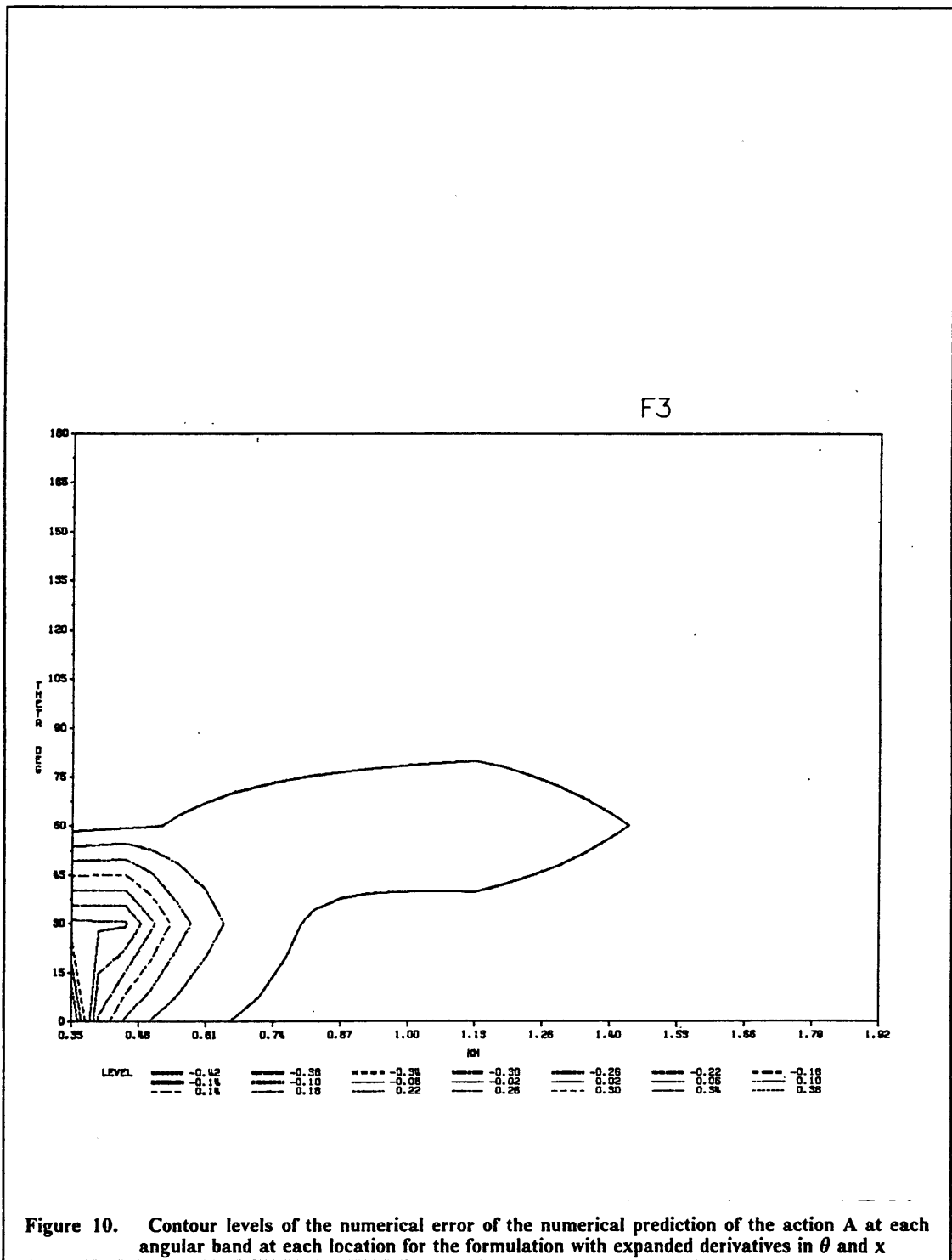


Figure 9. Contour levels of the numerical error of the numerical prediction of the action A at each angular band at each location for the formulation with expanded derivatives in  $\theta$



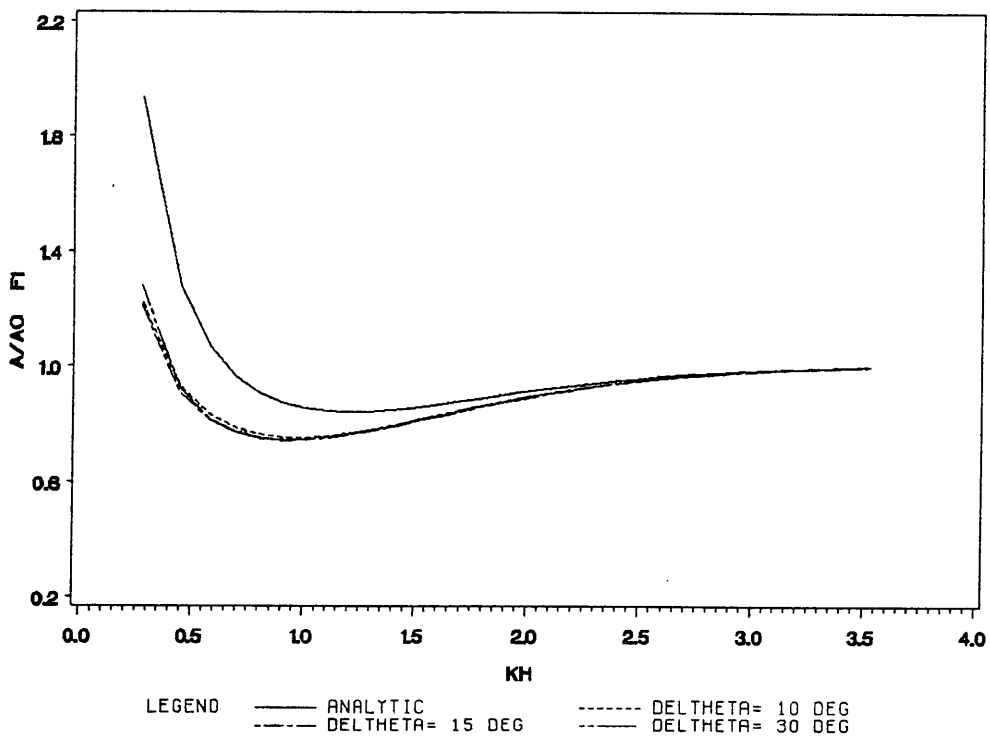


Figure 11. Comparison of the analytical solution to the prediction of the action A using different grid resolution in  $\theta$ , with no expanded derivatives in  $\theta$  and  $x$  vs  $kh$

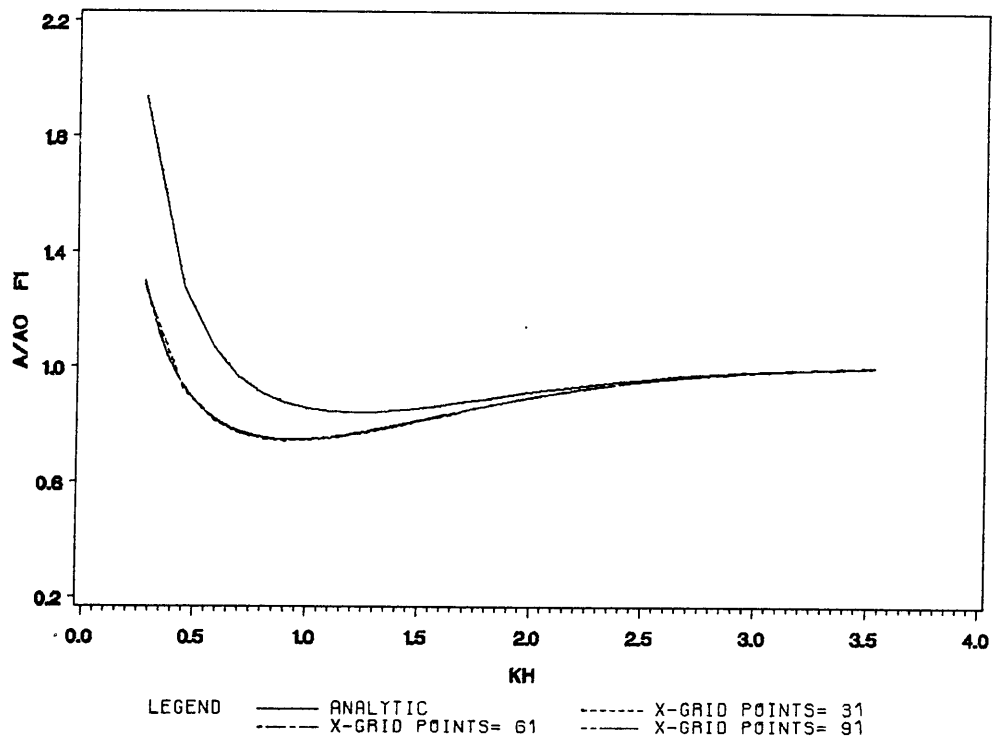


Figure 12. Comparison of the analytical solution to the numerical prediction of the action A using different grid resolution in x, with no expanded derivatives in  $\theta$  and x vs kh

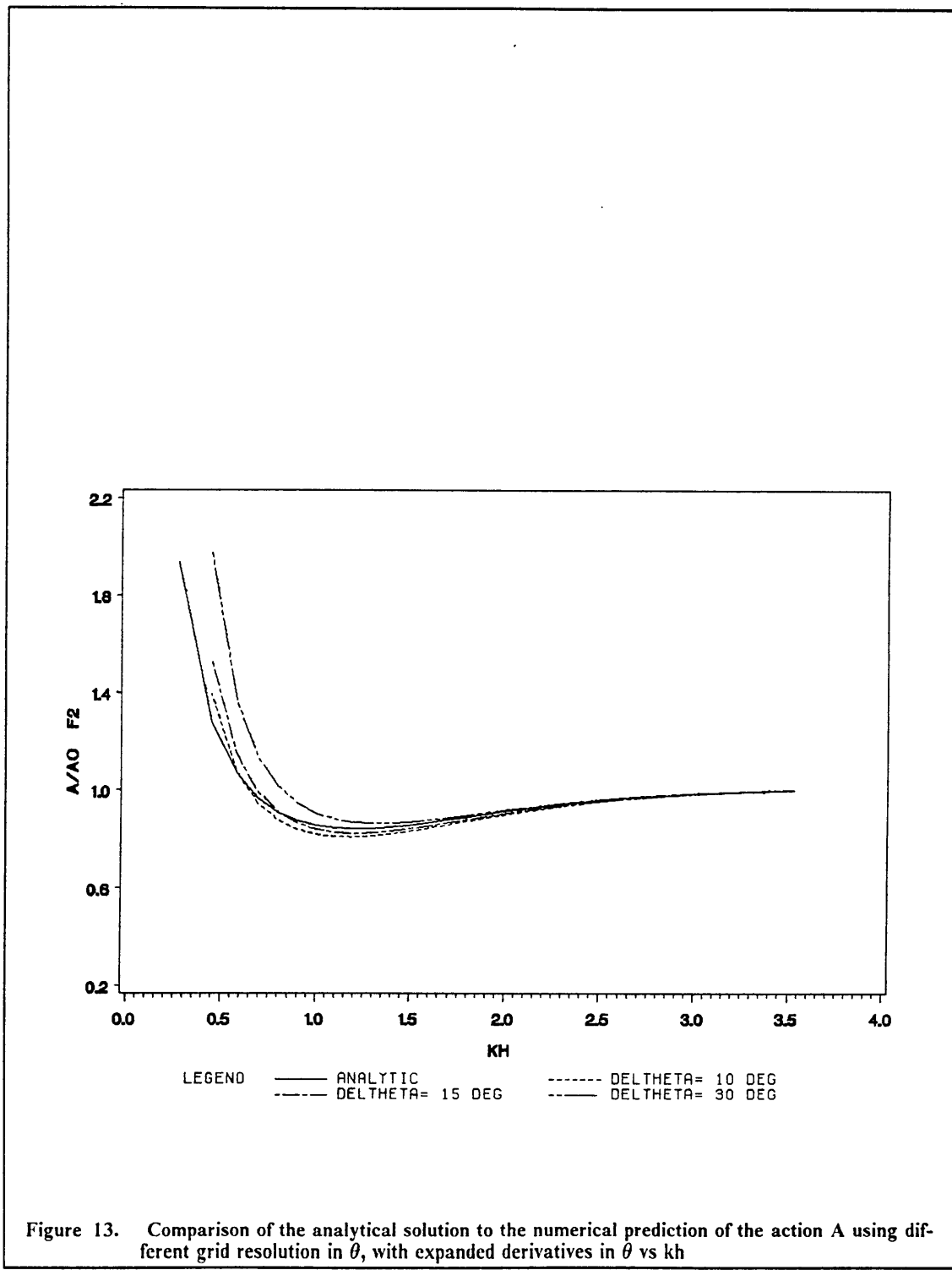


Figure 13. Comparison of the analytical solution to the numerical prediction of the action A using different grid resolution in  $\theta$ , with expanded derivatives in  $\theta$  vs  $kh$

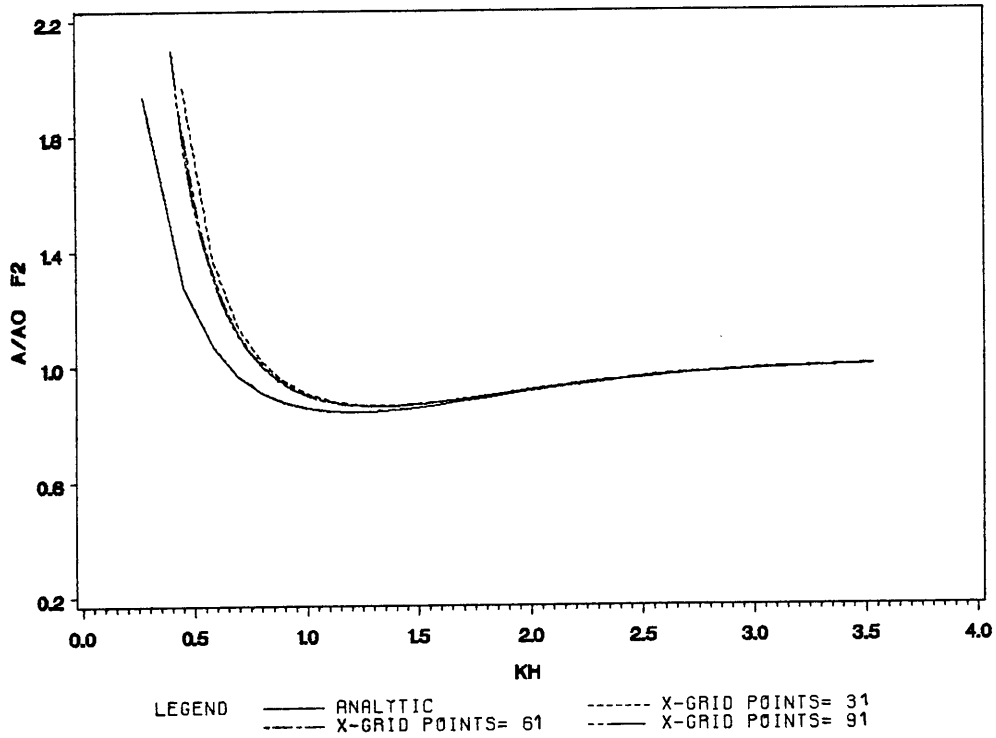


Figure 14. Comparison of the analytical solution to the numerical prediction of the action  $A$  using different grid resolution in  $x$ , with expanded derivatives in  $\theta$  vs  $kh$

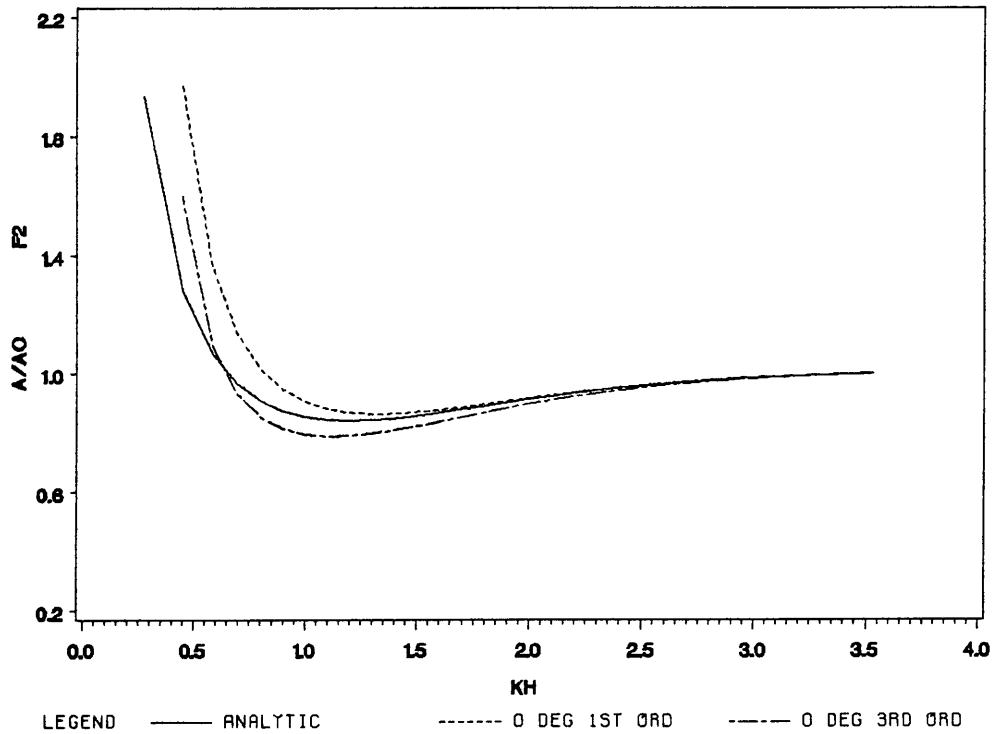
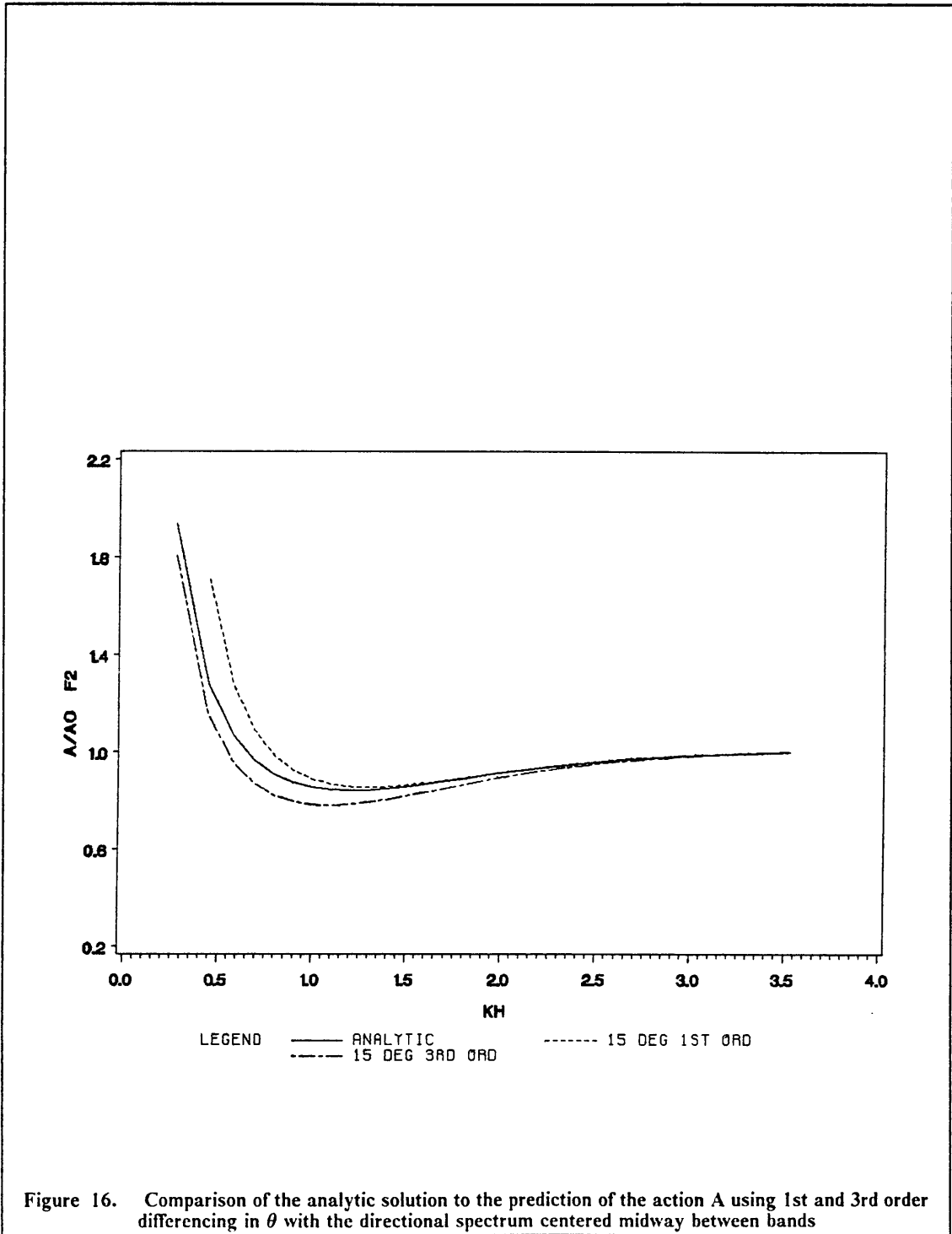
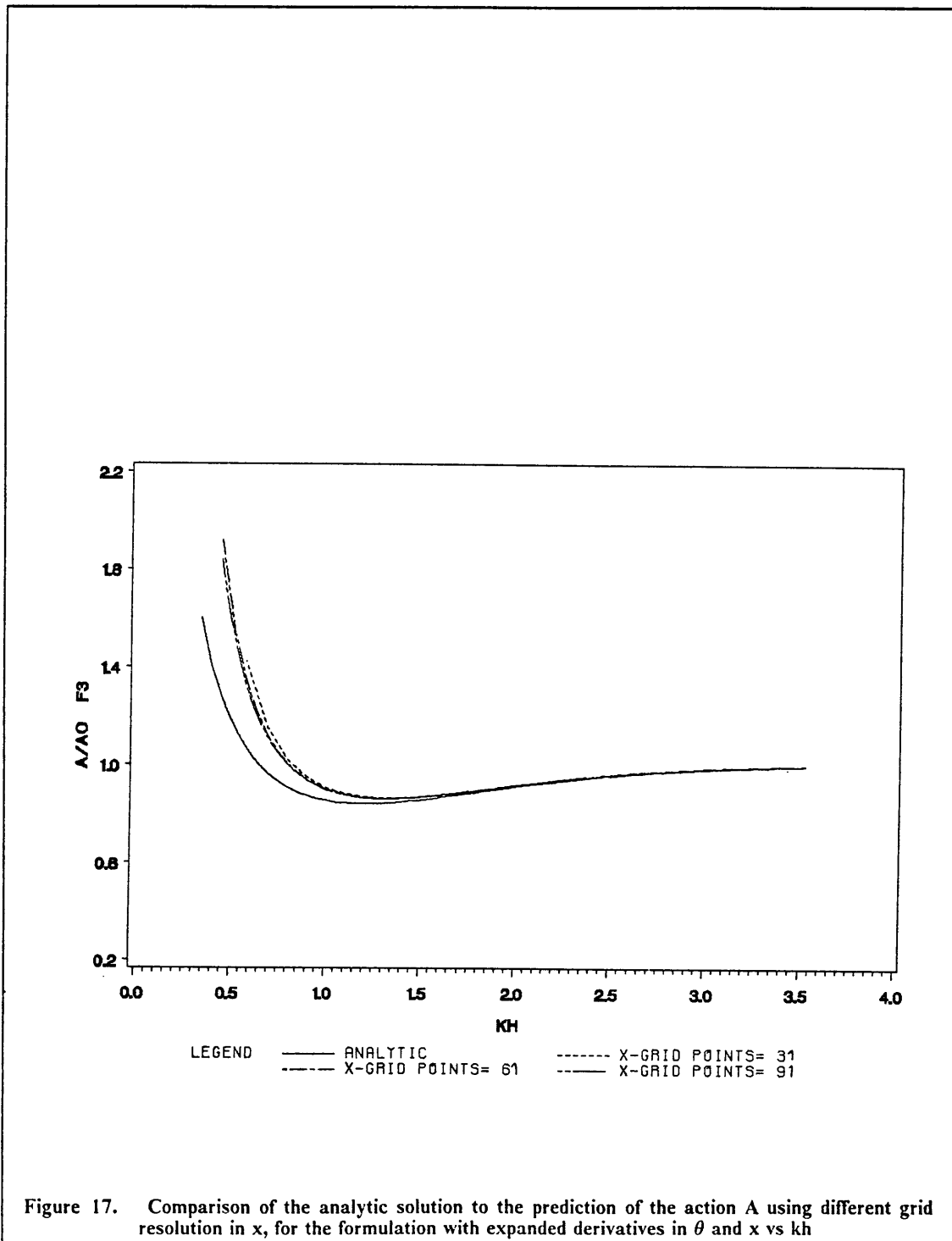


Figure 15. Comparison of the analytical solution to the numerical prediction of the action A using 1st and 3rd order differencing in  $\theta$ , with expanded derivatives in  $\theta$  vs  $kh$





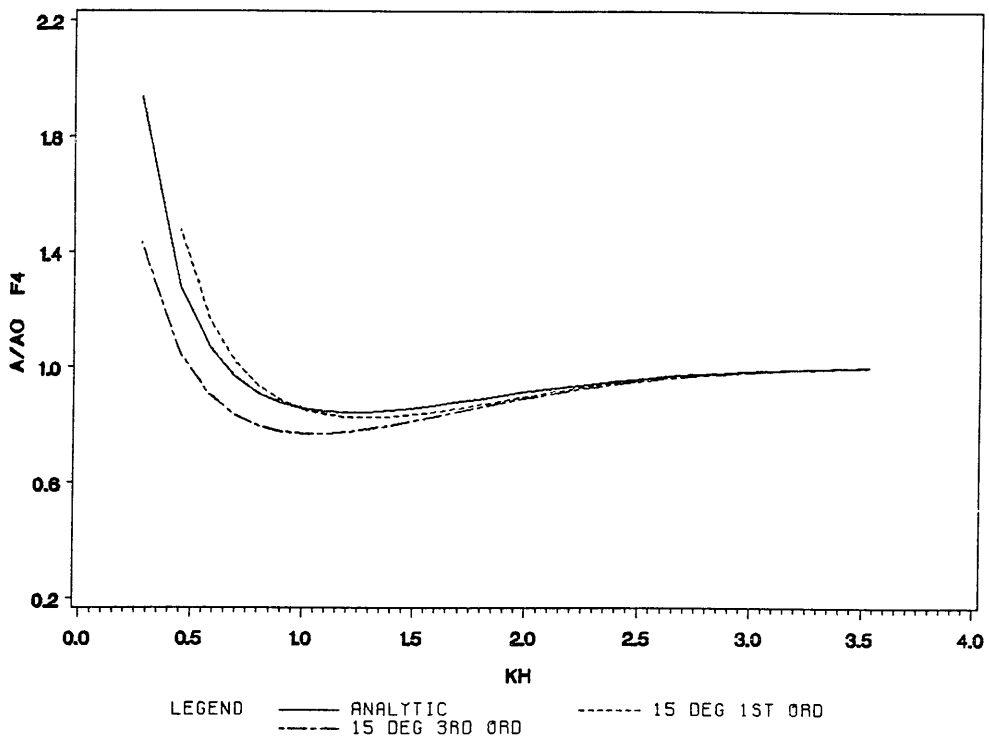
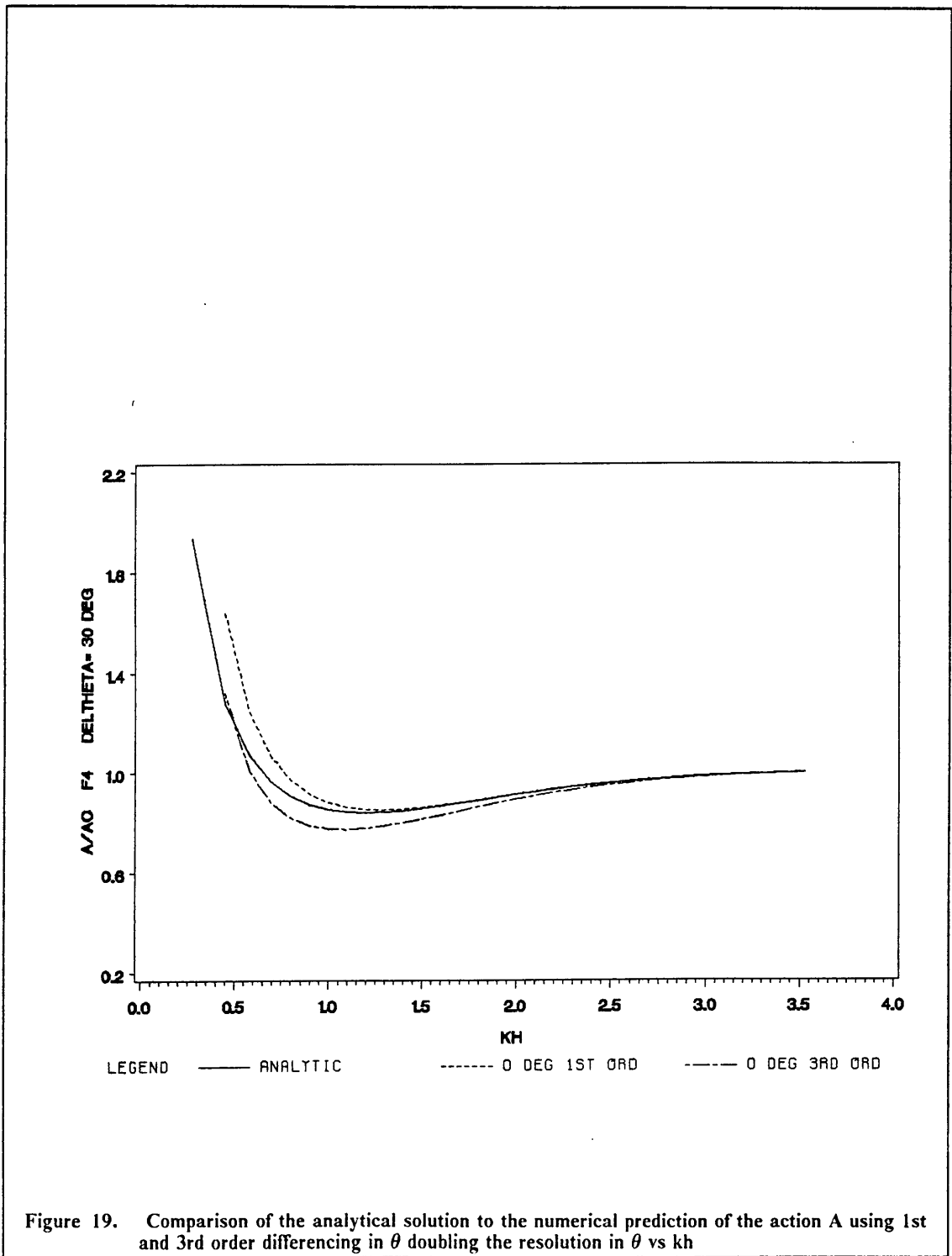
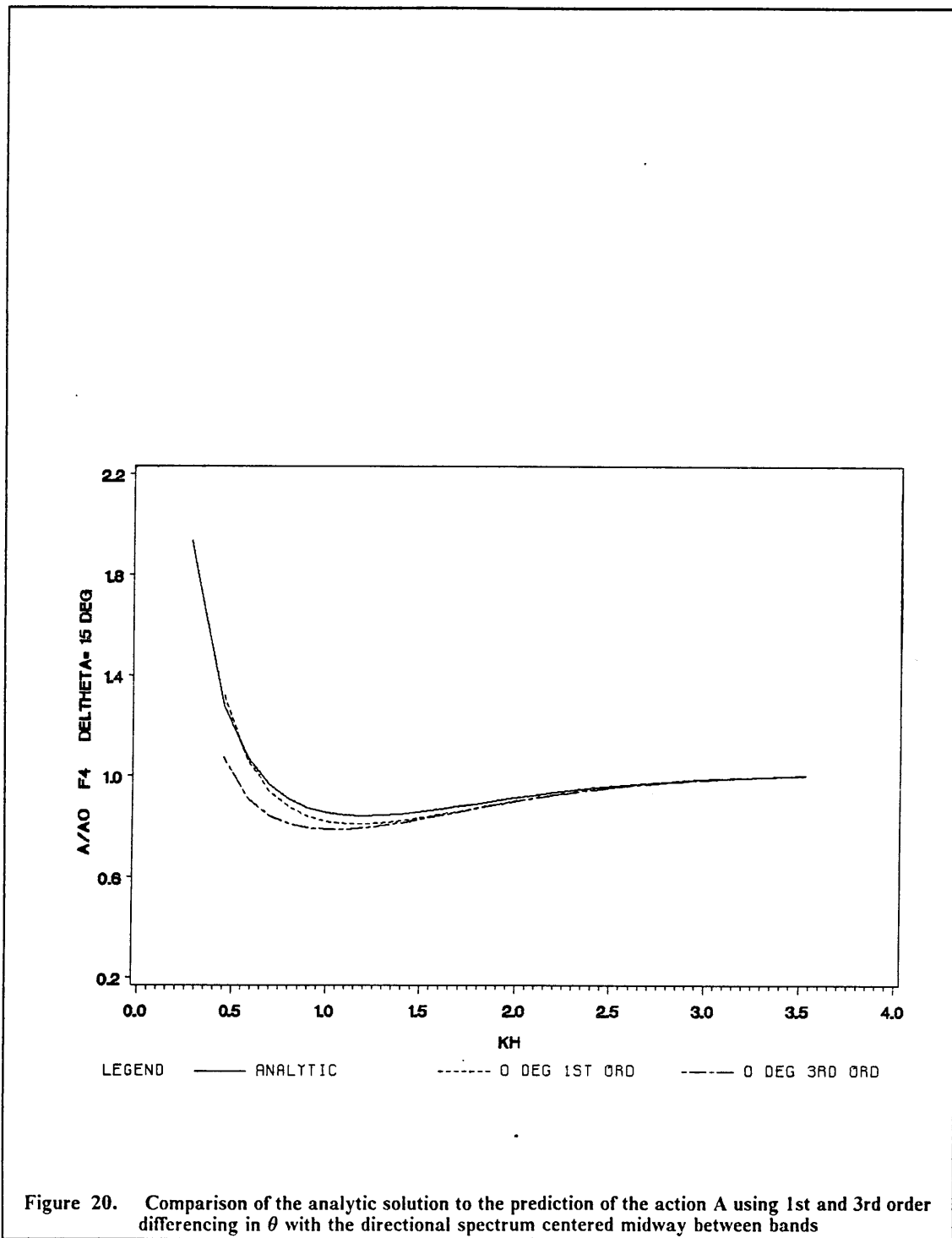


Figure 18. Comparison of the analytical solution to the numerical prediction of the action A using 1st and 3rd order differencing in  $\theta$  vs  $kh$





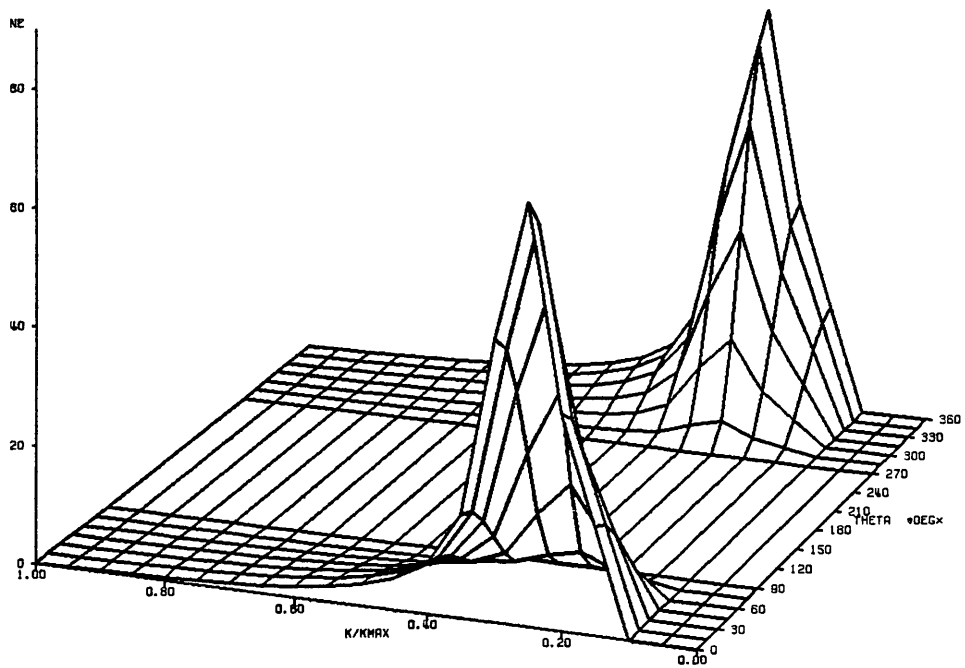


Figure 21. Analytical solution for the action  $N$  in the  $(k, \theta)$  space at  $x/L_0 = 0.035$

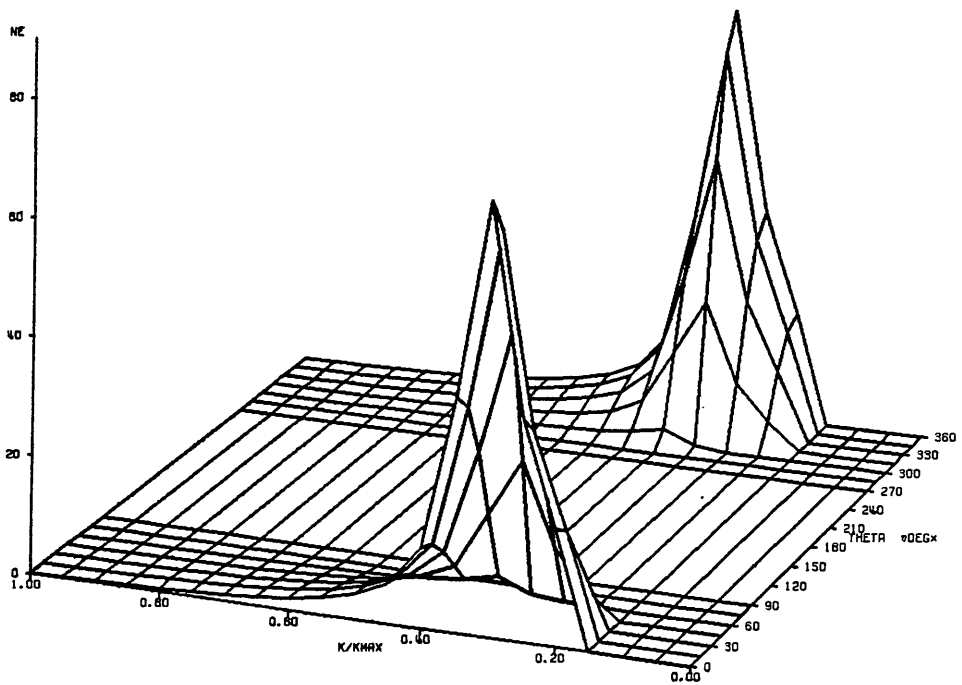


Figure 22. Analytical solution for the action  $N$  in the  $(k, \theta)$  space at  $x/L_0 = 0.520$

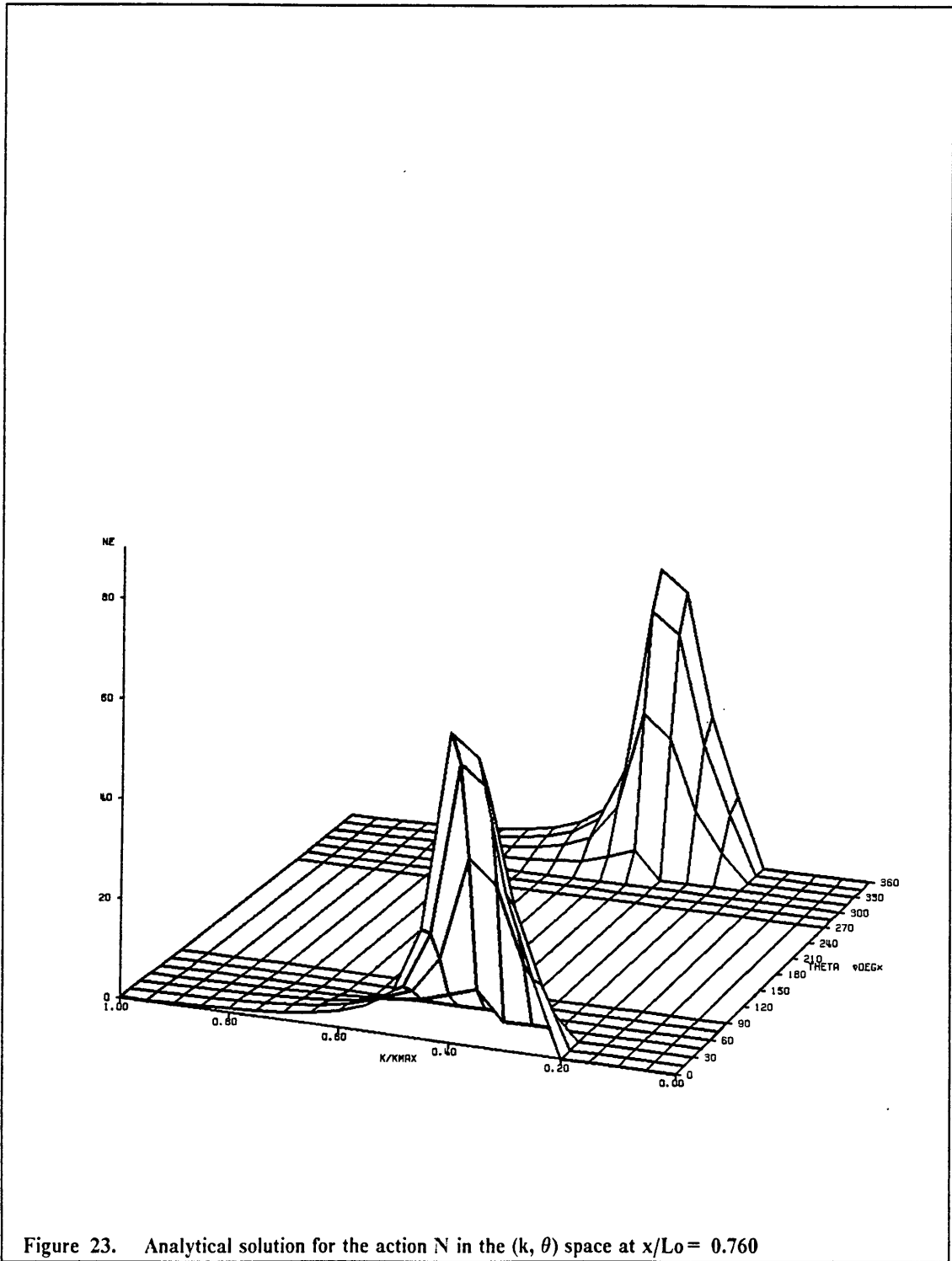


Figure 23. Analytical solution for the action  $N$  in the  $(k, \theta)$  space at  $x/L_0 = 0.760$

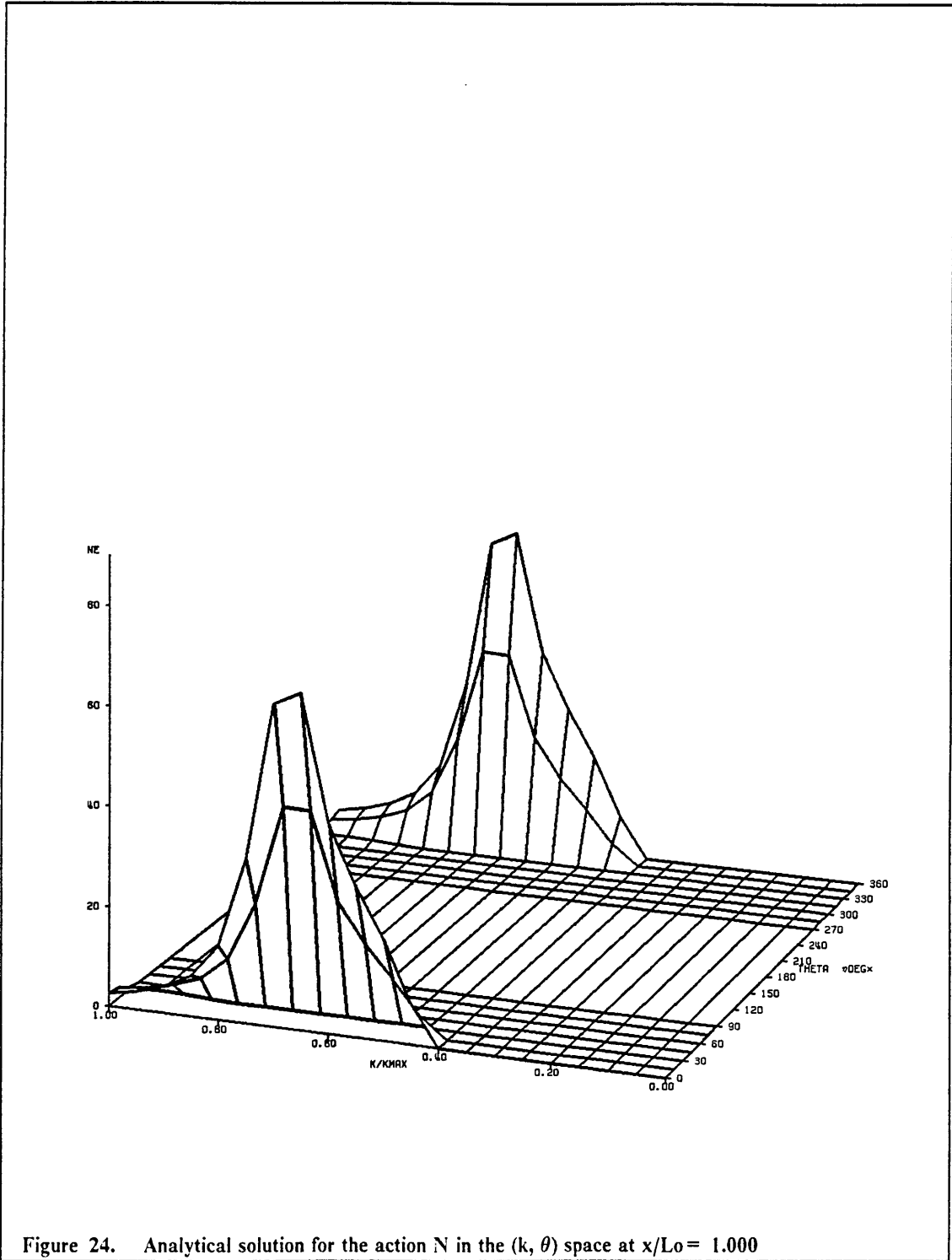


Figure 24. Analytical solution for the action  $N$  in the  $(k, \theta)$  space at  $x/L_0 = 1.000$

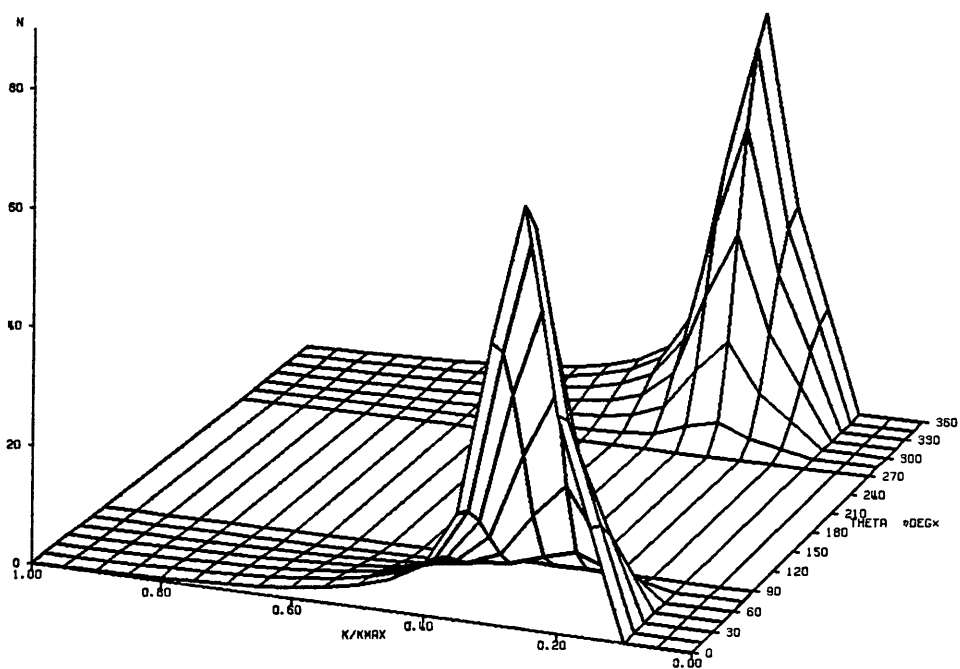


Figure 25. Numerical Prediction for the action  $N$  in the  $(k, \theta)$  space at  $x/L_0 = 0.035$

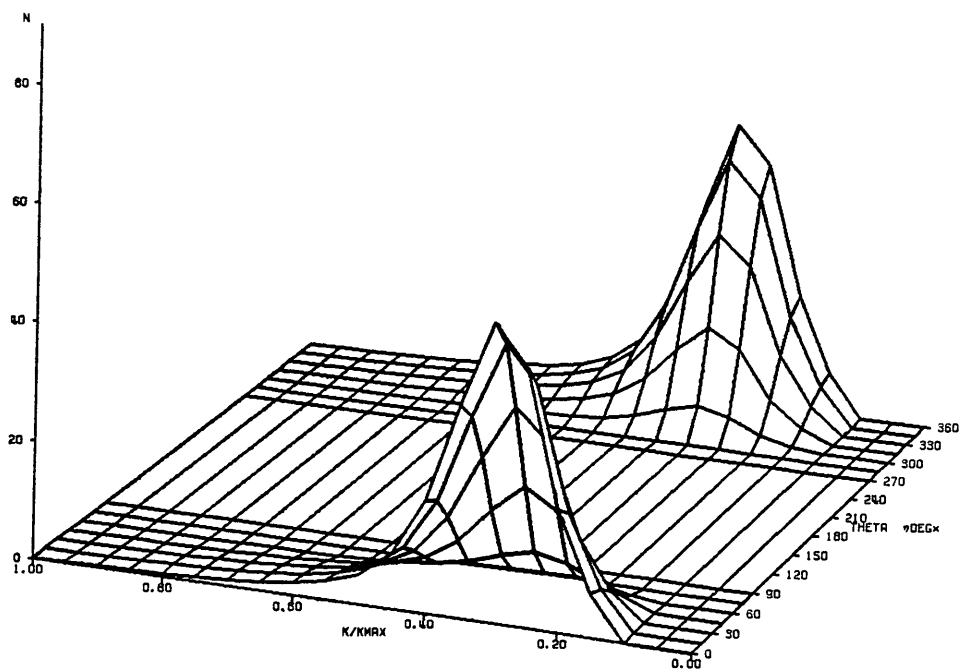


Figure 26. Numerical Prediction for the action  $N$  in the  $(k, \theta)$  space at  $x/L_0 = 0.520$

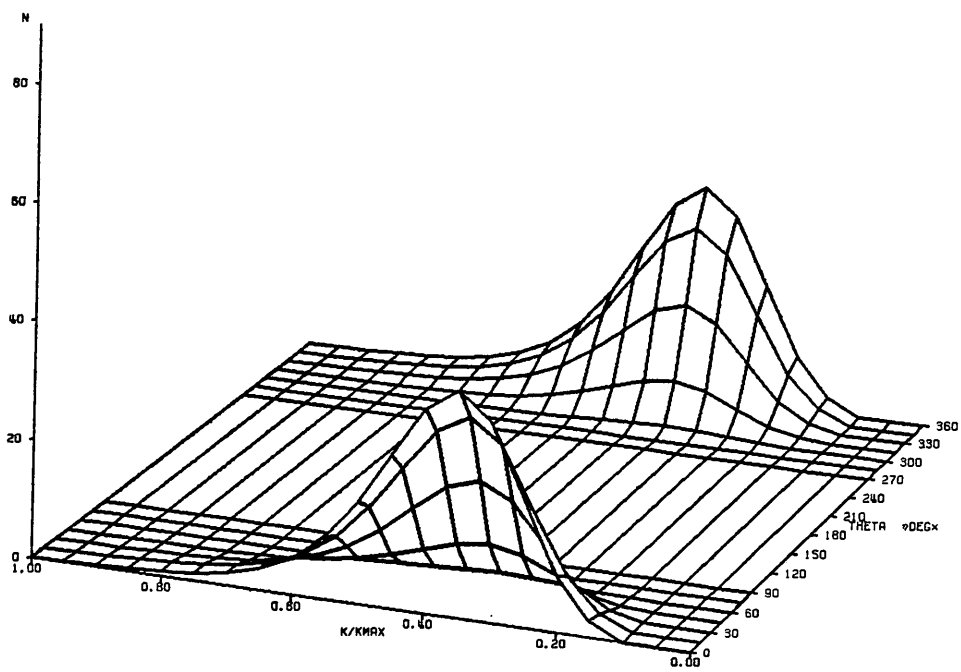


Figure 27. Numerical Prediction for the action  $N$  in the  $(k, \theta)$  space at  $x/L_0 = 0.760$

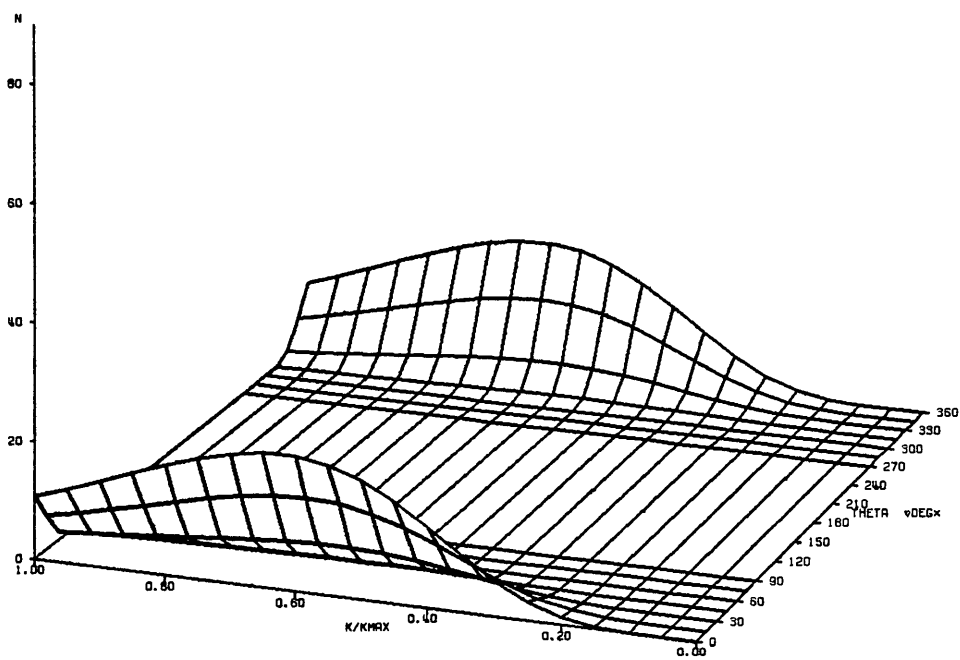
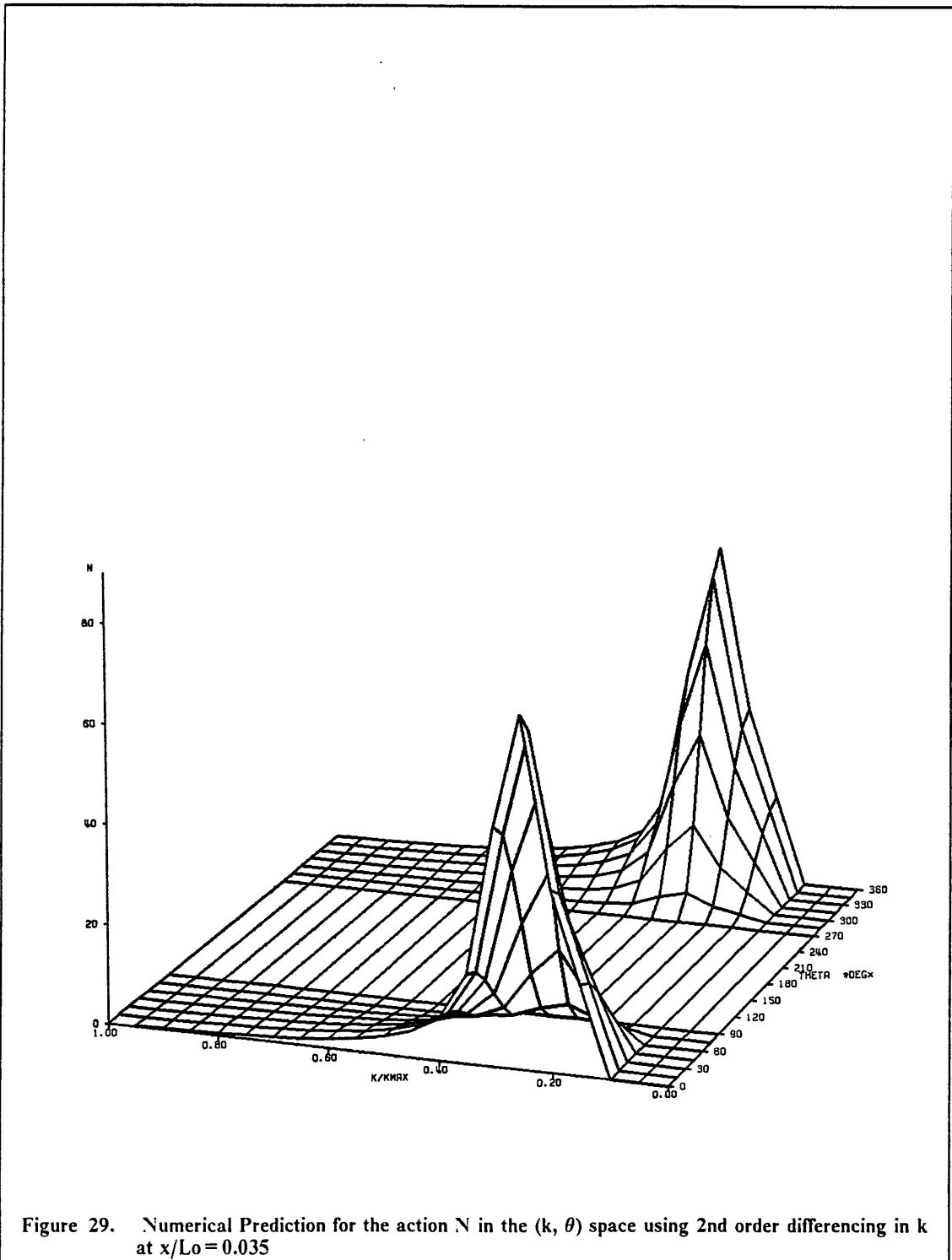


Figure 28. Numerical Prediction for the action  $N$  in the  $(k, \theta)$  space at  $x/L_0 = 1.000$



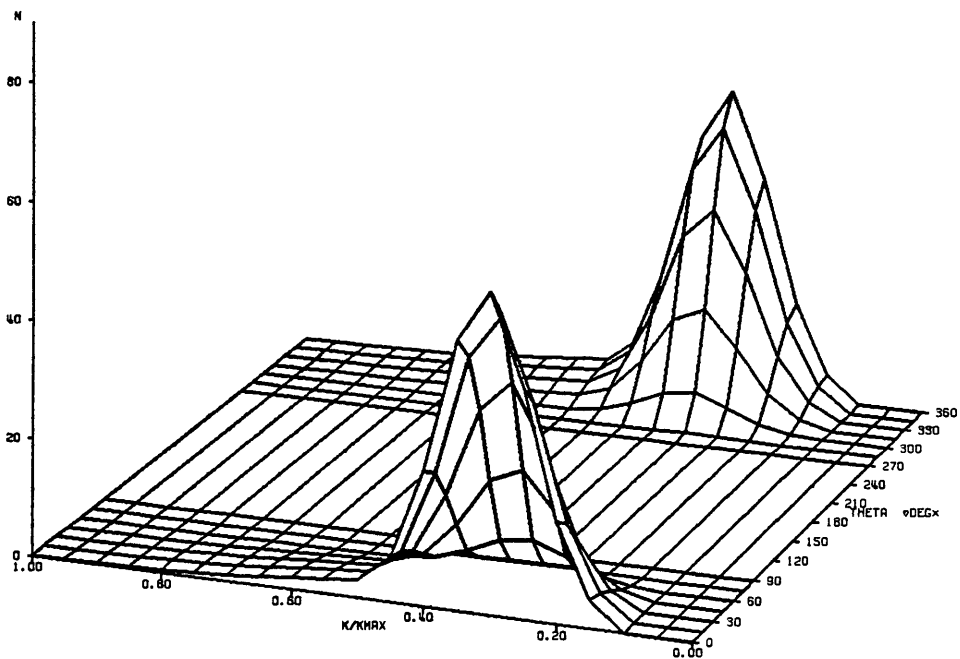
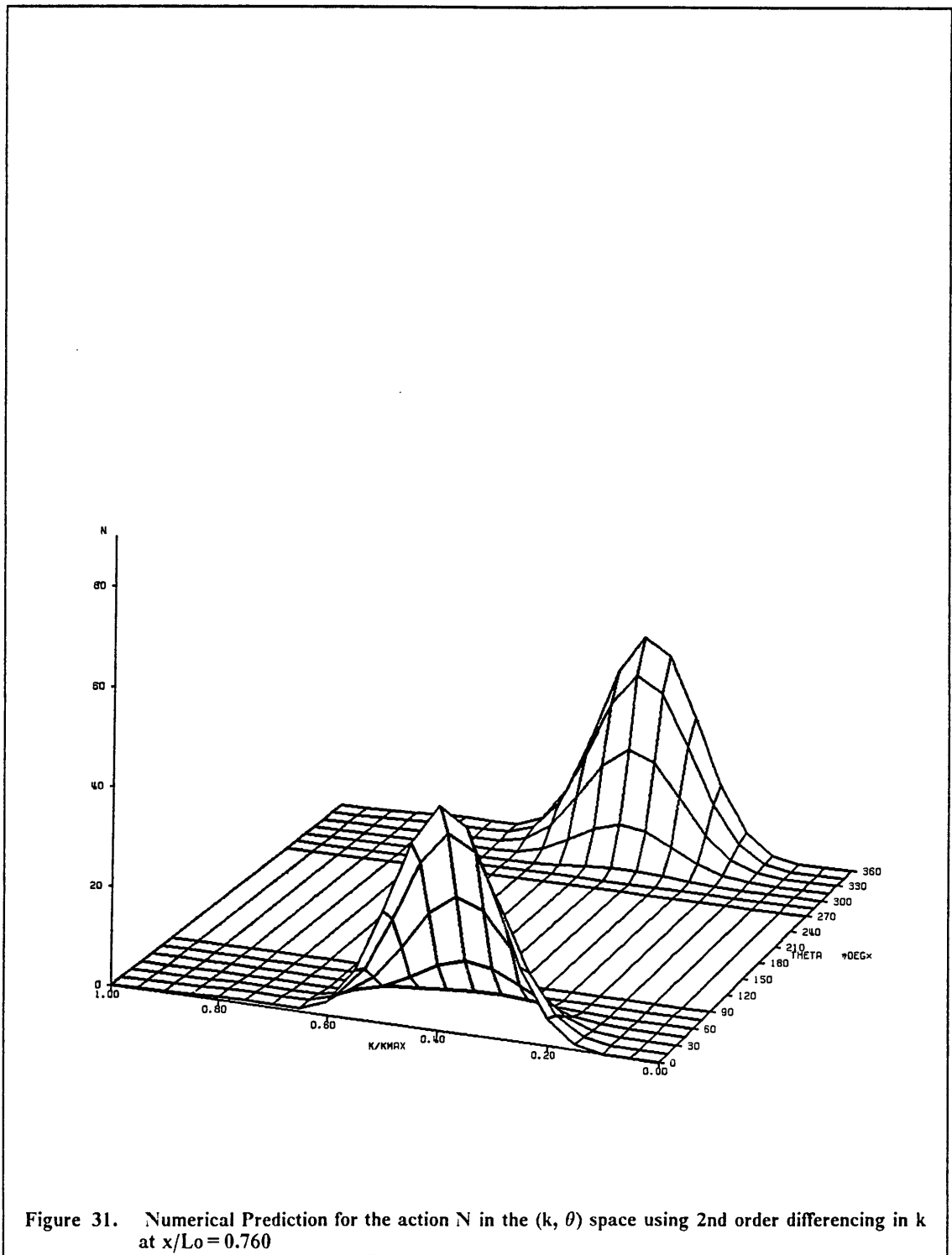


Figure 30. Numerical Prediction for the action  $N$  in the  $(k, \theta)$  space using 2nd order differencing in  $k$  at  $x/L_0 = 0.520$



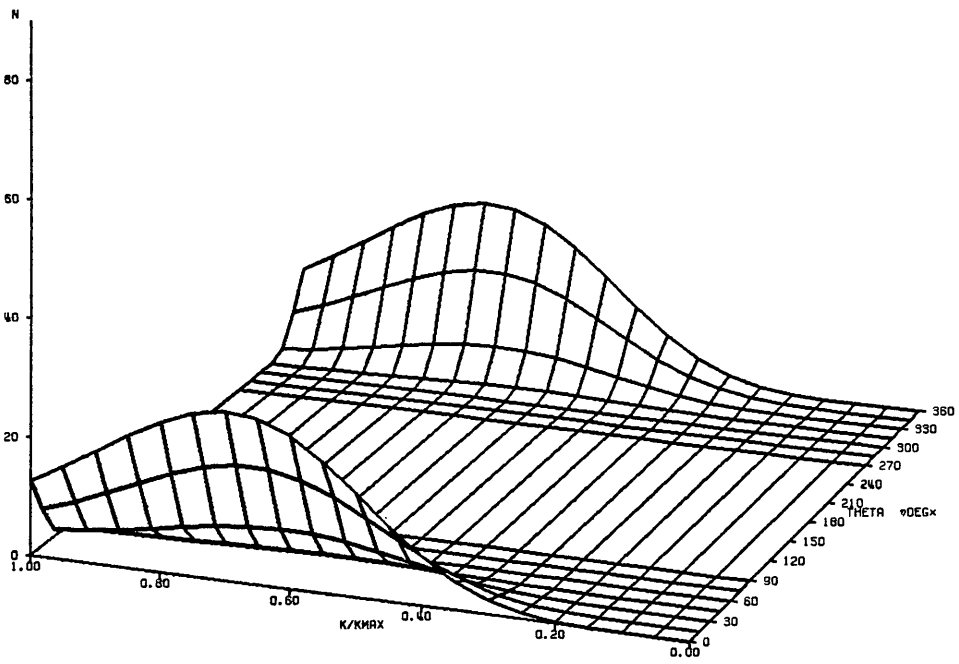


Figure 32. Numerical Prediction for the action  $N$  in the  $(k, \theta)$  space using 2nd order differencing in  $k$  at  $x/L_0 = 1.000$

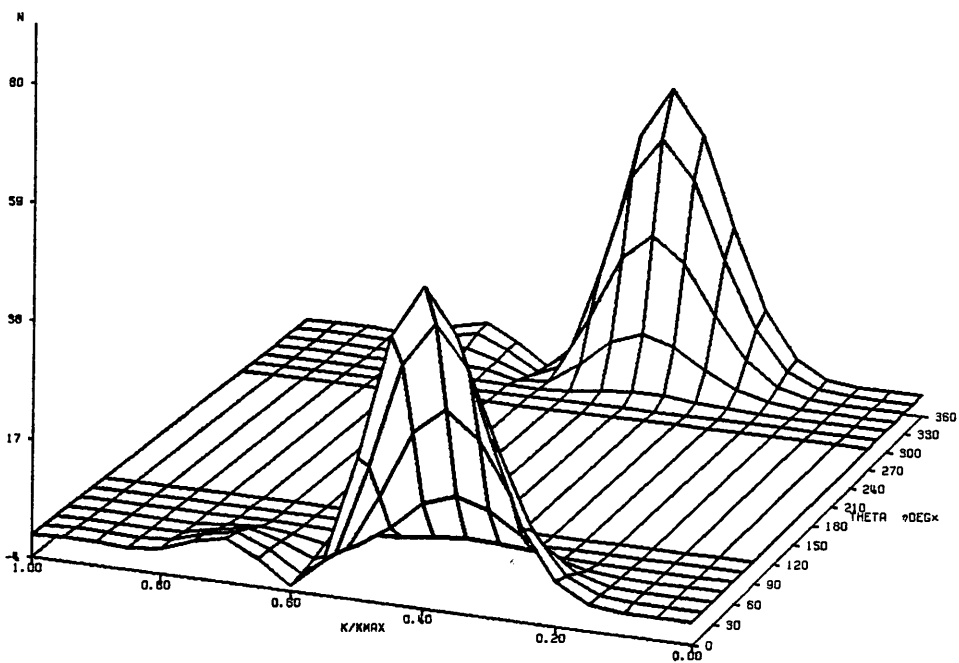


Figure 33. Numerical Prediction for the action  $N$  in the  $(k, \theta)$  space using 3rd order differencing in  $k$  at  $x/L_0 = 0.760$

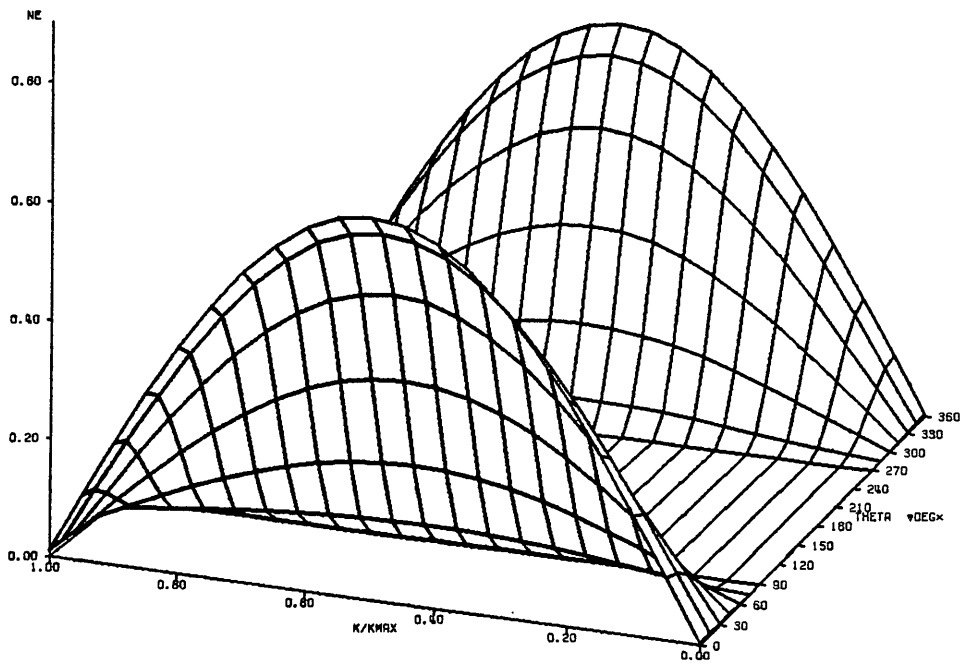
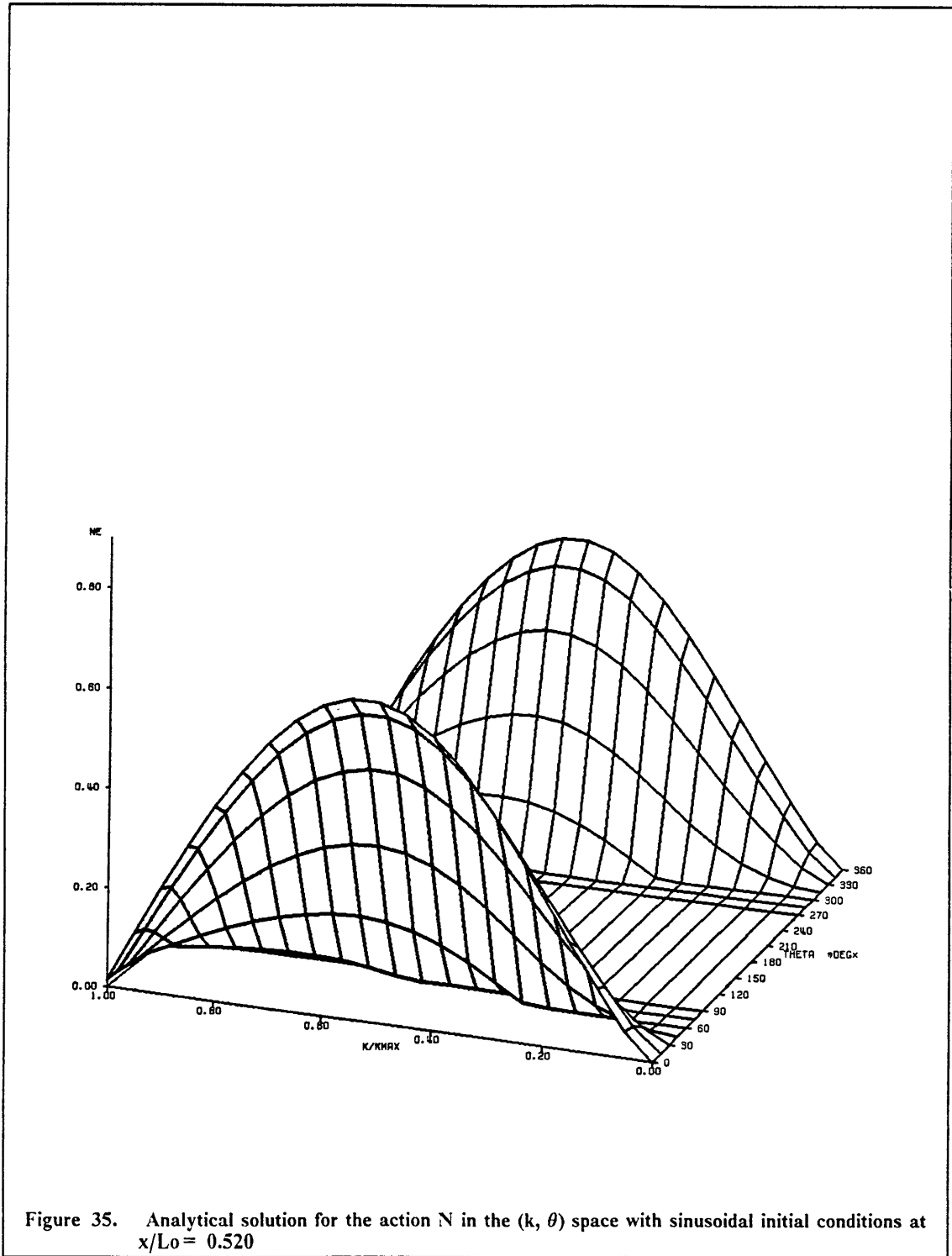


Figure 34. Analytical solution for the action  $N$  in the  $(k, \theta)$  space with sinusoidal initial conditions at  $x/L_0 = 0.035$



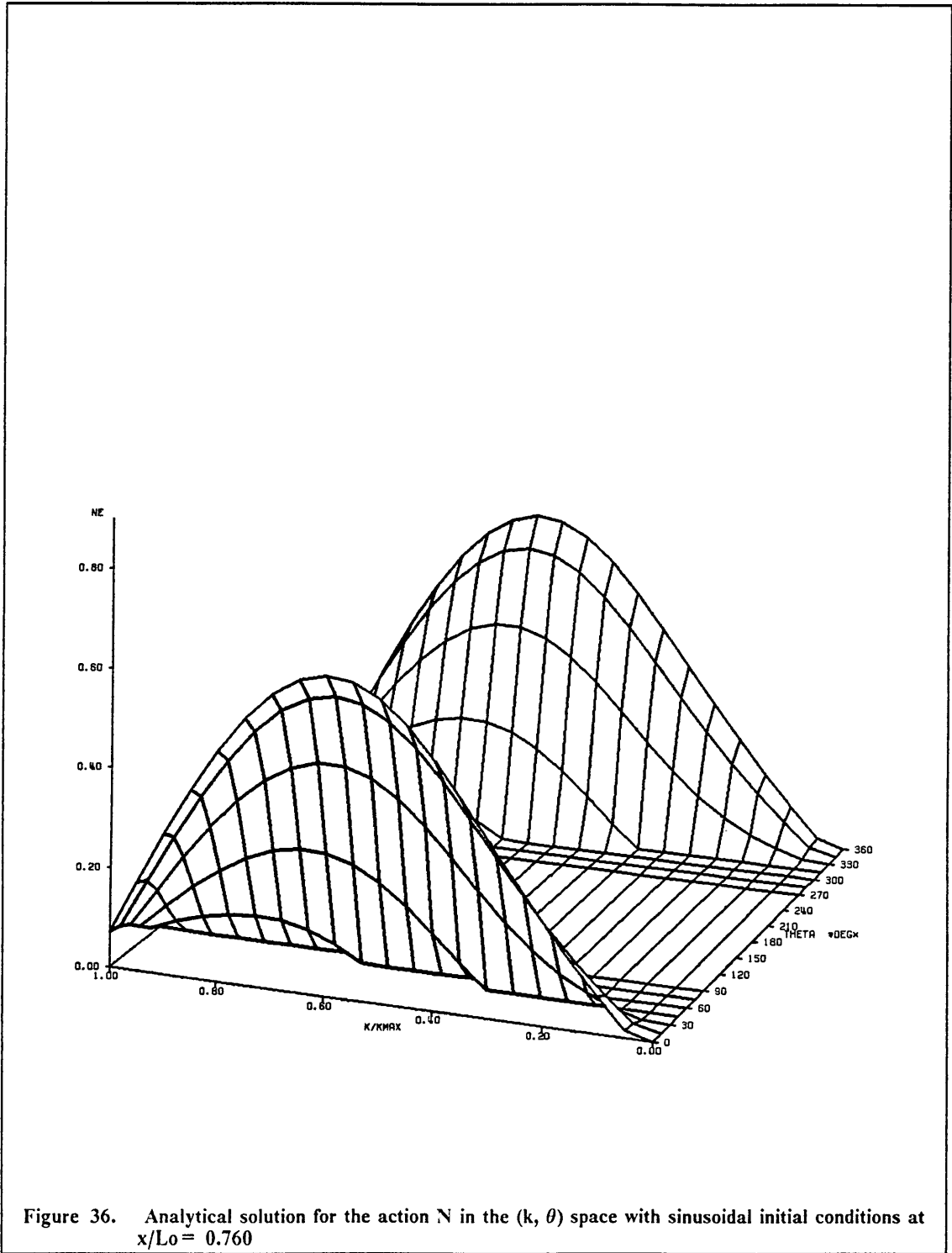


Figure 36. Analytical solution for the action  $N$  in the  $(k, \theta)$  space with sinusoidal initial conditions at  $x/L_0 = 0.760$

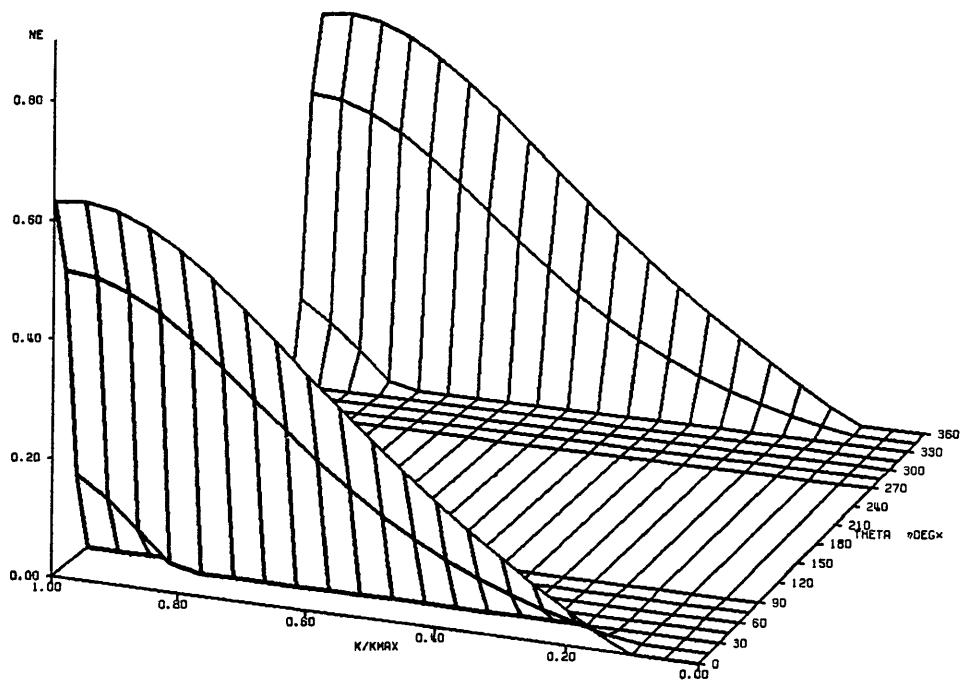


Figure 37. Analytical solution for the action  $N$  in the  $(k, \theta)$  space with sinusoidal initial conditions at  $x/L_0 = 1.000$

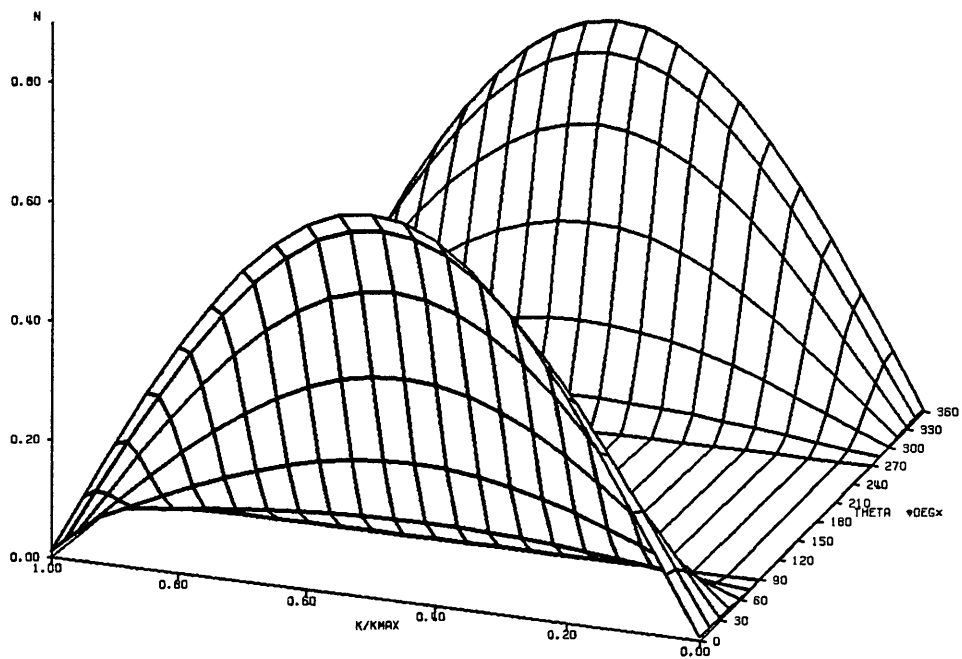
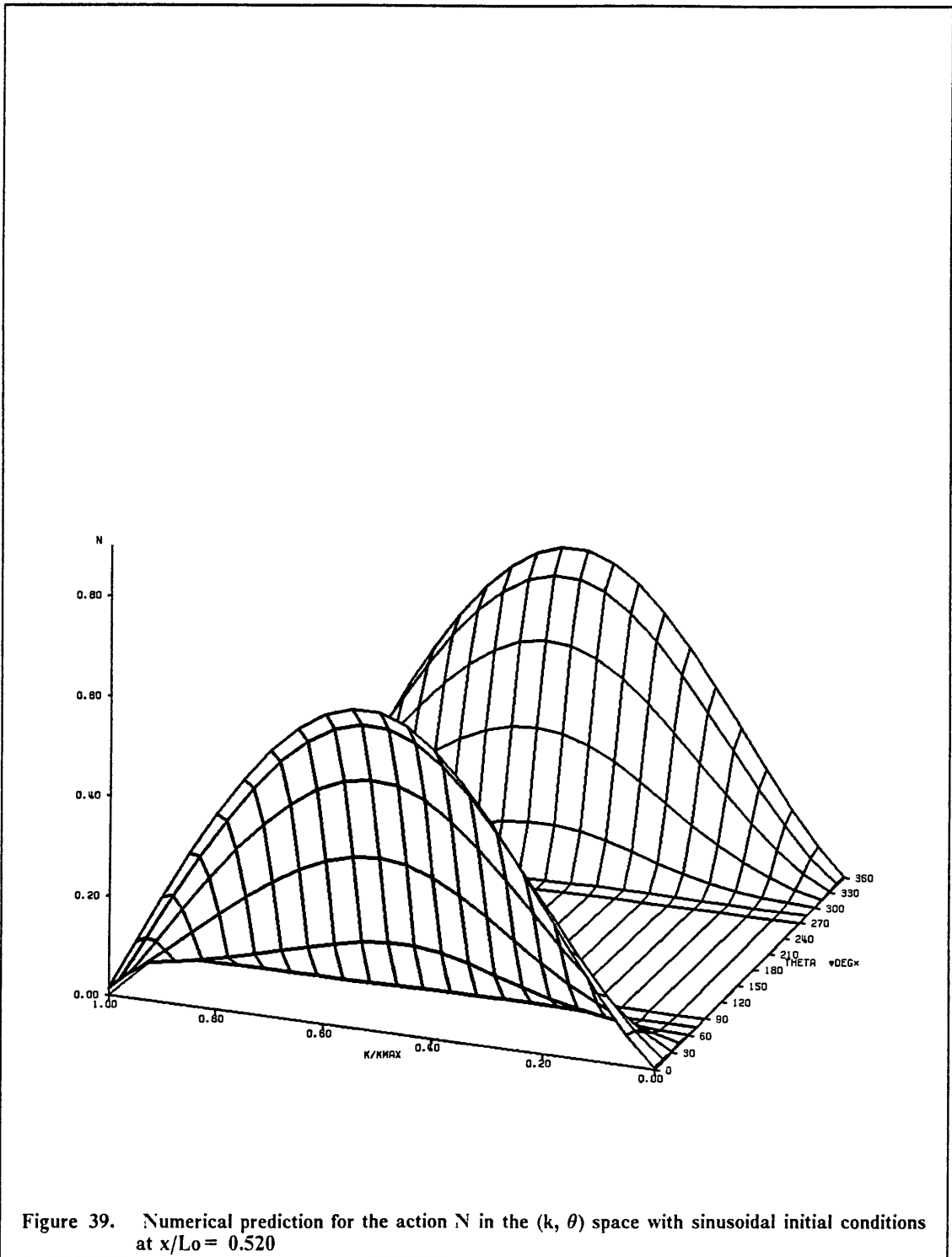
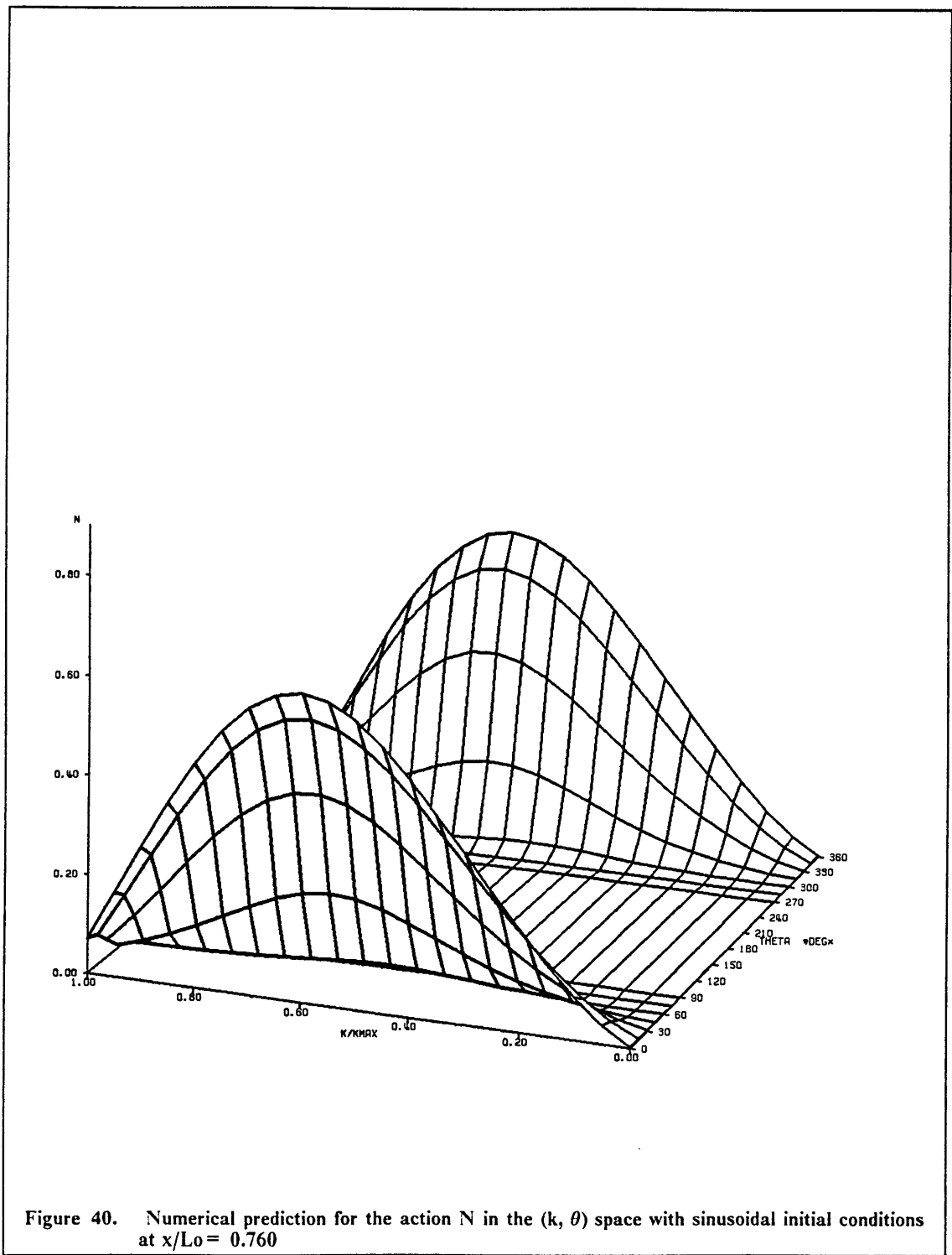


Figure 38. Numerical prediction for the action  $N$  in the  $(k, \theta)$  space with sinusoidal initial conditions at  $x/L_0 = 0.035$





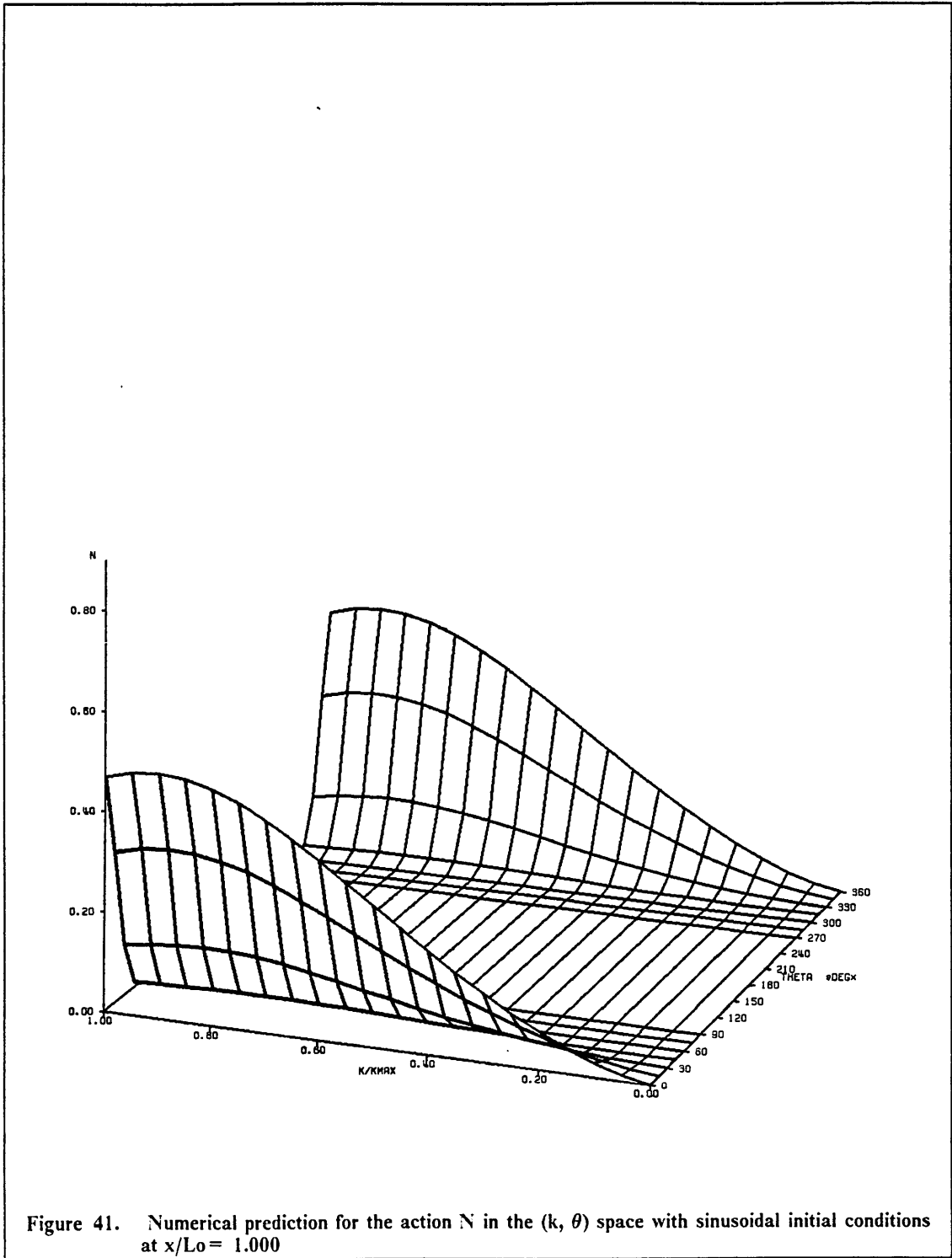


Figure 41. Numerical prediction for the action  $N$  in the  $(k, \theta)$  space with sinusoidal initial conditions at  $x/L_0 = 1.000$

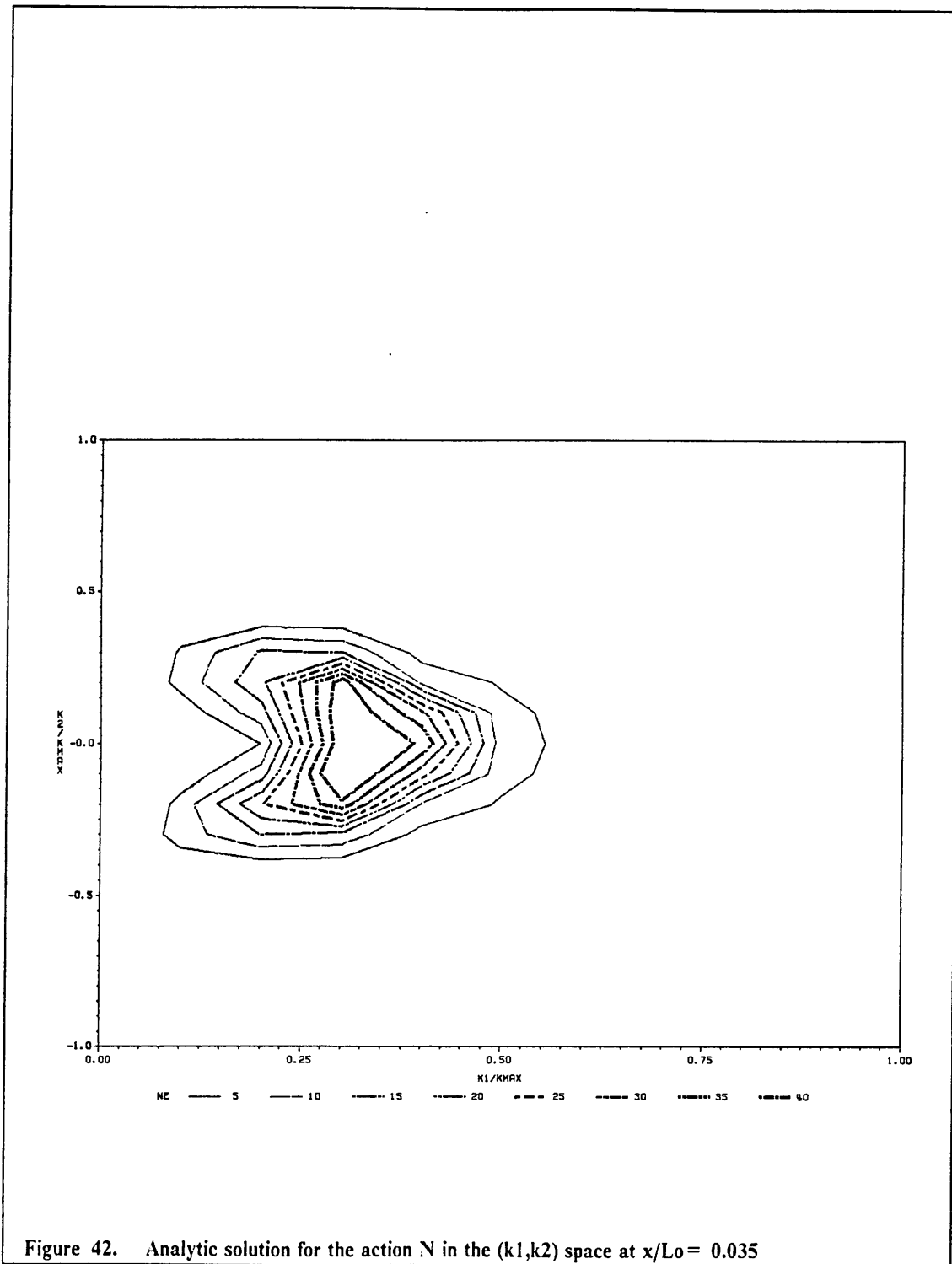


Figure 42. Analytic solution for the action  $N$  in the  $(k_1, k_2)$  space at  $x/L_0 = 0.035$

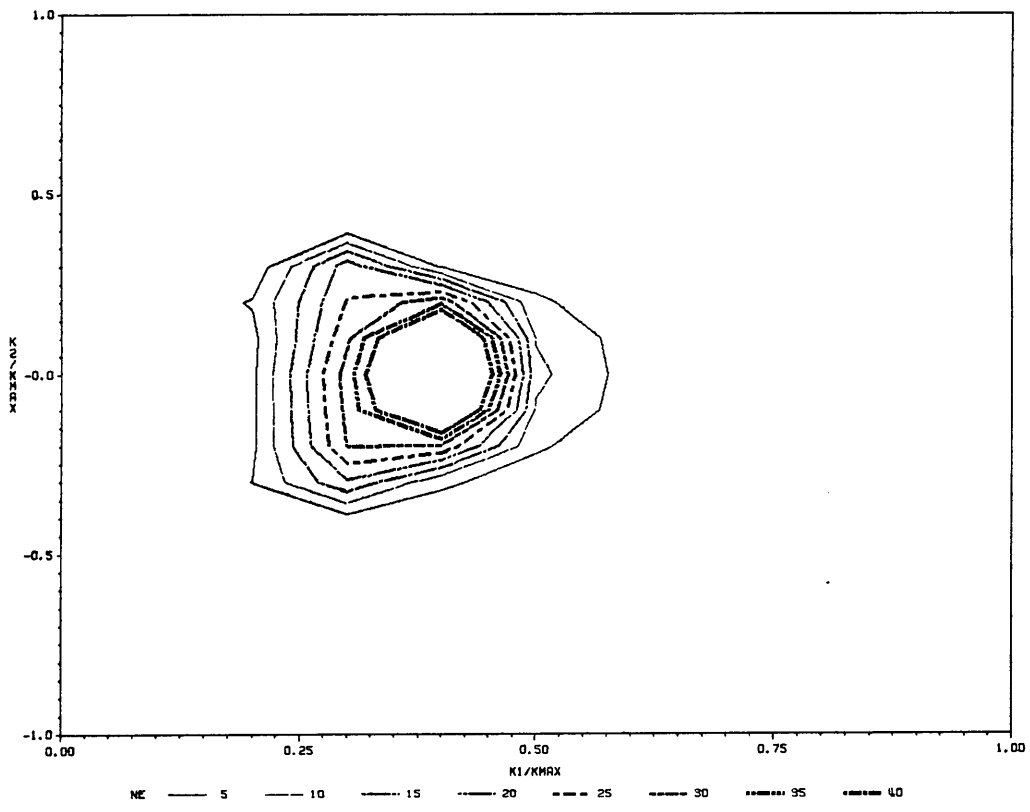


Figure 43. Analytic solution for the action  $N$  in the  $(k_1, k_2)$  space at  $x/L_0 = 0.520$

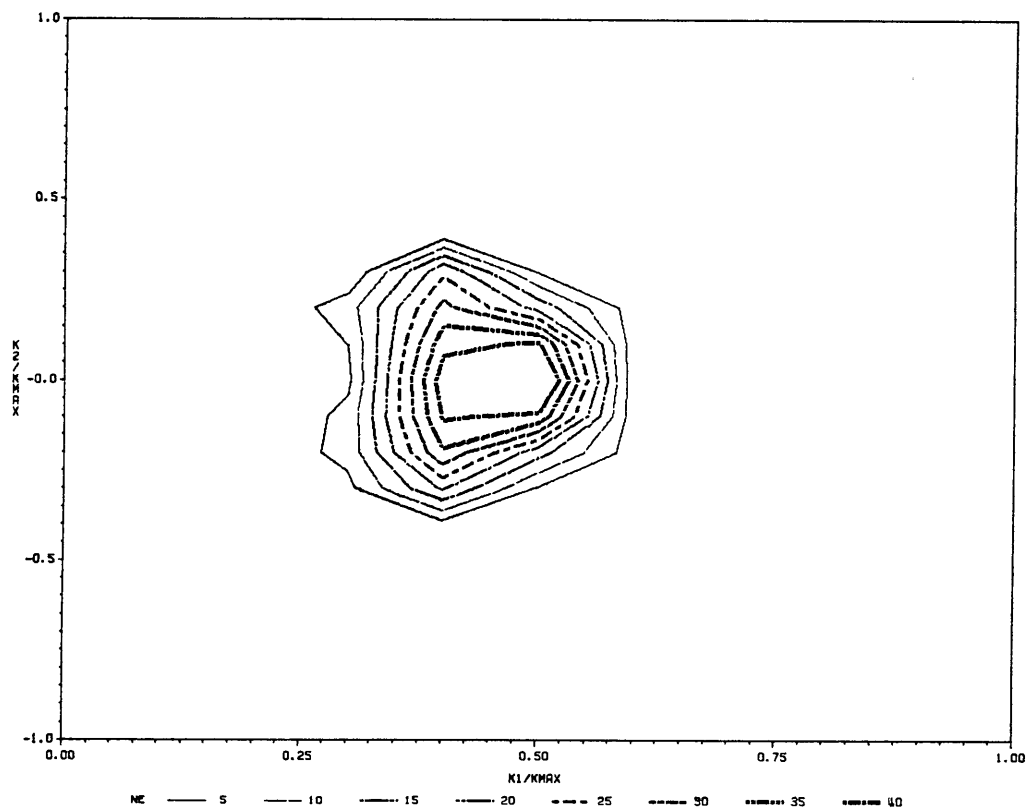


Figure 44. Analytic solution for the action  $N$  in the  $(k_1, k_2)$  space at  $x/L_0 = 0.760$

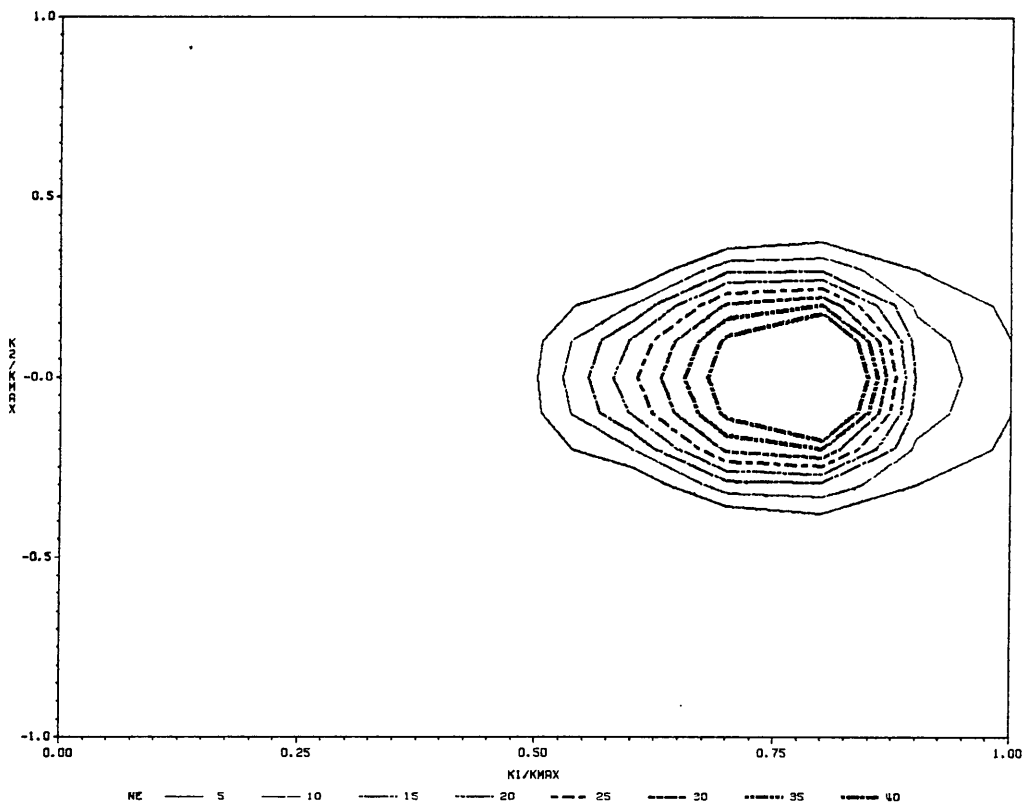


Figure 45. Analytic solution for the action  $N$  in the  $(k_1, k_2)$  space at  $x/L_0 = 1.000$

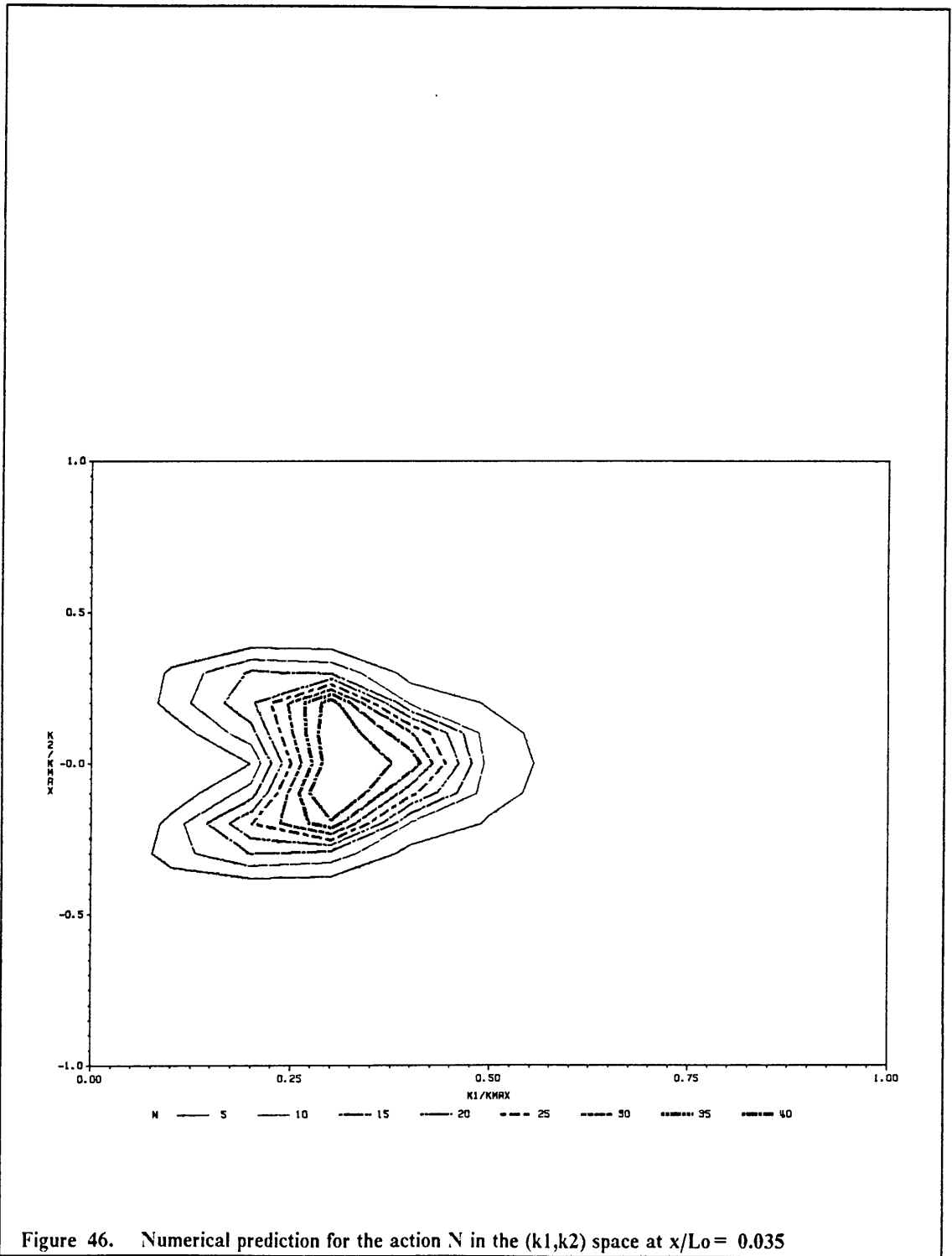
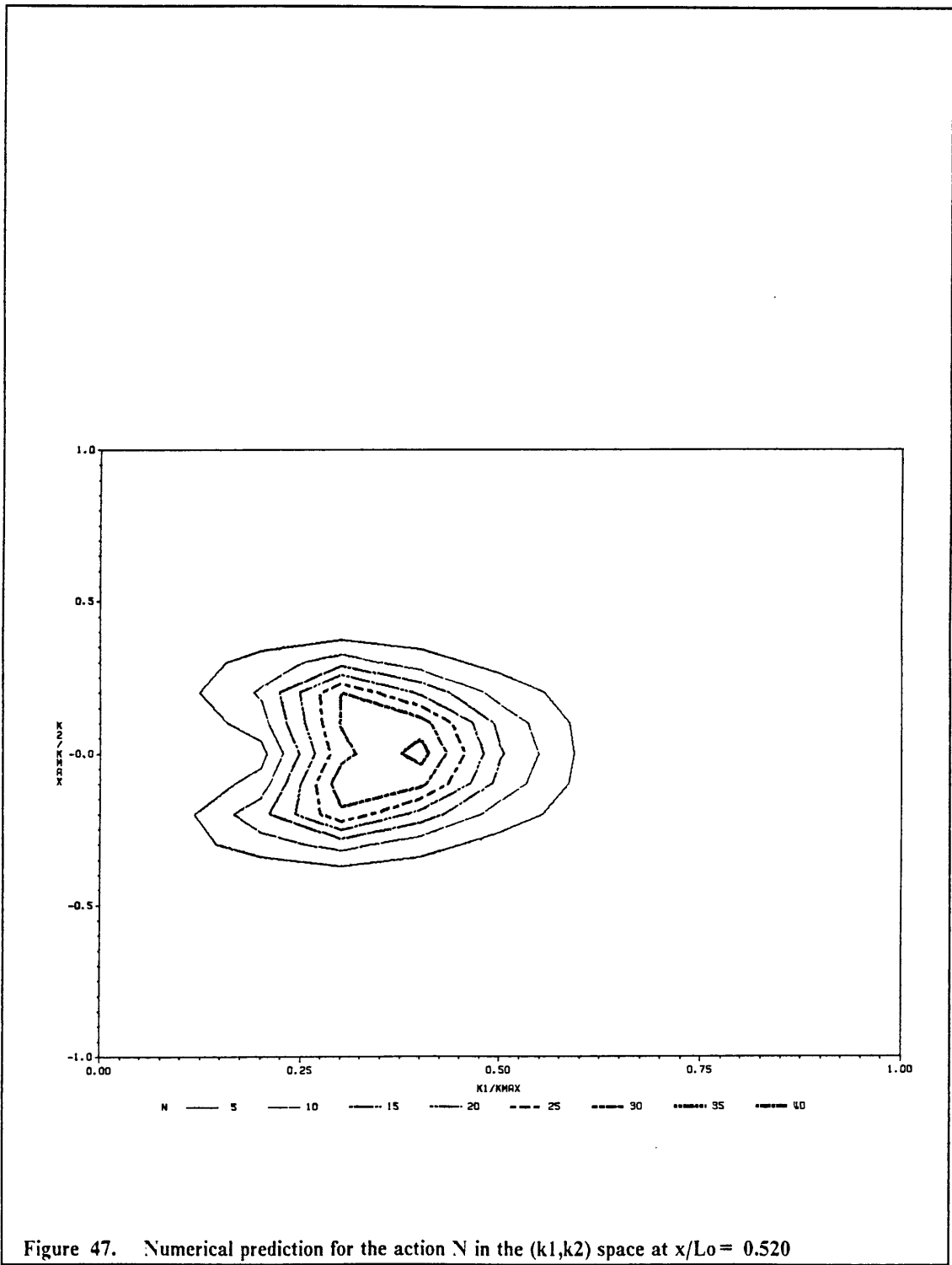


Figure 46. Numerical prediction for the action  $N$  in the  $(k_1, k_2)$  space at  $x/L_0 = 0.035$



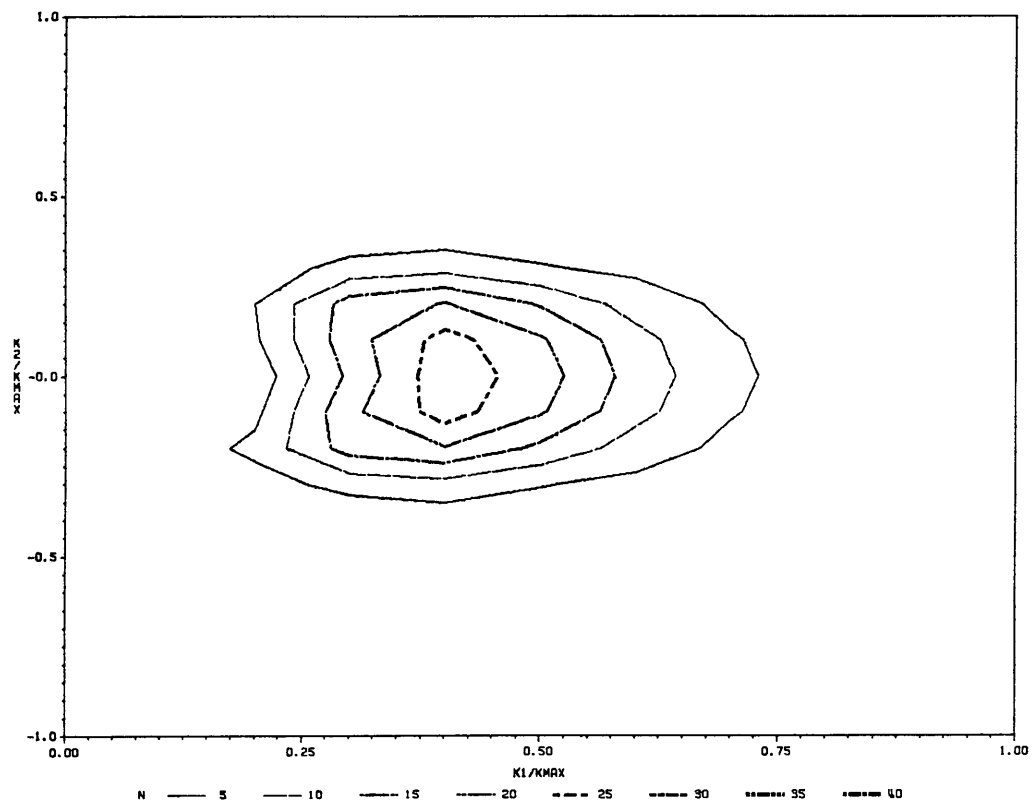


Figure 48. Numerical prediction for the action  $N$  in the  $(k_1, k_2)$  space at  $x/L_0 = 0.760$

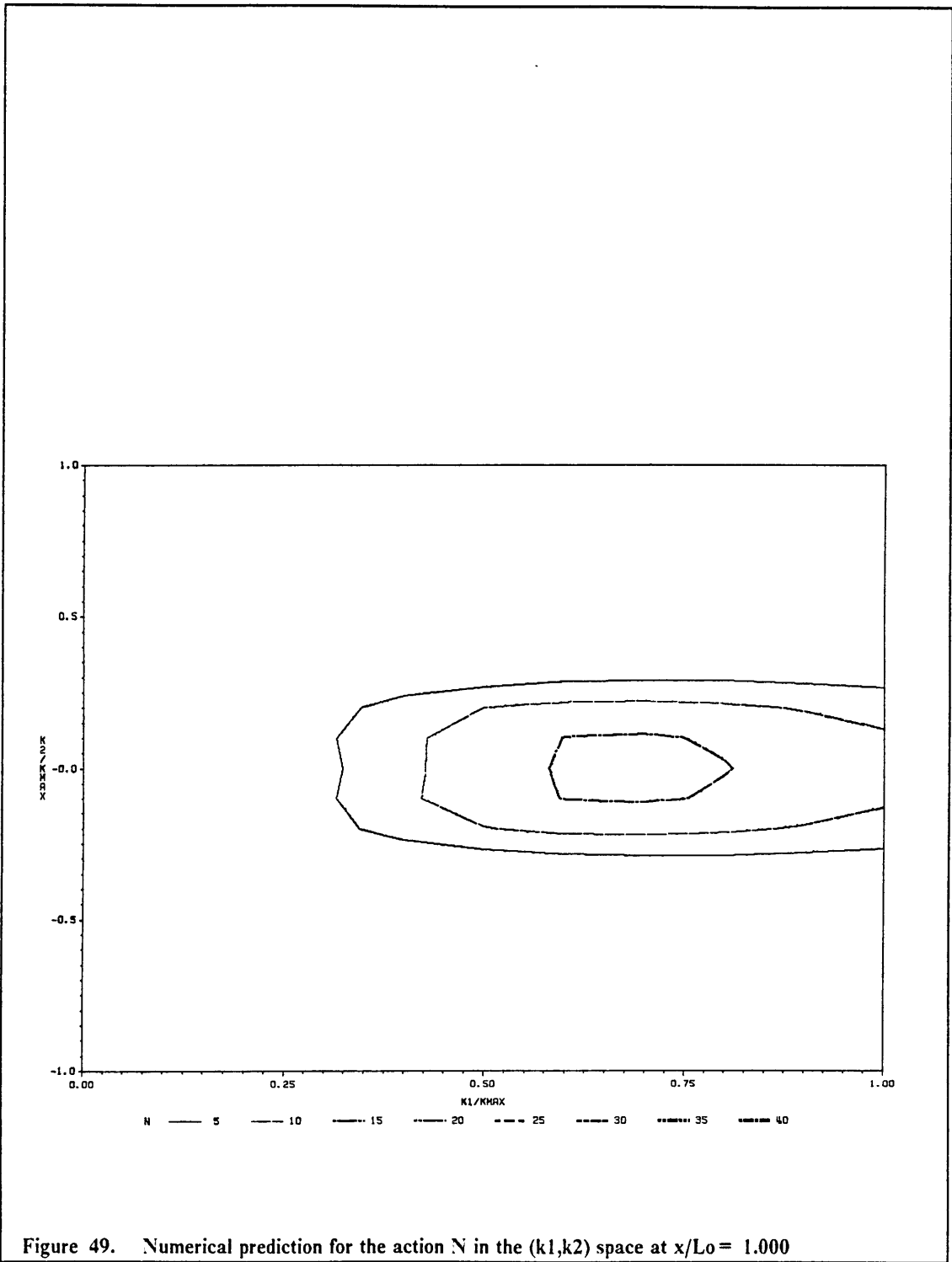


Figure 49. Numerical prediction for the action  $N$  in the  $(k_1, k_2)$  space at  $x/L_0 = 1.000$

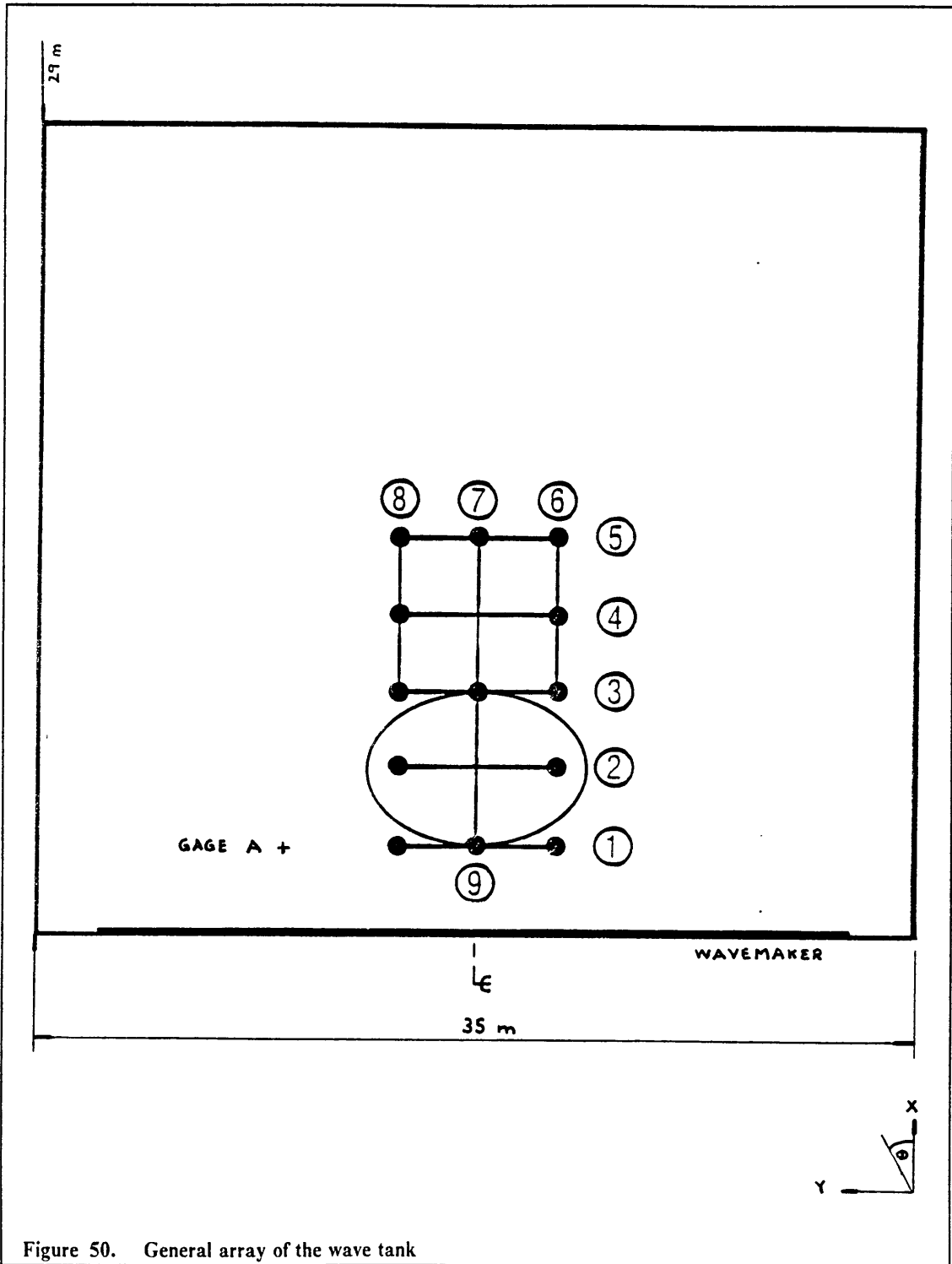
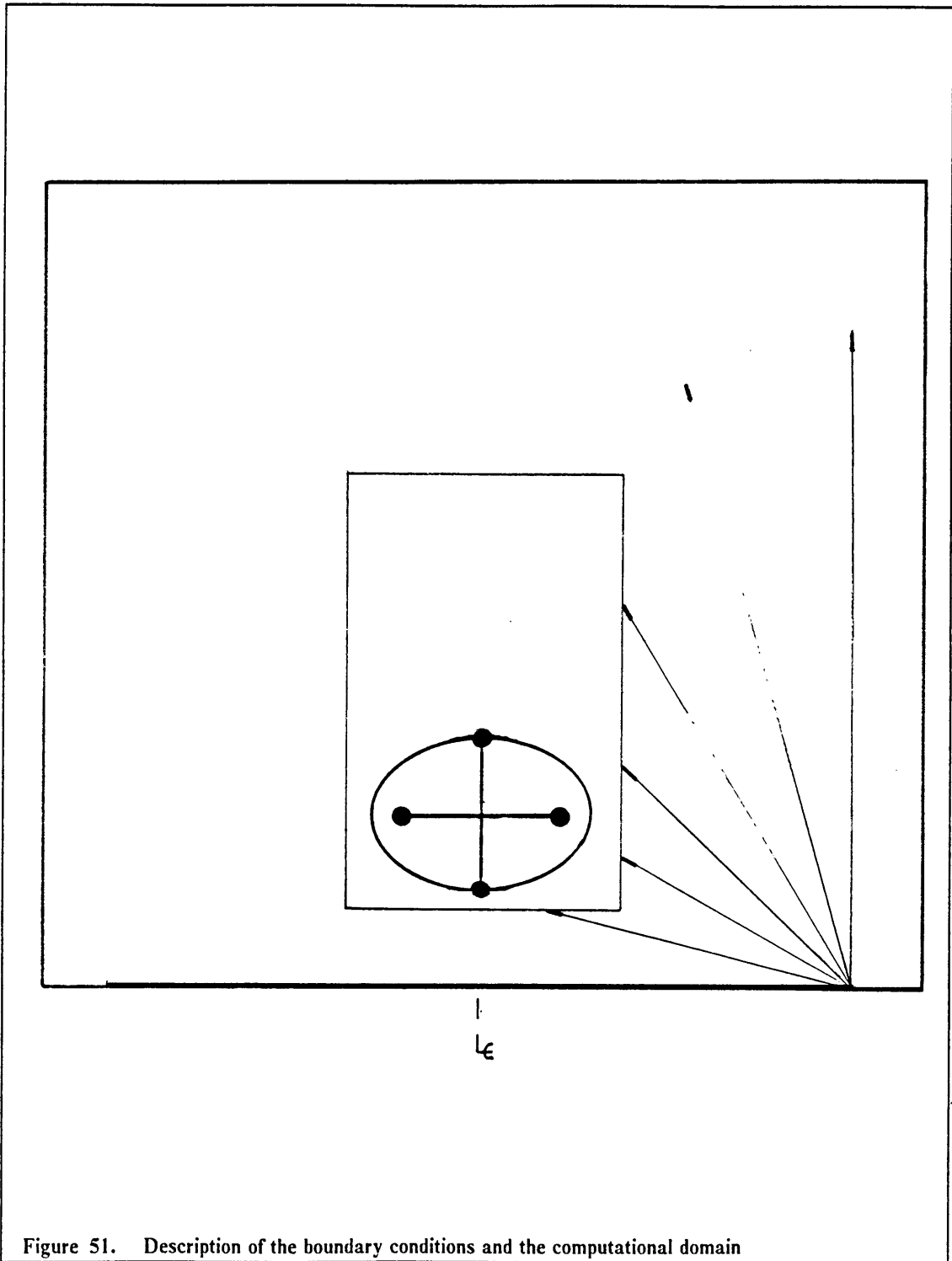


Figure 50. General array of the wave tank



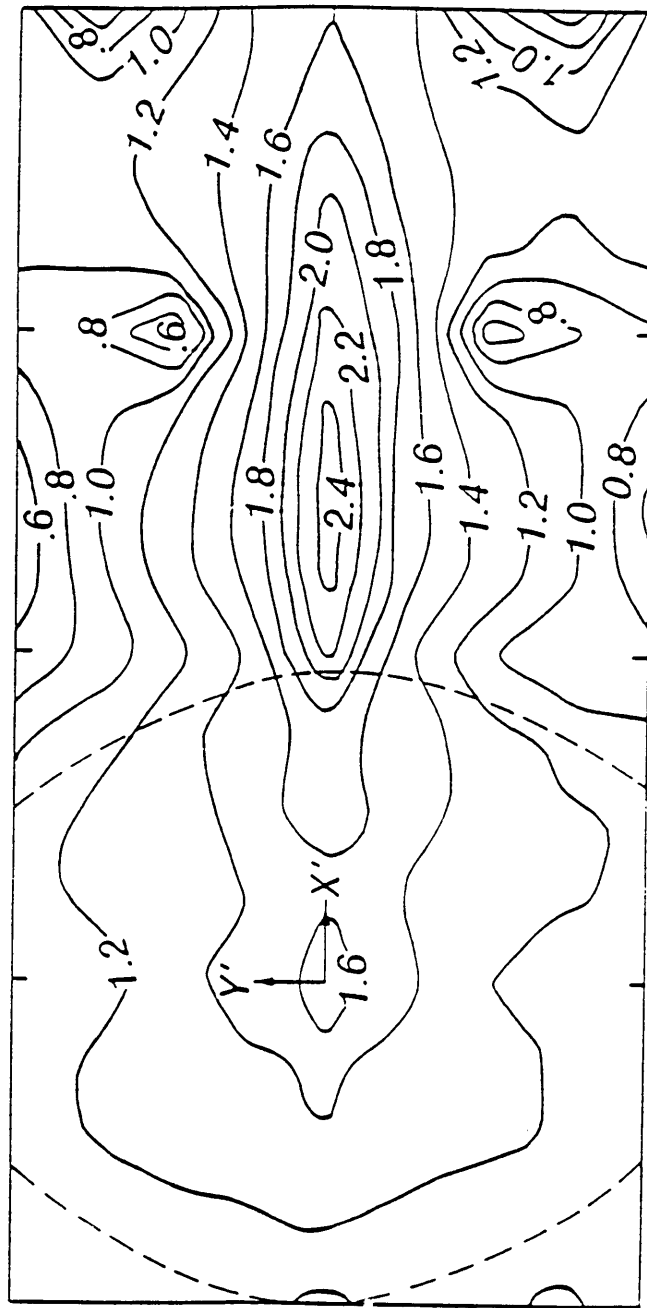


Figure 52. Wave height levels as given by paper for the monochrome case with  $\sigma = 4.83$  Hz and  $\lambda = 0$

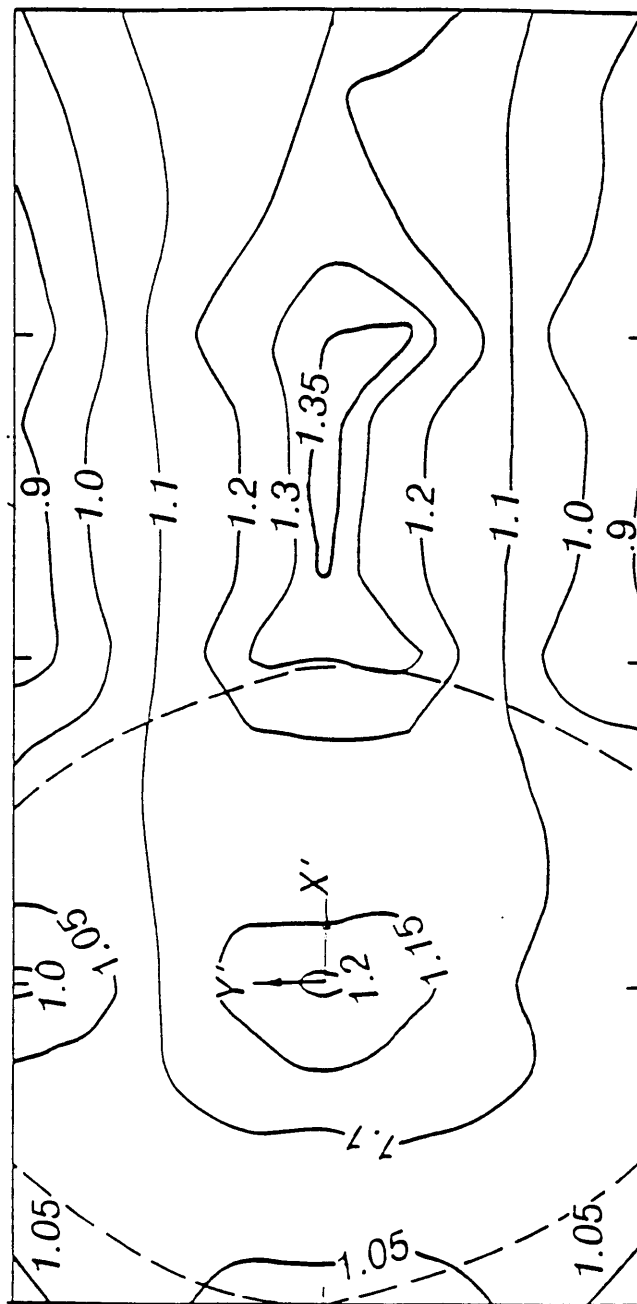


Figure 53. Wave height levels as given by paper for the spectral case with  $\gamma = 2$  and  $\lambda = 10$

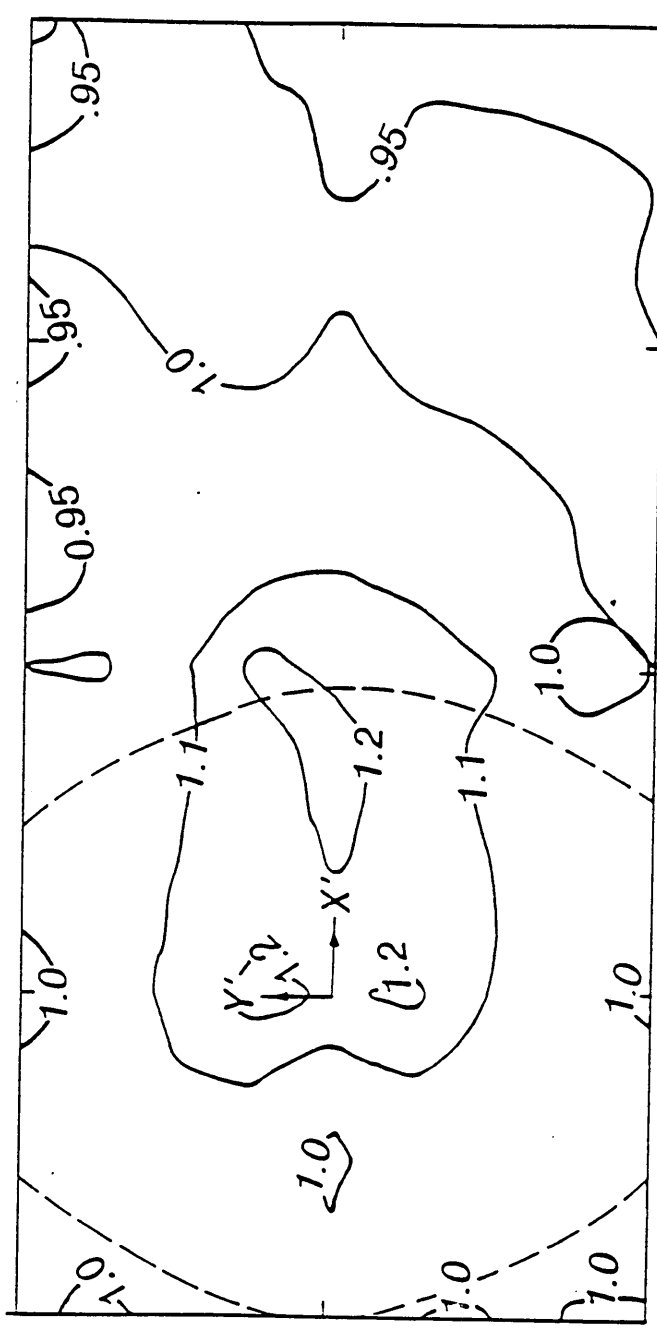
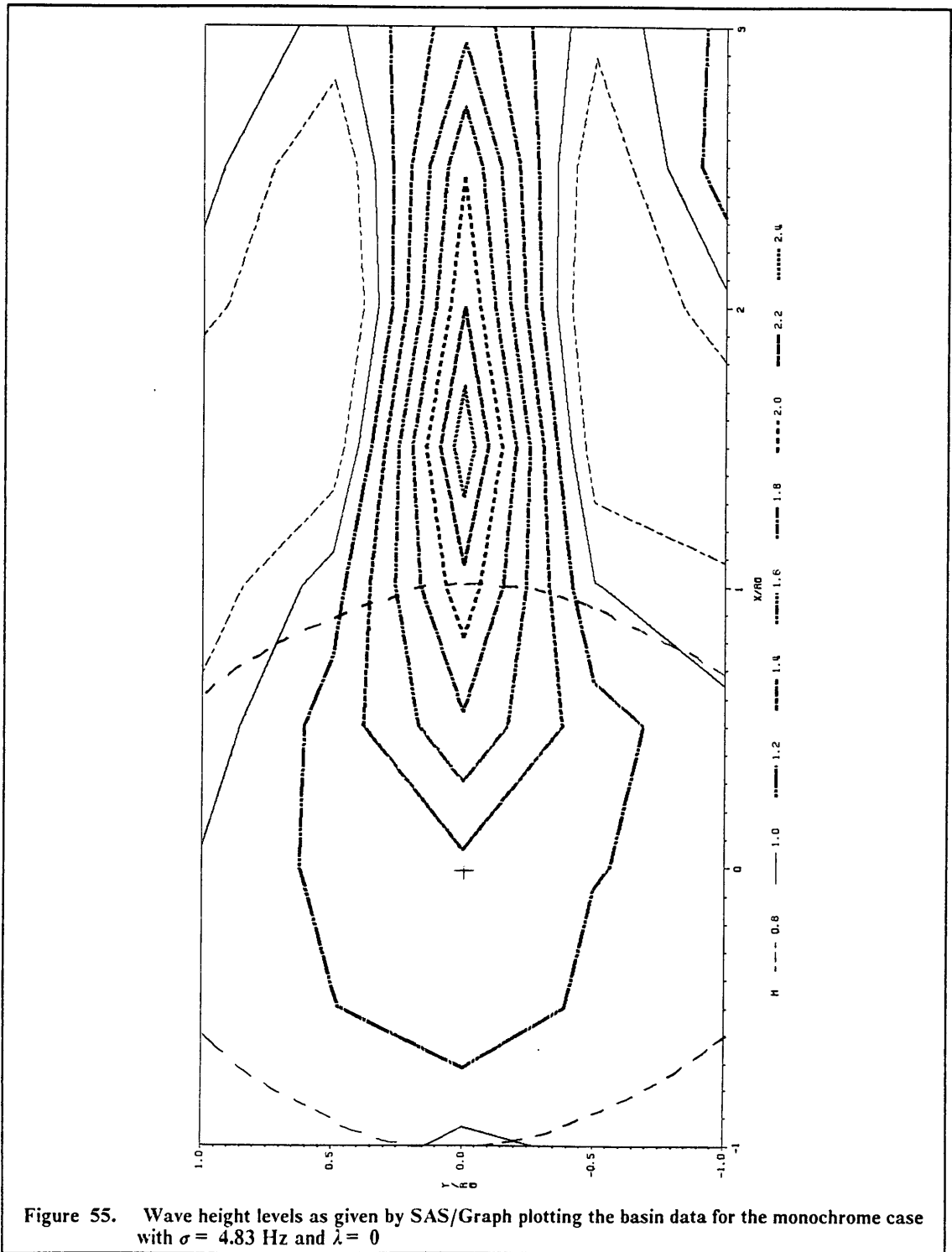


Figure 54. Wave height levels as given by paper for the spectral case with  $\gamma = 2$  and  $\lambda = 30$



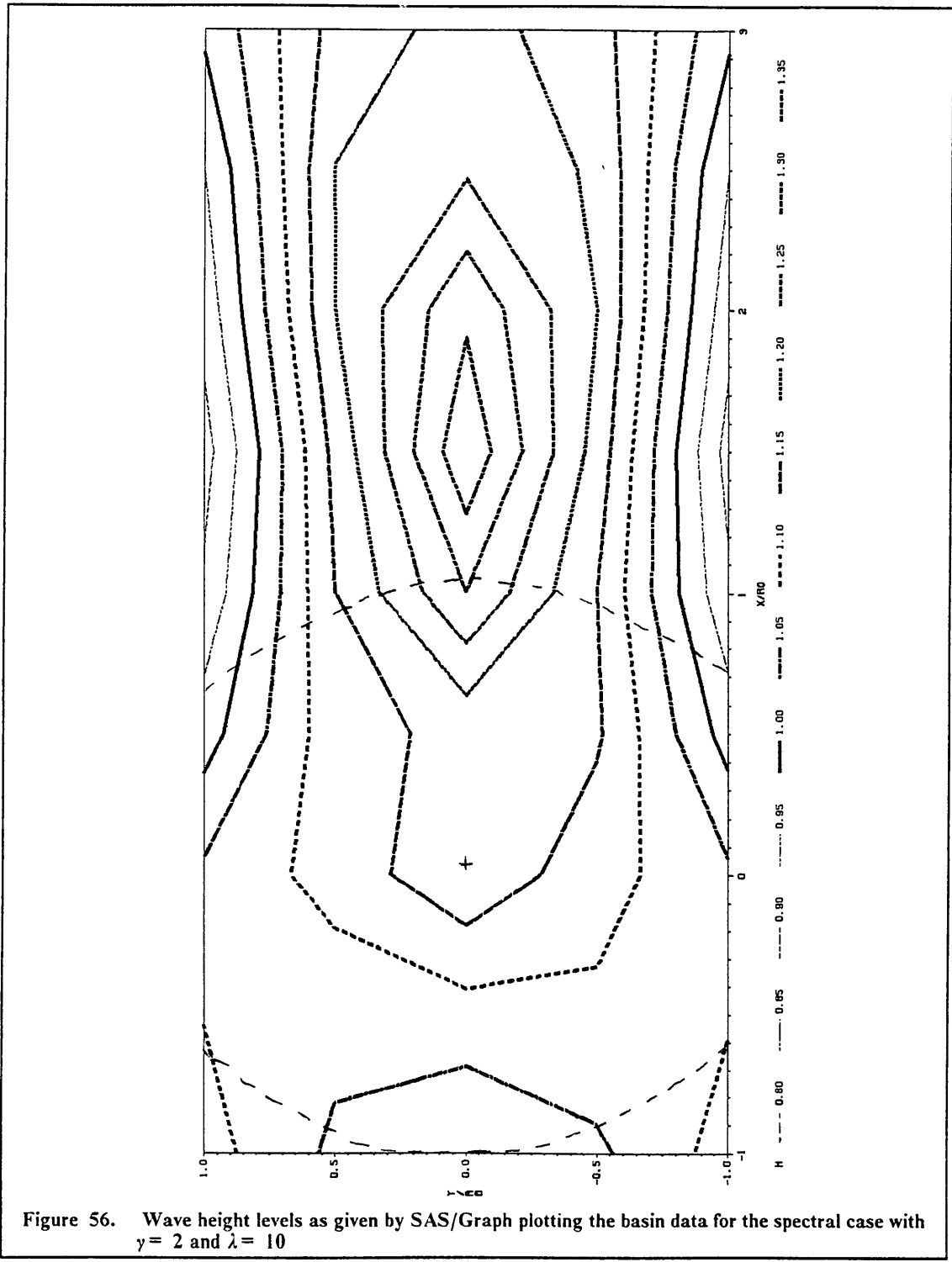
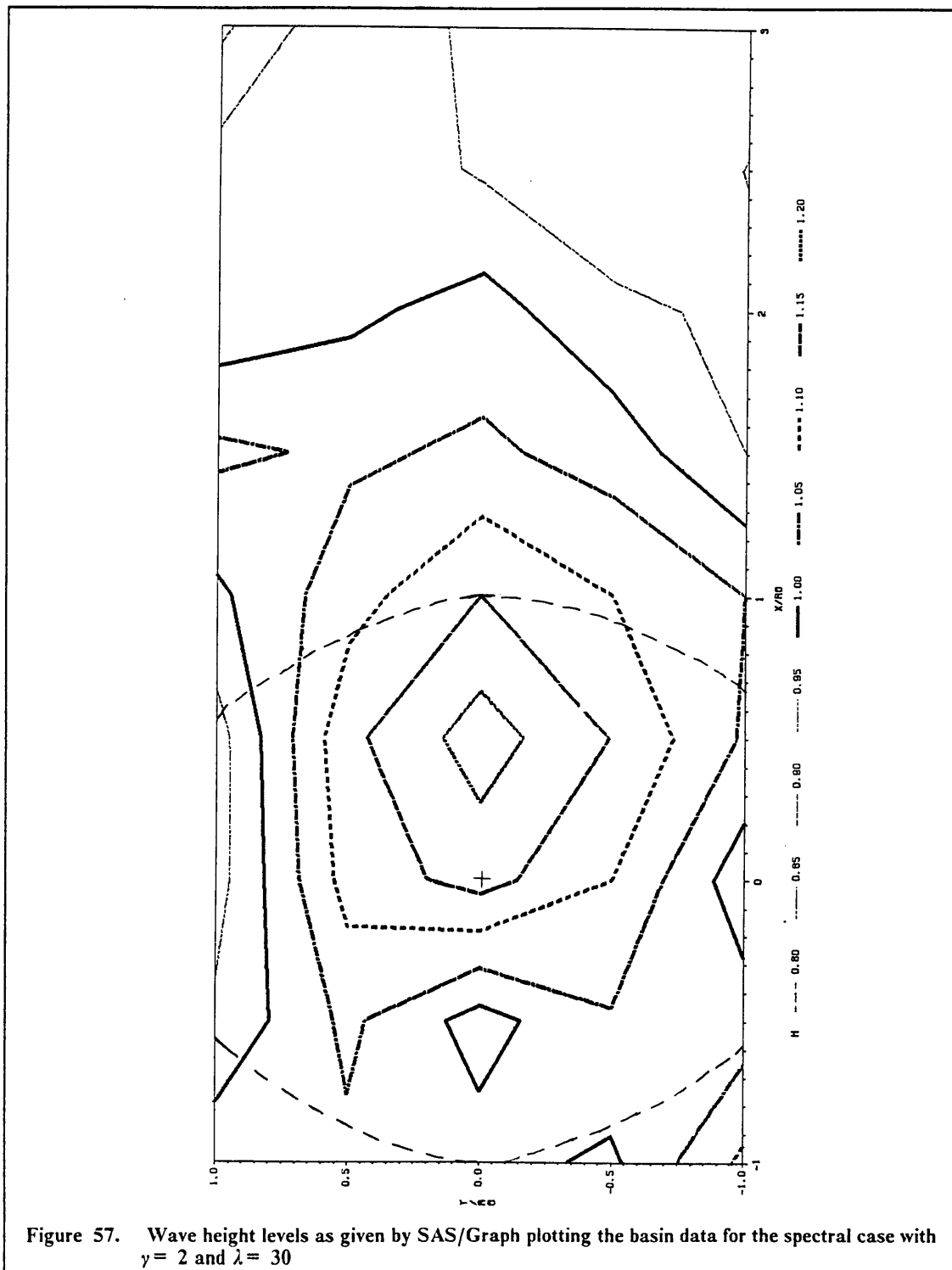
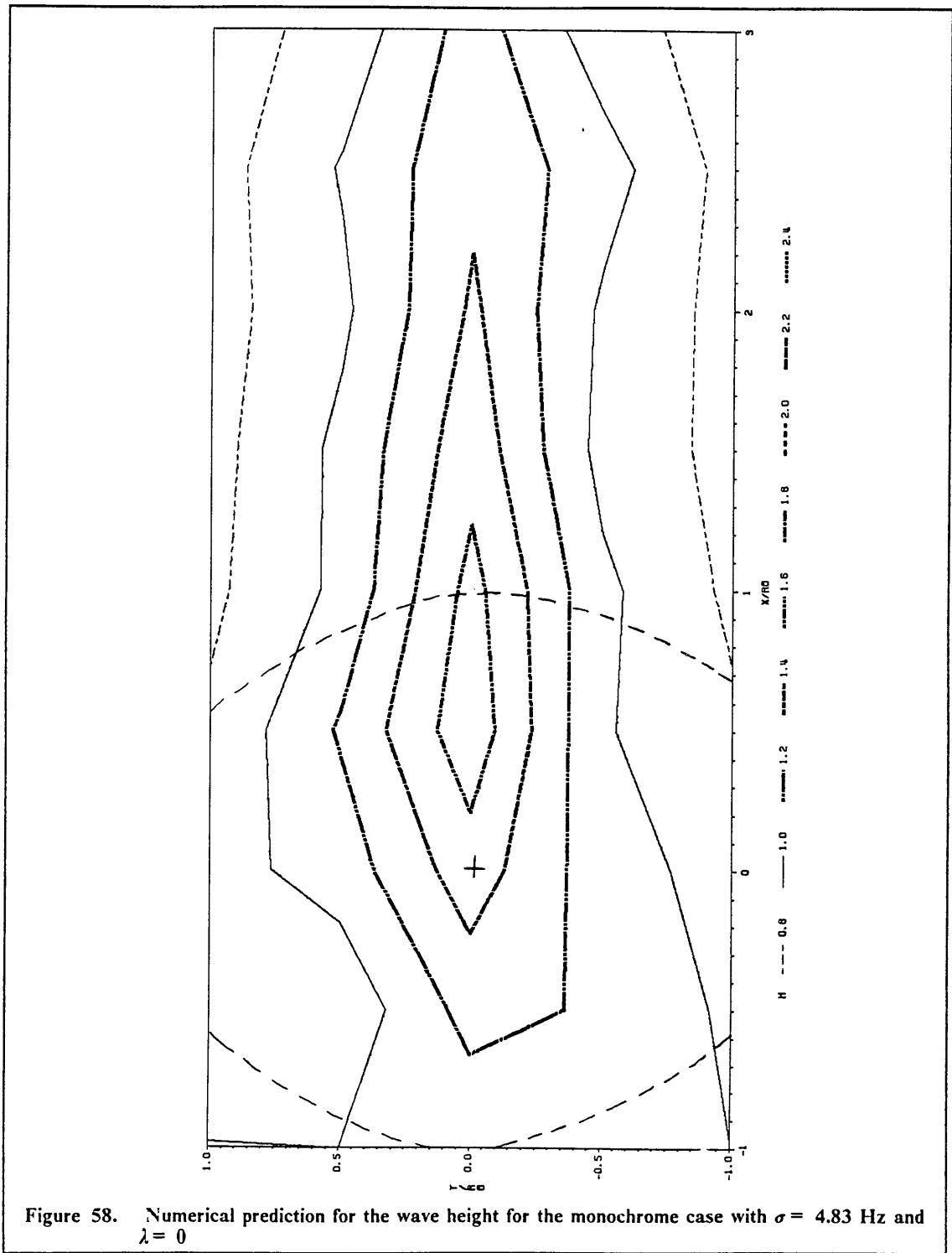


Figure 56. Wave height levels as given by SAS/Graph plotting the basin data for the spectral case with  $\gamma = 2$  and  $\lambda = 10$





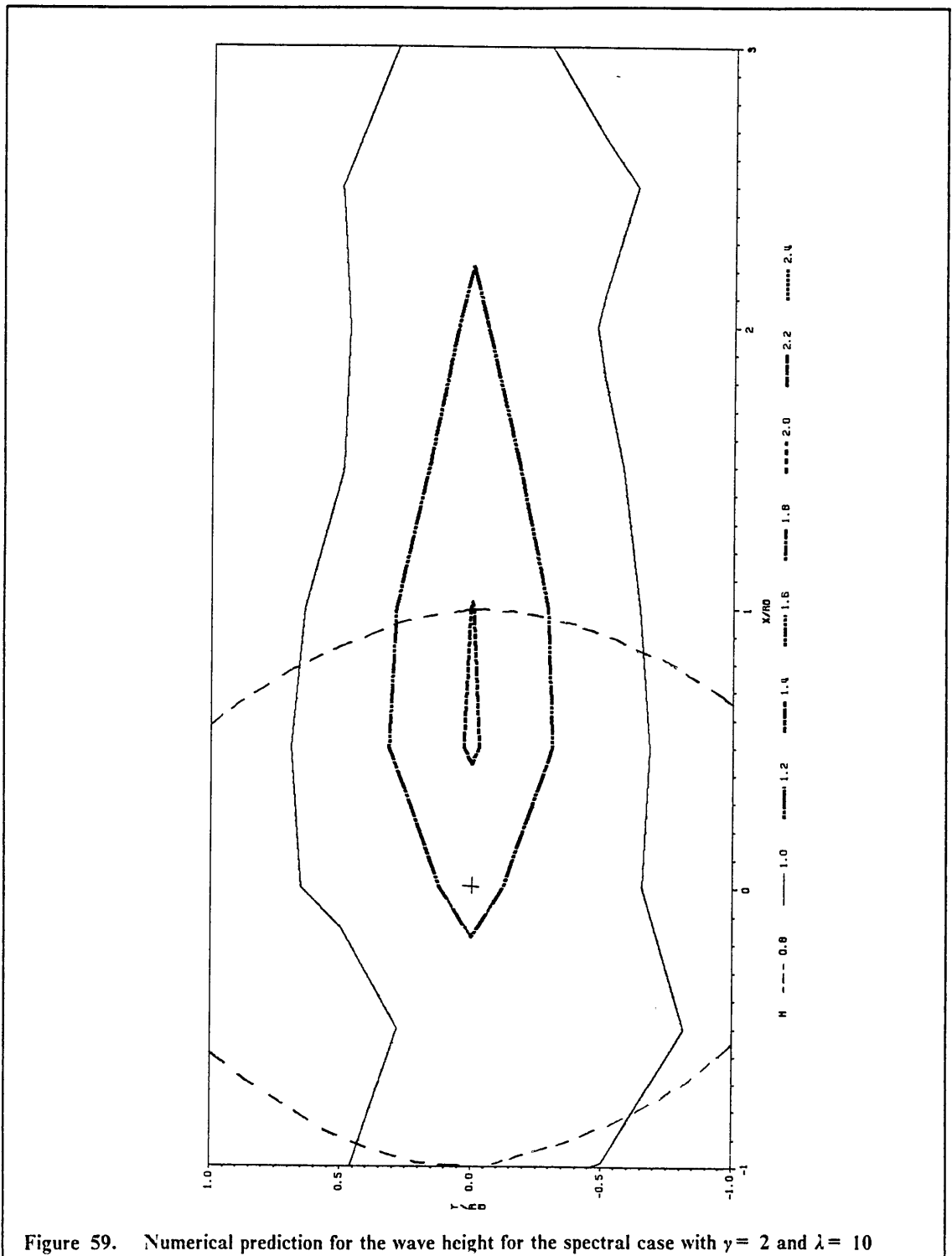


Figure 59. Numerical prediction for the wave height for the spectral case with  $\gamma = 2$  and  $\lambda = 10$

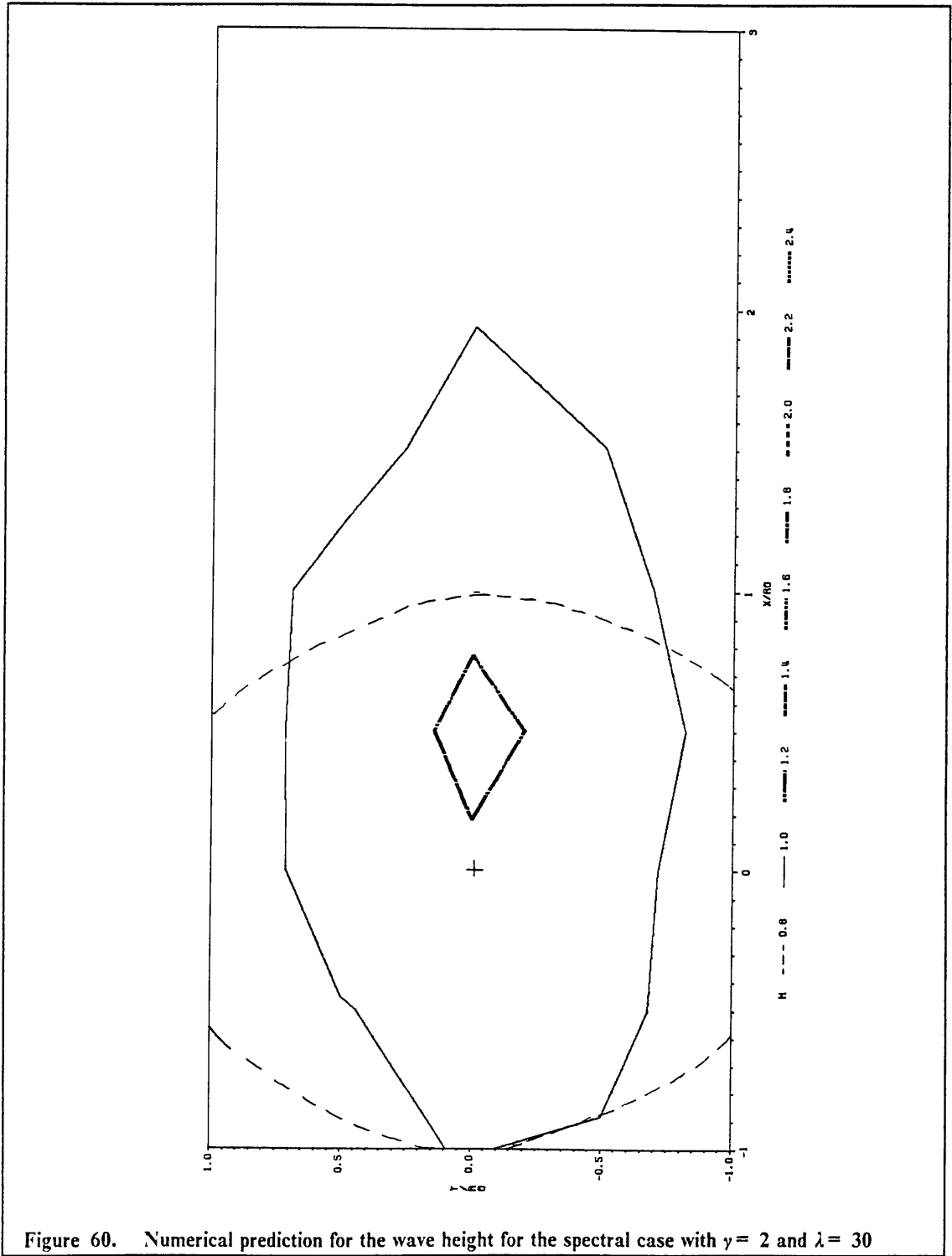


Figure 60. Numerical prediction for the wave height for the spectral case with  $\gamma = 2$  and  $\lambda = 30$

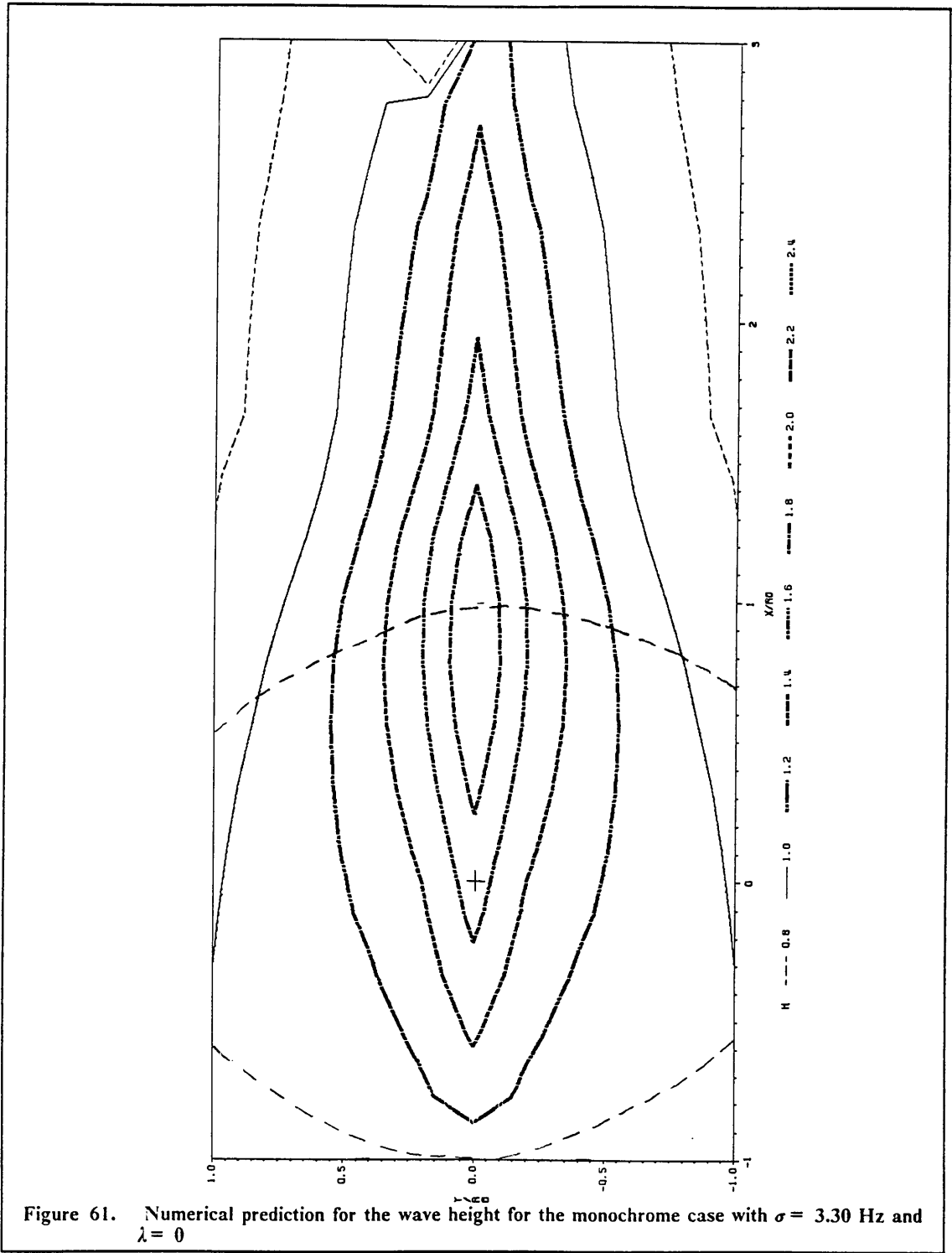
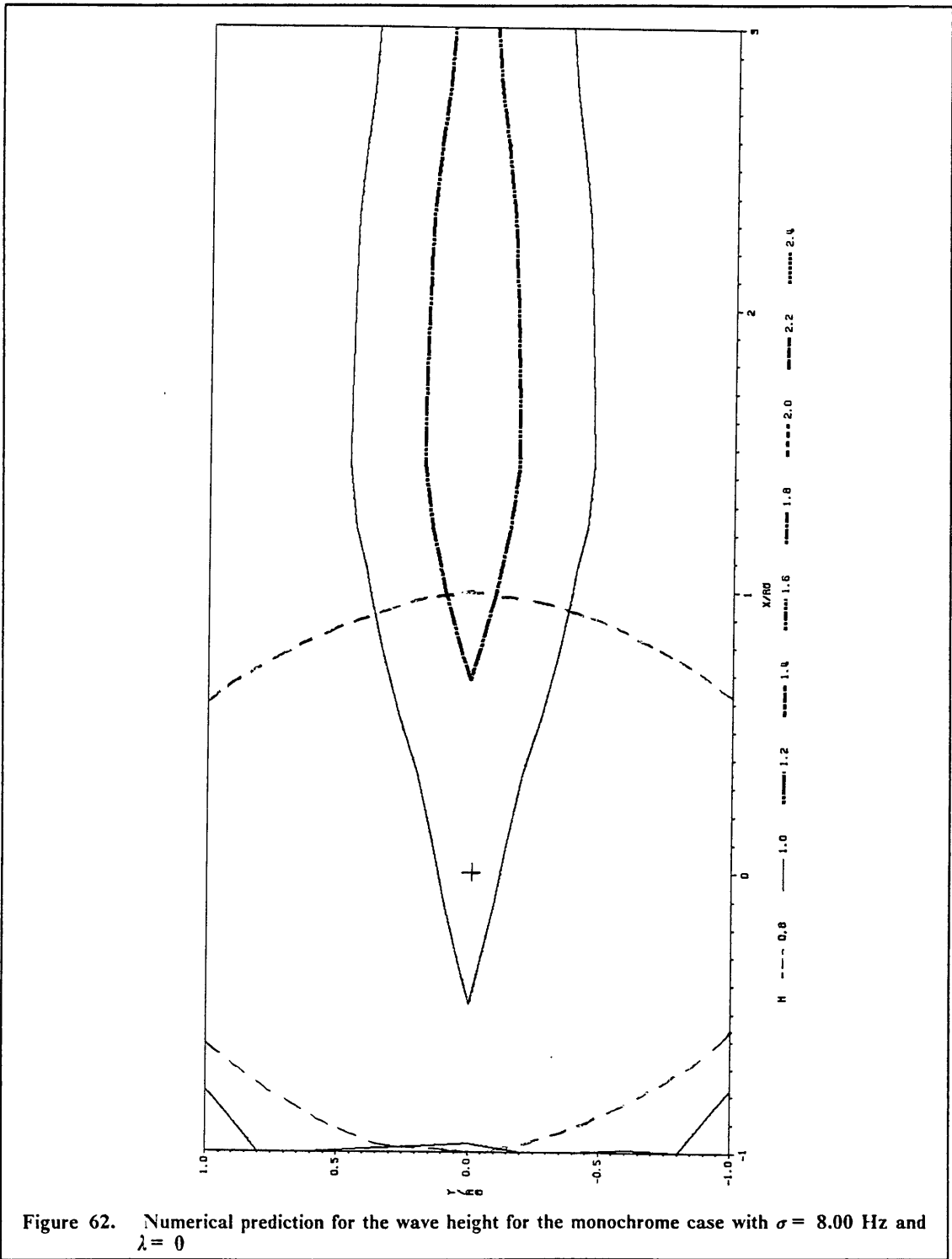


Figure 61. Numerical prediction for the wave height for the monochrome case with  $\sigma = 3.30$  Hz and  $\lambda = 0$



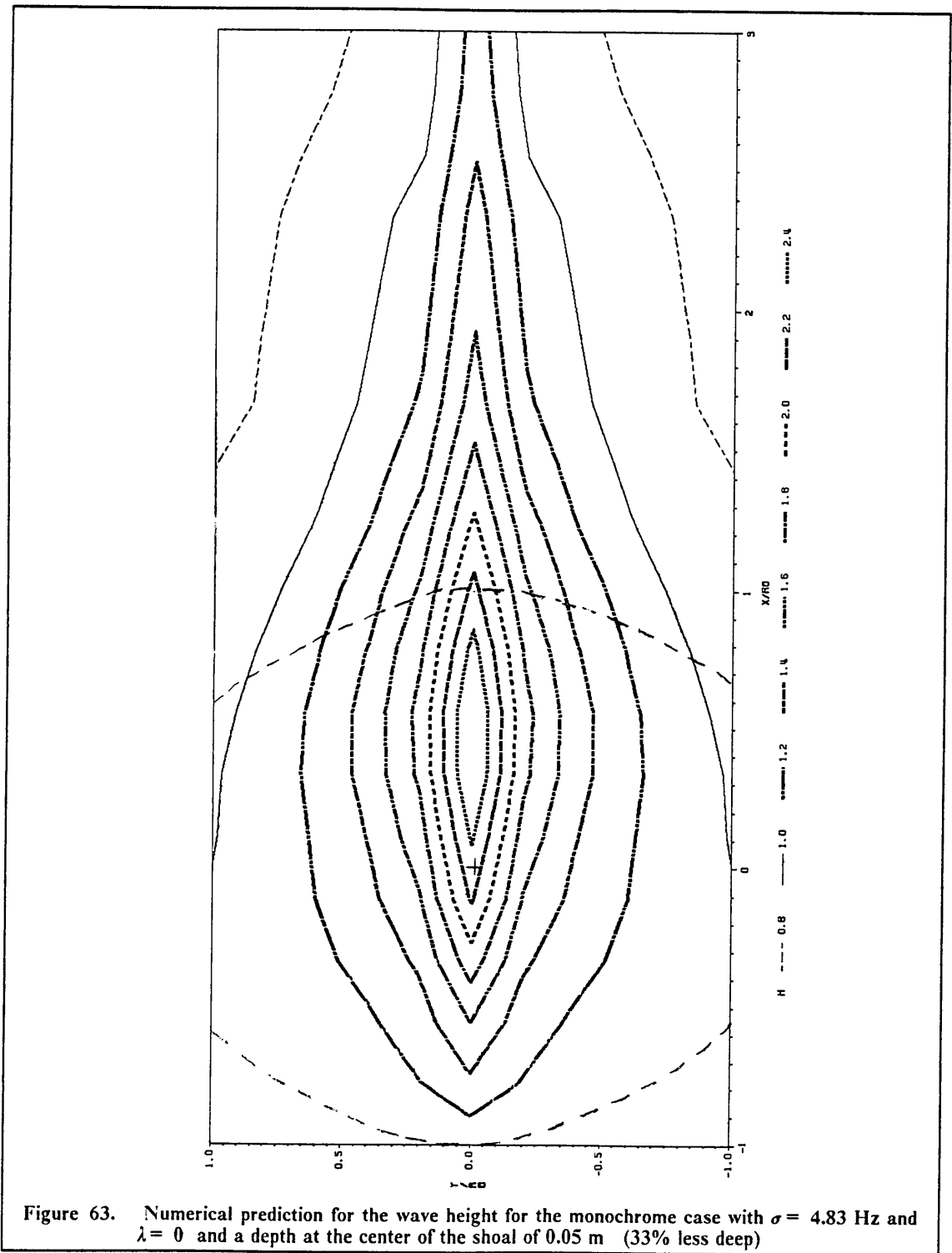


Figure 63. Numerical prediction for the wave height for the monochrome case with  $\sigma = 4.83$  Hz and  $\lambda = 0$  and a depth at the center of the shoal of 0.05 m (33% less deep)

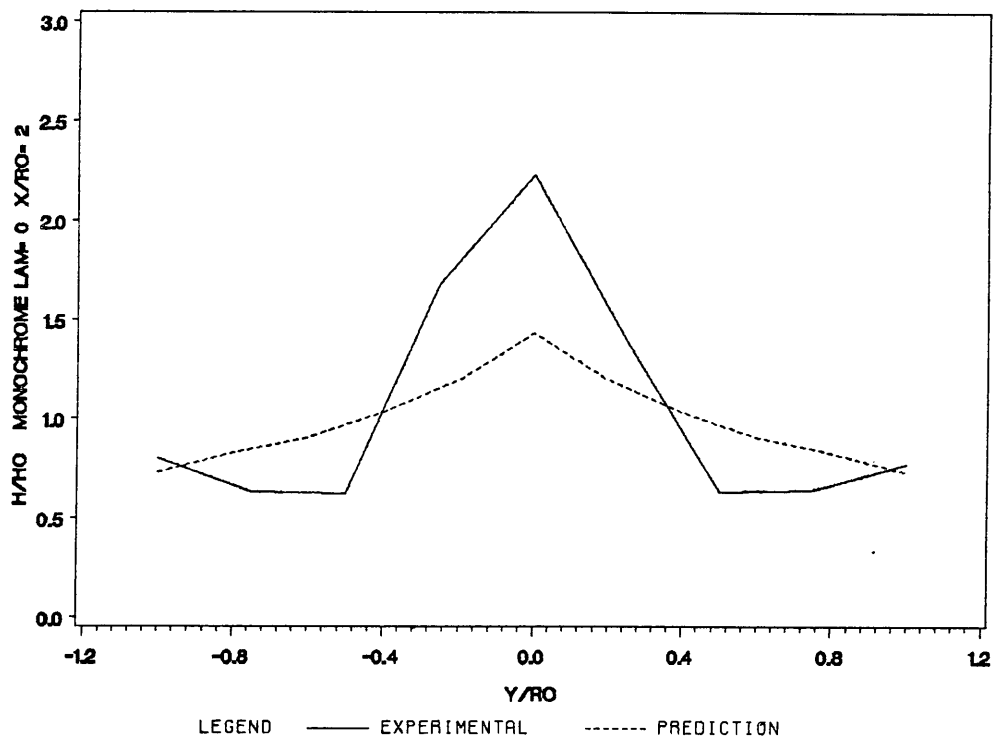
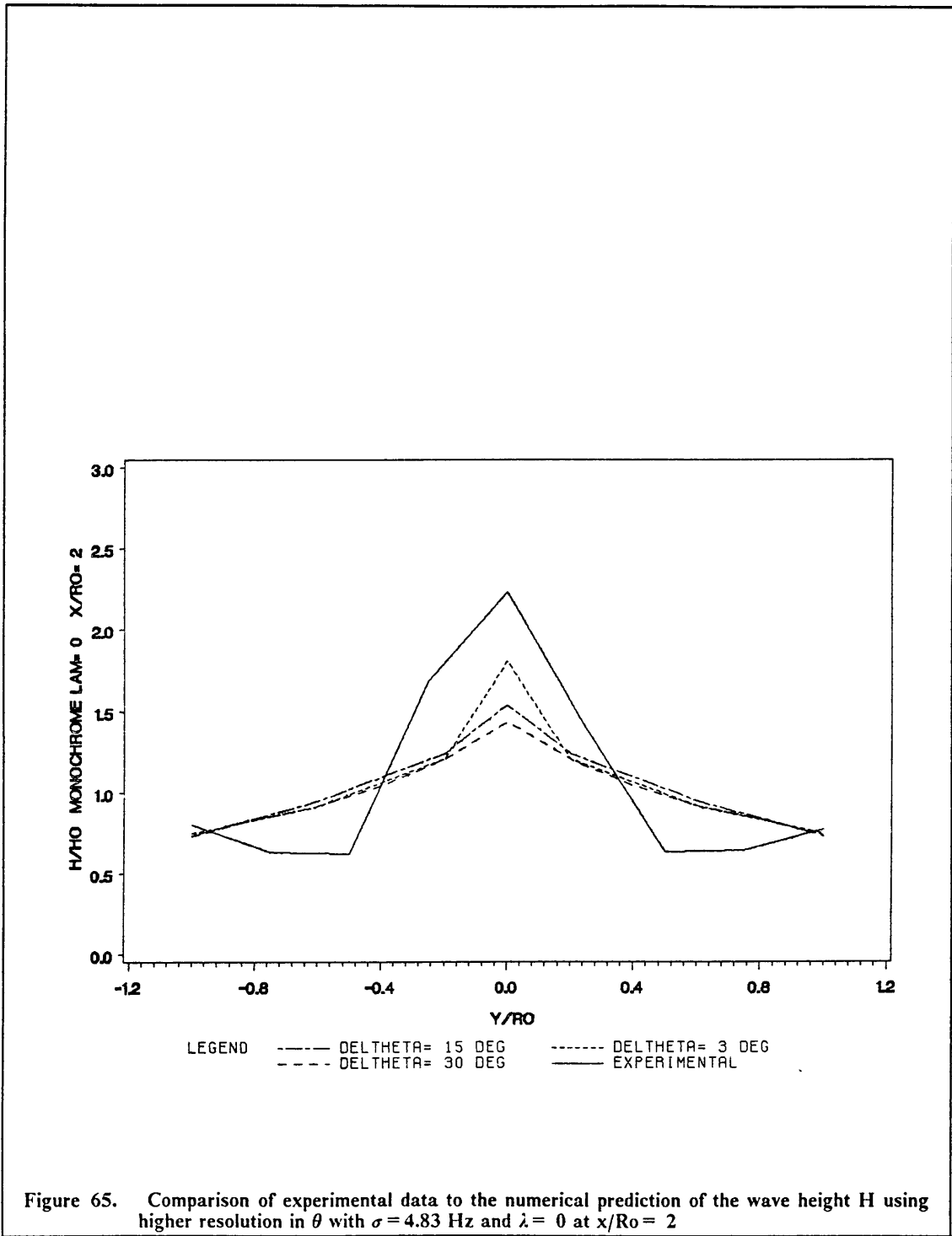
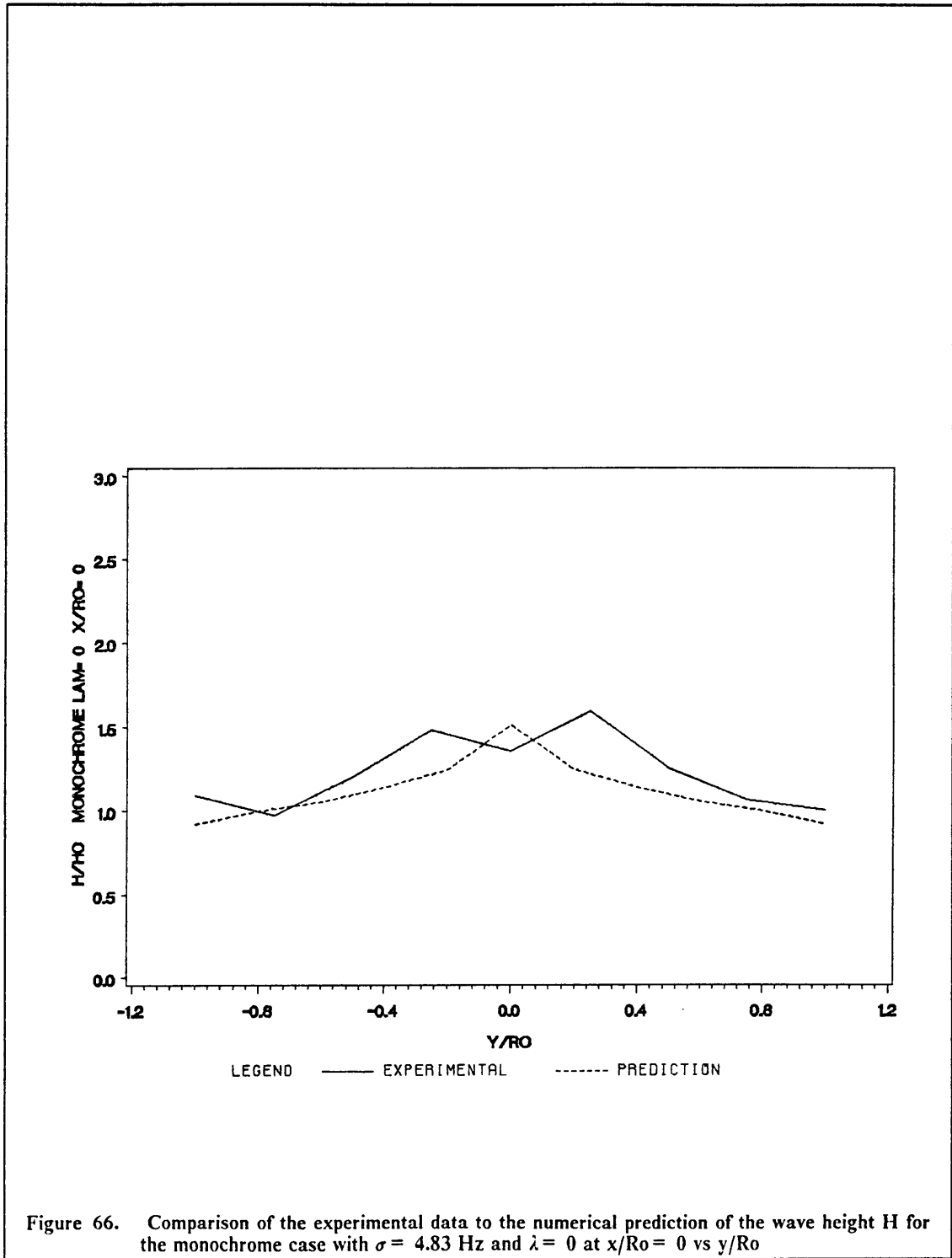


Figure 64. Comparison of the experimental data to the numerical prediction of the wave height H for the monochrome case with  $\sigma = 4.83$  Hz and  $\lambda = 0$  at  $x/R_0 = 2$  vs  $y/R_0$





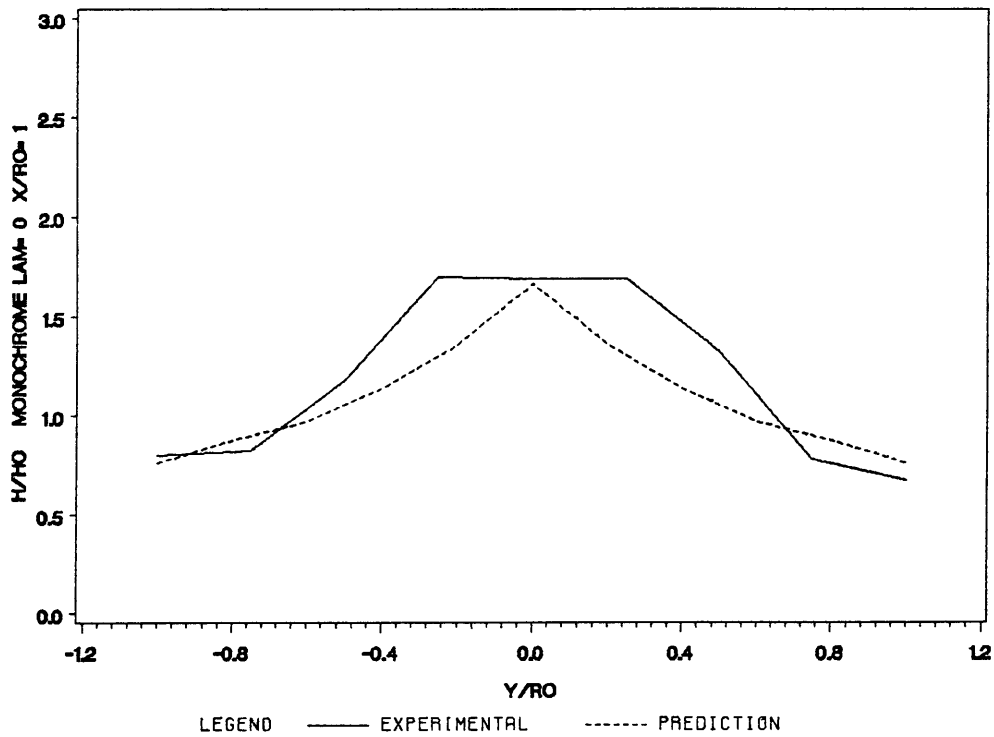
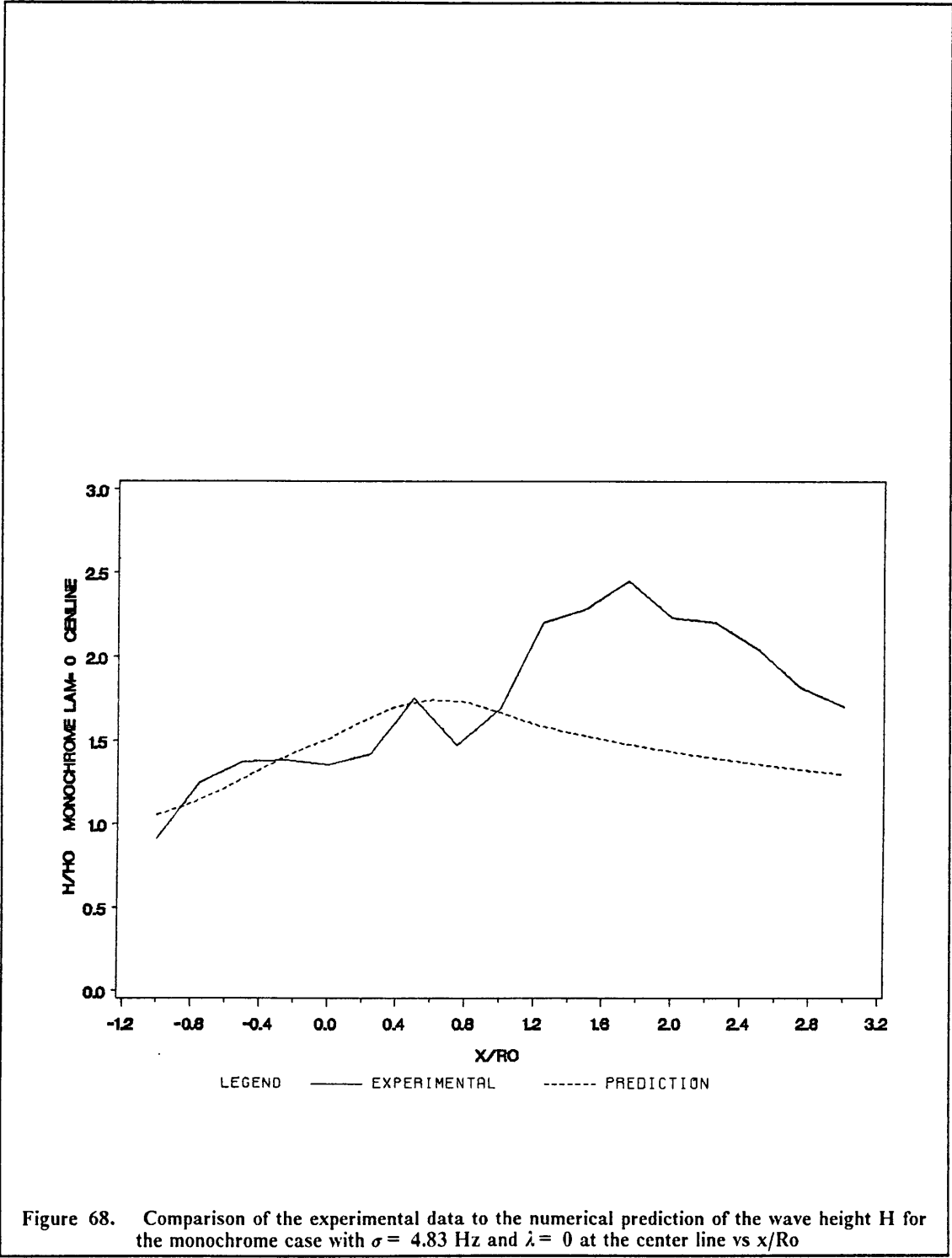


Figure 67. Comparison of the experimental data to the numerical prediction of the wave height  $H$  for the monochrome case with  $\sigma = 4.83$  Hz and  $\lambda = 0$  at  $x/R_0 = 1$  vs  $y/R_0$



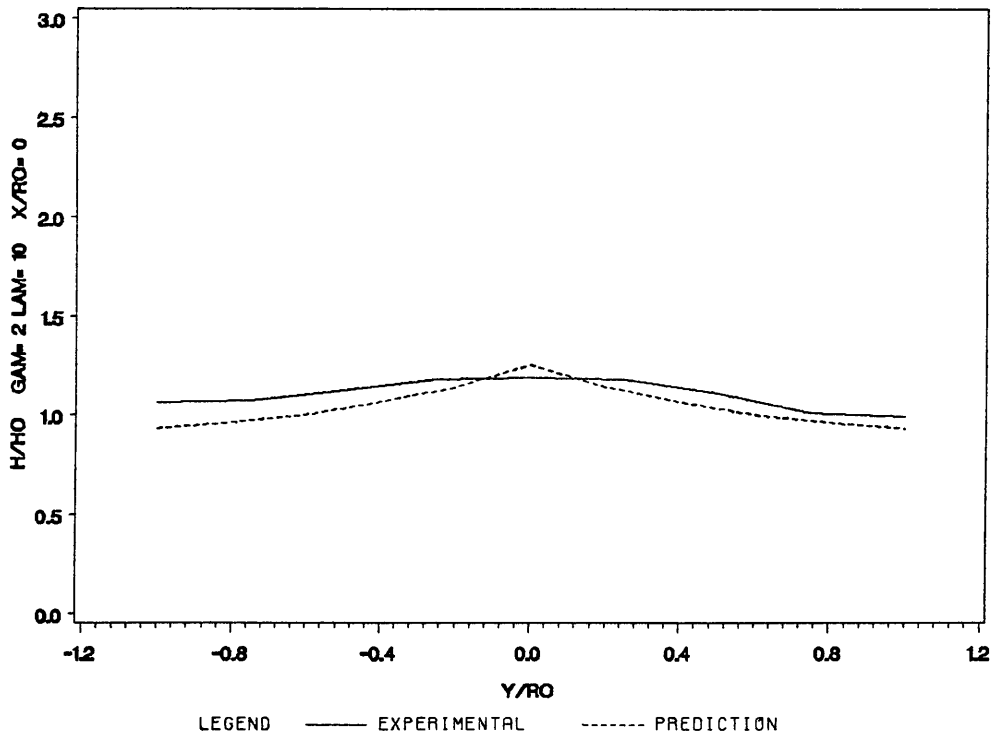


Figure 69. Comparison of the experimental data to the numerical prediction of the wave height  $H$  for the spectral case with  $\gamma = 2$  and  $\lambda = 10$  at  $x/R_0 = 0$  vs  $y/R_0$

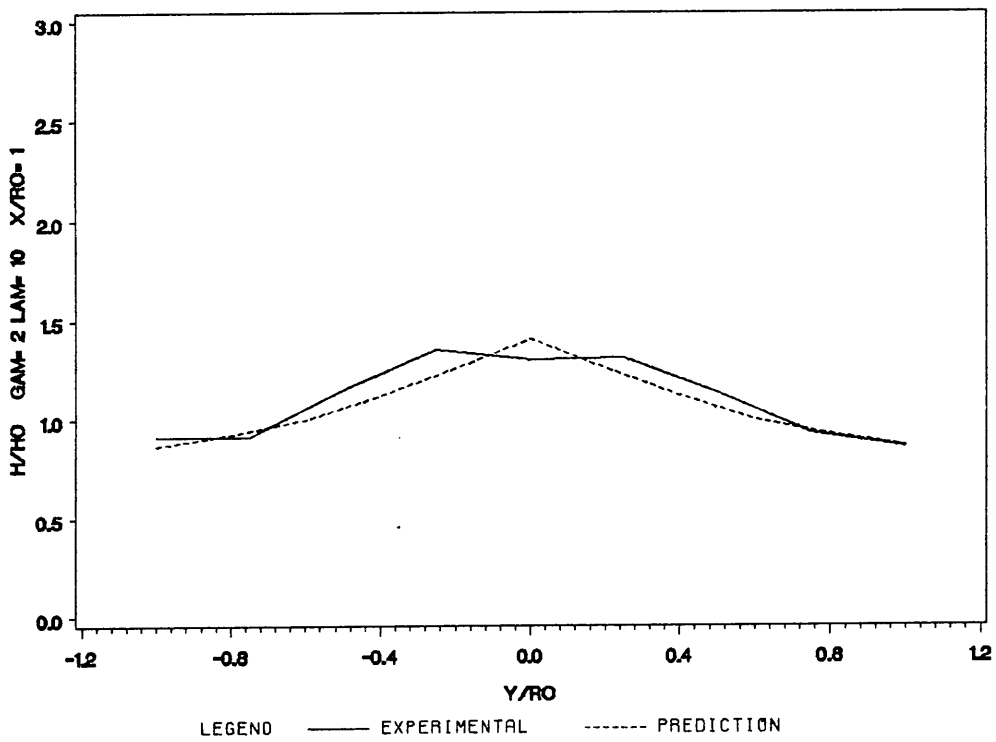


Figure 70. Comparison of the experimental data to the numerical prediction of the wave height  $H$  for the spectral case with  $\gamma = 2$  and  $\lambda = 10$  at  $x/R_0 = 1$  vs  $y/R_0$

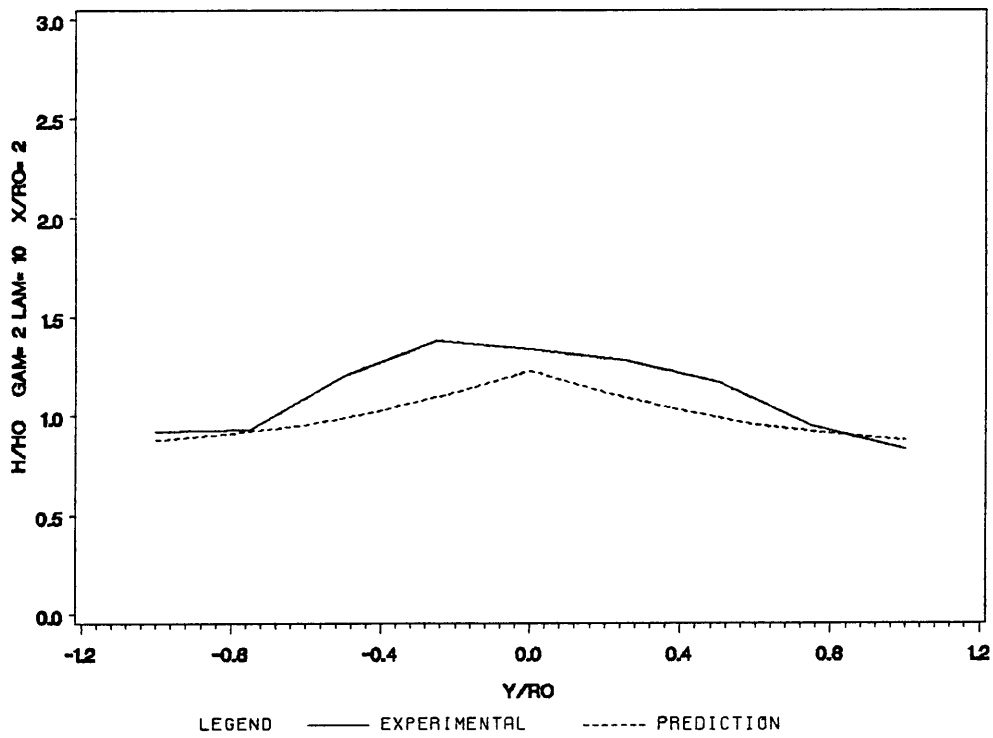


Figure 71. Comparison of the experimental data to the numerical prediction of the wave height  $H$  for the spectral case with  $\gamma = 2$  and  $\lambda = 10$  at  $x/R_0 = 2$  vs  $y/R_0$

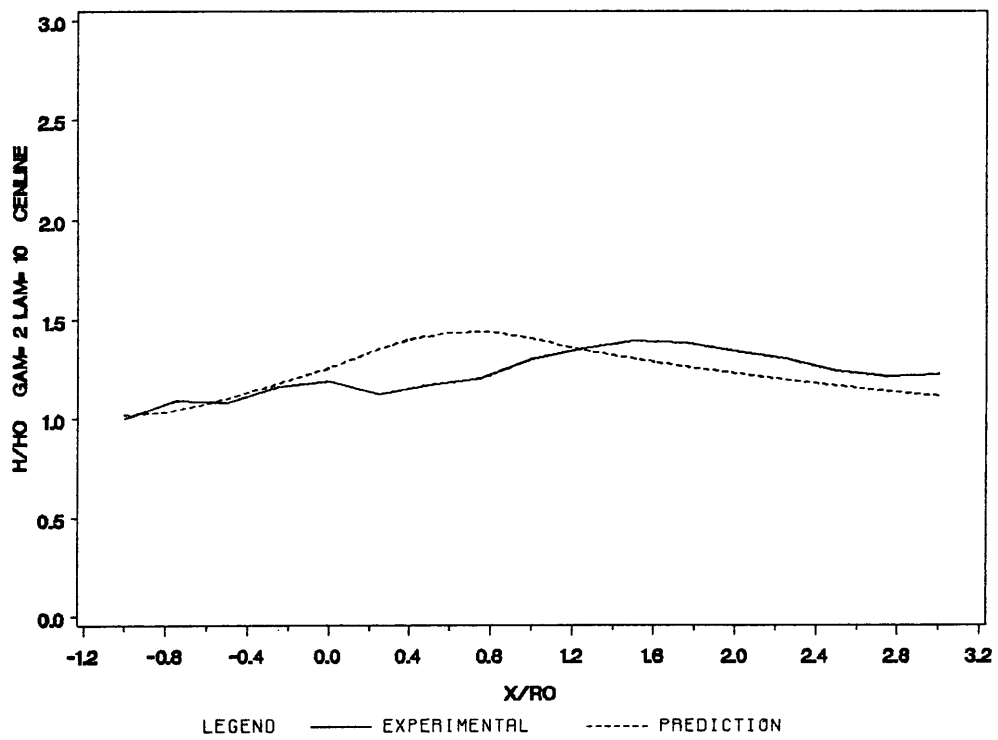


Figure 72. Comparison of the experimental data to the numerical prediction of the wave height  $H$  for the spectral case with  $\gamma = 2$  and  $\lambda = 10$  at the center line vs  $x/R_0$

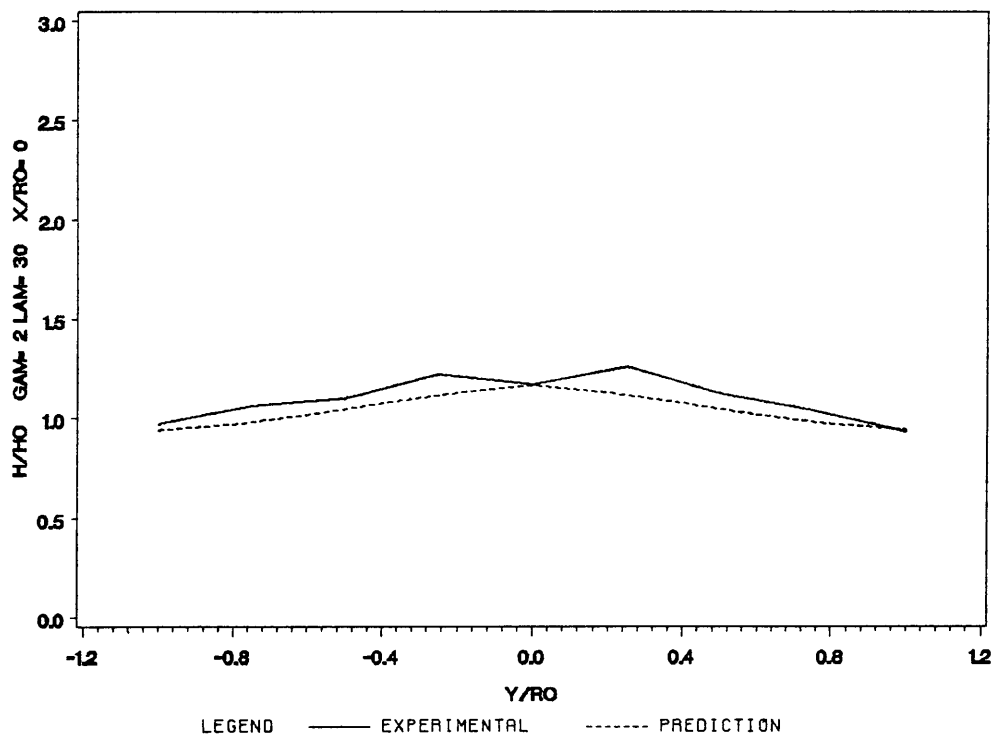


Figure 73. Comparison of the experimental data to the numerical prediction of the wave height  $H$  for the spectral case with  $\gamma = 2$  and  $\lambda = 30$  at  $x/R_0 = 0$  vs  $y/R_0$

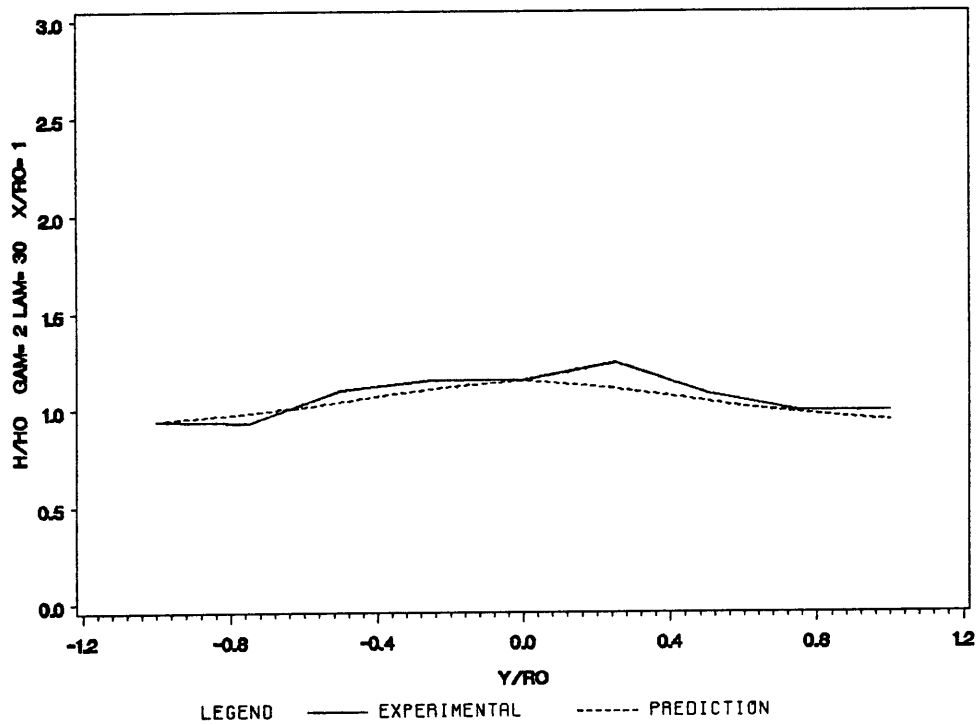


Figure 74. Comparison of the experimental data to the numerical prediction of the wave height  $H$  for the spectral case with  $\gamma = 2$  and  $\lambda = 30$  at  $x/R_0 = 1$  vs  $y/R_0$

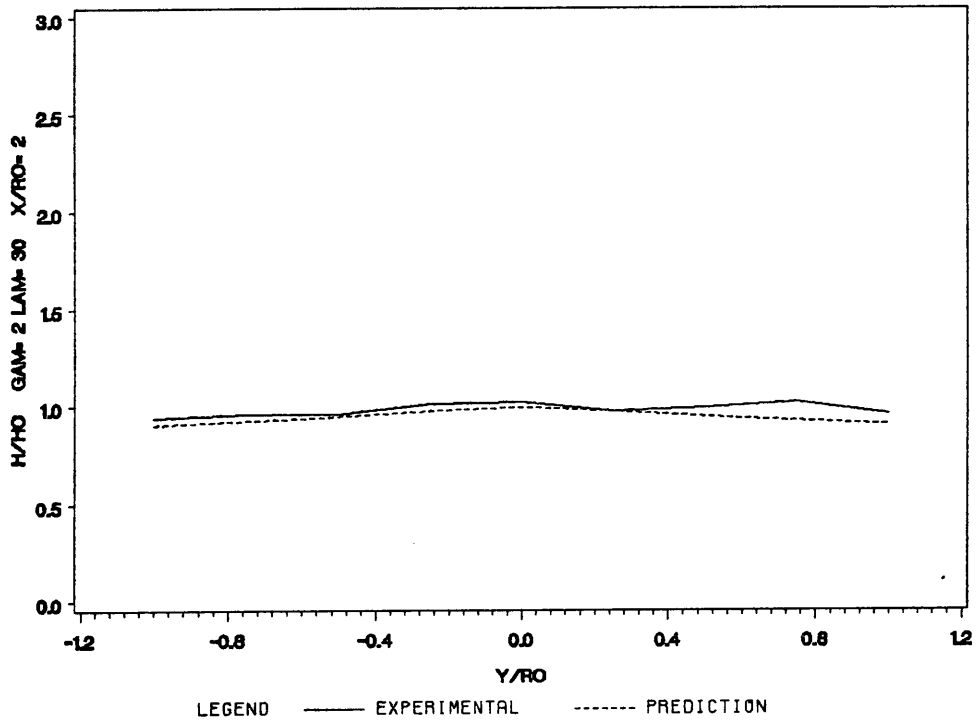


Figure 75. Comparison of the experimental data to the numerical prediction of the wave height  $H$  for the spectral case with  $\gamma = 2$  and  $\lambda = 30$  at  $x/R_0 = 2$  vs  $y/R_0$

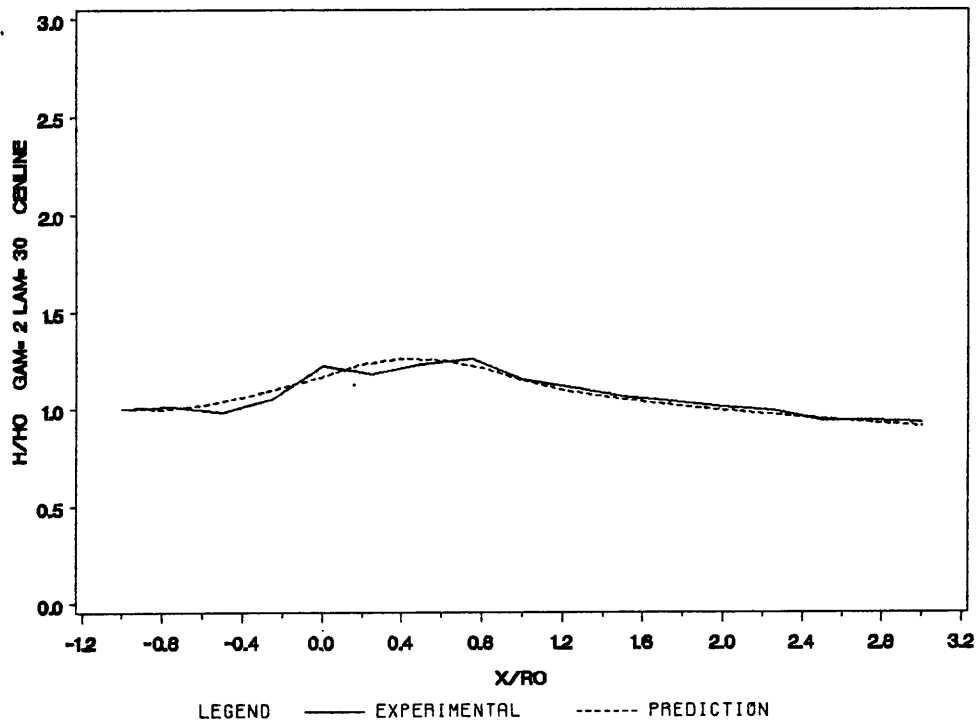


Figure 76. Comparison of the experimental data to the numerical prediction of the wave height  $H$  for the spectral case with  $\gamma = 2$  and  $\lambda = 30$  at the center line vs  $x/R_0$

**The vita has been removed from  
the scanned document**